

The Pennsylvania State University

The Graduate School

College of Engineering

**MULTI-FIELD SIMULATION OF THE SPARK PLASMA SINTERING  
PROCESS**

A Thesis in

Engineering Mechanics

by

Hui Yang

© 2010 Hui Yang

Submitted in Partial Fulfillment  
of the Requirements  
for the Degree of

Master of Science

August 2010

The thesis of Hui Yang was reviewed and approved\* by the following:

Albert E. Segall  
Professor of Department of Engineering Science and Mechanics  
Thesis Advisor

Ivica Smid  
Associate Professor of Department of Engineering Science and Mechanics

Corina Drapaca  
Assistant Professor of Department of Engineering Science and Mechanics

Judith Todd  
Professor of Department of Engineering Science and Mechanics  
P.B. Breneman Department Head  
Department of Engineering Science and Mechanics

\*Signatures are on file in the Graduate School

## ABSTRACT

Spark plasma sintering (SPS), also known as field assisted sintering, plasma activated sintering, pulsed electric current sintering, pulsed discharge pressure sintering, and/or the current activated sintering, which belongs to a class of techniques that use electric current to make sintering easier, is the most widely used electrically assisted sintering nowadays, even though the fundamental understanding of the principle mechanisms of SPS are not well established. In the present study, a finite element model capable of simulating the three-way coupling of thermal, electrical, and mechanical behavior of the SPS process, was developed using the commercially available ANSYS software for the purpose to obtain a precise insight of the cause of potential temperature and stress heterogeneities. Samples made from different materials, including alumina, ceria, copper, and tungsten with different aspect ratios were used in the simulation. Utilizing these parameters, the influences of material properties and aspect ratios on the temperature and stress distributions were then systematically investigated. In addition, an integrated experimental/numerical methodology was proposed, and the densification effect on the temperature and stress distributions was also considered by taking into account the temperature-density dependent properties of the sintering material. The model and the results provided herein are of paramount importance for understanding the phenomena in the SPS process, and can be used for the system design and process optimization that could subsequently lead to the reliable production of sintered structures with controlled and tailored properties.

## TABLE OF CONTENTS

LIST OF FIGURES .....	vi
LIST OF TABLES.....	xiv
ACKNOWLEDGEMENTS.....	xv
Chapter 1 Introduction.....	1
1.1 Motivation.....	1
1.2 Experimental and Modeling Backgrounds.....	3
1.2.1 Experimental Investigations.....	4
1.2.2 Computational Modeling.....	7
1.3 Scope of the Thesis .....	10
Chapter 2 Coupled Thermal-Electric Field Analysis.....	12
2.1 Introduction.....	12
2.2 Finite Element Modeling Details .....	12
2.2.1 Theory .....	12
2.2.2 Numerical Implementation.....	13
2.3 Results and Discussion.....	16
2.3.1 Influence of Aspect Ratios .....	18
2.3.2 Influence of Material Properties.....	28
2.4 Conclusions.....	37
Chapter 3 Coupled Thermal-Mechanical Field Analysis.....	38
3.1 Introduction.....	38
3.2 Finite Element Modeling Details .....	38
3.2.1 Theory .....	38
3.2.2 Numerical Implementation.....	39
3.3 Results and Discussion.....	40
3.4 Conclusions.....	63
Chapter 4 Densification Process Modeling.....	65
4.1 Introduction.....	65
4.2 Finite Element Modeling Details .....	65
4.2.1 Theory .....	65
4.2.2 Numerical Implementation.....	68
4.3 Results and Discussion.....	69
4.3.1 Temperature Distribution .....	69
4.3.2 Stress Distributions .....	82
4.4 Conclusions.....	100

Chapter 5 Conclusions and Future Work.....	102
5.1 Conclusions.....	102
5.2 Future Work.....	103
Bibliography .....	106
Appendix A Material Properties .....	115
Appendix B ANSYS Input Files.....	121

## LIST OF FIGURES

Figure 1-1. Schematic of the spark plasma sintering (SPS) apparatus. ....	2
Figure 2-1. Schematic of the SPS apparatus showing dimensions (in millimeter) and coordinate system with origin at the middle of the sample. ....	16
Figure 2-2. Temperature evolution at the center points of the samples with the same aspect ratios: (a) Ratio 0.5, (b) Ratio 1.0, and (c) Ratio 1.5. ....	17
Figure 2-3. Steady-state contour plots of the temperature distribution in the punch/sample/die area of alumina samples with different aspect ratios: 0.5 (left), 1.0 (middle), and 1.5 (right). ....	20
Figure 2-4. Steady-state contour plots of the temperature distribution in the punch/sample/die area of ceria samples with different aspect ratios: 0.5 (left), 1.0 (middle), and 1.5 (right). ....	20
Figure 2-5. Steady-state contour plots of the temperature distribution in the punch/sample/die area of copper samples with different aspect ratios: 0.5 (left), 1.0 (middle), and 1.5 (right). ....	21
Figure 2-6. Steady-state contour plots of the temperature distribution in the punch/sample/die area of tungsten samples with different aspect ratios: 0.5 (left), 1.0 (middle), and 1.5 (right). ....	21
Figure 2-7. Comparison of the steady-state radial temperature profiles in the middle cross-section of the sample and the die for: (a) Alumina, (b) Ceria, (c) Copper, and (d) Tungsten. ....	22
Figure 2-8. Comparison of the steady-state vertical temperature profiles along the axis of symmetry in the punch/sample/die assembly for: (a) Alumina, (b) Ceria, (c) Copper, and (d) Tungsten. ....	23
Figure 2-9. Steady-state contour plots of the temperature distribution in the region of alumina samples with different aspect ratios: 0.5 (left), 1.0 (middle), and 1.5 (right). ....	24
Figure 2-10. Steady-state contour plots of the temperature distribution in the region of ceria samples with different aspect ratios: 0.5 (left), 1.0 (middle), and 1.5 (right). ....	24
Figure 2-11. Steady-state contour plots of the temperature distribution in the region of copper samples with different aspect ratios: 0.5 (left), 1.0 (middle), and 1.5 (right). ....	25
Figure 2-12. Steady-state contour plots of the temperature distribution in the region of tungsten samples with different aspect ratios: 0.5 (left), 1.0 (middle), and 1.5 (right). ....	25

Figure 2-13. Comparison of the steady-state radial temperature profiles in the middle cross-section of the sample for: (a) Alumina, (b) Ceria, (c) Copper, and (d) Tungsten.....	26
Figure 2-14. Comparison of the steady-state vertical temperature profiles along the axis of symmetry in the sample for: (a) Alumina, (b) Ceria, (c) Copper, and (d) Tungsten. ...	27
Figure 2-15. Comparison of the steady-state radial temperature profiles in the middle cross-section of the sample and the die with the same sample aspect ratios: (a) Ratio 0.5, (b) Ratio 1.0, and (c) Ratio 1.5.....	29
Figure 2-16. Comparison of the steady-state vertical temperature profiles along the axis of symmetry in the punch/sample/die assembly with the same sample aspect ratios: (a) Ratio 0.5, (b) Ratio 1.0, and (c) Ratio 1.5.....	30
Figure 2-17. Comparison of the steady-state temperature distributions in the samples with the same aspect ratio of 0.5 for: (a) Alumina, (b) Ceria, (c) Copper, and (d) Tungsten.....	32
Figure 2-18. Comparison of the steady-state temperature distributions in the samples with the same aspect ratio of 1.0 for: (a) Alumina, (b) Ceria, (c) Copper, and (d) Tungsten.....	33
Figure 2-19. Comparison of the steady-state temperature distributions in the samples with the same aspect ratio of 1.5 for: (a) Alumina, (b) Ceria, (c) Copper, and (d) Tungsten.....	34
Figure 2-20. Comparison of the steady-state radial temperature profiles in the middle cross-section of the sample with the same aspect ratios: (a) Ratio 0.5, (b) Ratio 1.0, and (c) Ratio 1.5.....	35
Figure 2-21. Comparison of the steady-state vertical temperature profiles along the axis of symmetry in the sample with the same aspect ratios: (a) Ratio 0.5, (b) Ratio 1.0, and (c) Ratio 1.5.....	36
Figure 3-1. Contour plots of the radial stress distribution in the punch/sample/die area of alumina samples with different aspect ratios: 0.5 (left), 1.0 (middle), and 1.5 (right).....	44
Figure 3-2. Contour plots of the radial stress distribution in the punch/sample/die area of ceria samples with different aspect ratios: 0.5 (left), 1.0 (middle), and 1.5 (right).....	44
Figure 3-3. Contour plots of the radial stress distribution in the punch/sample/die area of copper samples with different aspect ratios: 0.5 (left), 1.0 (middle), and 1.5 (right).....	45
Figure 3-4. Contour plots of the radial stress distribution in the punch/sample/die area of tungsten samples with different aspect ratios: 0.5 (left), 1.0 (middle), and 1.5 (right)....	45
Figure 3-5. Contour plots of the hoop stress distribution in the punch/sample/die area of alumina samples with different aspect ratios: 0.5 (left), 1.0 (middle), and 1.5 (right).....	46

Figure 3-6. Contour plots of the hoop stress distribution in the punch/sample/die area of ceria samples with different aspect ratios: 0.5 (left), 1.0 (middle), and 1.5 (right).....	46
Figure 3-7. Contour plots of the hoop stress distribution in the punch/sample/die area of copper samples with different aspect ratios: 0.5 (left), 1.0 (middle), and 1.5 (right).....	47
Figure 3-8. Contour plots of the hoop stress distribution in the punch/sample/die area of tungsten samples with different aspect ratios: 0.5 (left), 1.0 (middle), and 1.5 (right)....	47
Figure 3-9. Contour plots of the axial stress distribution in the punch/sample/die area of alumina samples with different aspect ratios: 0.5 (left), 1.0 (middle), and 1.5 (right)....	48
Figure 3-10. Contour plots of the axial stress distribution in the punch/sample/die area of ceria samples with different aspect ratios: 0.5 (left), 1.0 (middle), and 1.5 (right).....	48
Figure 3-11. Contour plots of the axial stress distribution in the punch/sample/die area of copper samples with different aspect ratios: 0.5 (left), 1.0 (middle), and 1.5 (right).....	49
Figure 3-12. Contour plots of the axial stress distribution in the punch/sample/die area of tungsten samples with different aspect ratios: 0.5 (left), 1.0 (middle), and 1.5 (right)....	49
Figure 3-13. Contour plots of the radial stress distribution in the region of alumina samples with different aspect ratios: 0.5 (left), 1.0 (middle), and 1.5 (right). .....	50
Figure 3-14. Contour plots of the radial stress distribution in the region of ceria samples with different aspect ratios: 0.5 (left), 1.0 (middle), and 1.5 (right). .....	50
Figure 3-15. Contour plots of the radial stress distribution in the region of copper samples with different aspect ratios: 0.5 (left), 1.0 (middle), and 1.5 (right). .....	51
Figure 3-16. Contour plots of the radial stress distribution in the region of tungsten samples with different aspect ratios: 0.5 (left), 1.0 (middle), and 1.5 (right). .....	51
Figure 3-17. Contour plots of the hoop stress distribution in the region of alumina samples with different aspect ratios: 0.5 (left), 1.0 (middle), and 1.5 (right). .....	52
Figure 3-18. Contour plots of the hoop stress distribution in the region of ceria samples with different aspect ratios: 0.5 (left), 1.0 (middle), and 1.5 (right). .....	52
Figure 3-19. Contour plots of the hoop stress distribution in the region of copper samples with different aspect ratios: 0.5 (left), 1.0 (middle), and 1.5 (right). .....	53
Figure 3-20. Contour plots of the hoop stress distribution in the region of tungsten samples with different aspect ratios: 0.5 (left), 1.0 (middle), and 1.5 (right). .....	53
Figure 3-21. Contour plots of the axial stress distribution in the region of alumina samples with different aspect ratios: 0.5 (left), 1.0 (middle), and 1.5 (right). .....	54
Figure 3-22. Contour plots of the axial stress distribution in the region of ceria samples with different aspect ratios: 0.5 (left), 1.0 (middle), and 1.5 (right). .....	54

Figure 3-23. Contour plots of the axial stress distribution in the region of copper samples with different aspect ratios: 0.5 (left), 1.0 (middle), and 1.5 (right). .....	55
Figure 3-24. Contour plots of the axial stress distribution in the region of tungsten samples with different aspect ratios: 0.5 (left), 1.0 (middle), and 1.5 (right). .....	55
Figure 3-25. Comparison of the stress profiles in the middle cross-section of the sample and the die with the same sample aspect ratio of 0.5 for: (a) Alumina, (b) Ceria, (c) Copper, and (d) Tungsten.....	56
Figure 3-26. Comparison of the stress profiles in the middle cross-section of the sample and the die with the same sample aspect ratio of 1.0 for: (a) Alumina, (b) Ceria, (c) Copper, and (d) Tungsten.....	57
Figure 3-27. Comparison of the stress profiles in the middle cross-section of the sample and the die with the same sample aspect ratio of 1.5 for: (a) Alumina, (b) Ceria, (c) Copper, and (d) Tungsten.....	58
Figure 3-28. Comparison of the stress profiles along the axis of symmetry in the punch/sample/die assembly with the same sample aspect ratio of 0.5 for: (a) Alumina, (b) Ceria, (c) Copper, and (d) Tungsten.....	59
Figure 3-29. Comparison of the stress profiles along the axis of symmetry in the punch/sample/die assembly with the same sample aspect ratio of 1.0 for: (a) Alumina, (b) Ceria, (c) Copper, and (d) Tungsten.....	60
Figure 3-30. Comparison of the stress profiles along the axis of symmetry in the punch/sample/die assembly with the same sample aspect ratio of 1.5 for: (a) Alumina, (b) Ceria, (c) Copper, and (d) Tungsten.....	61
Figure 4-1. Assumed experimental curve (red) for the relative density of the powder compact; Step-wise relative density curve (blue) used in the simulation. ....	69
Figure 4-2. Temperature evolution at the center points of the alumina samples with constant and evolving densities.....	70
Figure 4-3. Comparison of the radial temperature profiles in the middle cross-section of the sample and the die at different time steps: (a) $t=50$ s, (b) $t=100$ s, (c) $t=200$ s, and (d) $t=300$ s. ....	71
Figure 4-4. Comparison of the radial temperature profiles in the middle cross-section of the sample and the die at different time steps: (e) $t=400$ s, (f) $t=500$ s, (g) $t=600$ s, and (h) $t=1000$ s. ....	72
Figure 4-5. Comparison of the vertical temperature profiles along the axis of symmetry in the punch/sample/die assembly at different time steps: (a) $t=50$ s, (b) $t=100$ s, (c) $t=200$ s, and (d) $t=300$ s. ....	73

Figure 4-6. Comparison of the vertical temperature profiles along the axis of symmetry in the punch/sample/die assembly at different time steps: (e) $t=400$ s, (f) $t=500$ s, (g) $t=600$ s, and (h) $t=1000$ s. ....	74
Figure 4-7. Contour plots of the temperature distribution in the region of samples with constant density (left) and evolving density (right) at $t=50$ s.....	75
Figure 4-8. Contour plots of the temperature distribution in the region of samples with constant density (left) and evolving density (right) at $t=100$ s.....	75
Figure 4-9. Contour plots of the temperature distribution in the region of samples with constant density (left) and evolving density (right) at $t=200$ s.....	76
Figure 4-10. Contour plots of the temperature distribution in the region of samples with constant density (left) and evolving density (right) at $t=300$ s.....	76
Figure 4-11. Contour plots of the temperature distribution in the region of samples with constant density (left) and evolving density (right) at $t=400$ s.....	76
Figure 4-12. Contour plots of the temperature distribution in the region of samples with constant density (left) and evolving density (right) at $t=500$ s.....	77
Figure 4-13. Contour plots of the temperature distribution in the region of samples with constant density (left) and evolving density (right) at $t=600$ s.....	77
Figure 4-14. Contour plots of the temperature distribution in the region of samples with constant density (left) and evolving density (right) at $t=1000$ s.....	77
Figure 4-15. Comparison of the radial temperature profiles in the middle cross-section of the sample at different time steps: (a) $t=50$ s, (b) $t=100$ s, (c) $t=200$ s, and (d) $t=300$ s. ....	78
Figure 4-16. Comparison of the radial temperature profiles in the middle cross-section of the sample at different time steps: (e) $t=400$ s, (f) $t=500$ s, (g) $t=600$ s, and (h) $t=1000$ s.....	79
Figure 4-17. Comparison of the vertical temperature profiles along the axis of symmetry in the sample at different time steps: (a) $t=50$ s, (b) $t=100$ s, (c) $t=200$ s, and (d) $t=300$ s.....	80
Figure 4-18. Comparison of the vertical temperature profiles along the axis of symmetry in the sample at different time steps: (e) $t=400$ s, (f) $t=500$ s, (g) $t=600$ s, and (h) $t=1000$ s.....	81
Figure 4-19. Contour plots of the radial stress distribution in the region of samples with constant density (left) and evolving density (right) at $t=50$ s.....	84
Figure 4-20. Contour plots of the radial stress distribution in the region of samples with constant density (left) and evolving density (right) at $t=100$ s.....	84

Figure 4-21. Contour plots of the radial stress distribution in the region of samples with constant density (left) and evolving density (right) at $t=200$ s.....	84
Figure 4-22. Contour plots of the radial stress distribution in the region of samples with constant density (left) and evolving density (right) at $t=300$ s.....	85
Figure 4-23. Contour plots of the radial stress distribution in the region of samples with constant density (left) and evolving density (right) at $t=400$ s.....	85
Figure 4-24. Contour plots of the radial stress distribution in the region of samples with constant density (left) and evolving density (right) at $t=500$ s.....	85
Figure 4-25. Contour plots of the radial stress distribution in the region of samples with constant density (left) and evolving density (right) at $t=600$ s.....	86
Figure 4-26. Contour plots of the radial stress distribution in the region of samples with constant density (left) and evolving density (right) at $t=1000$ s.....	86
Figure 4-27. Contour plots of the hoop stress distribution in the region of samples with constant density (left) and evolving density (right) at $t=50$ s.....	86
Figure 4-28. Contour plots of the hoop stress distribution in the region of samples with constant density (left) and evolving density (right) at $t=100$ s.....	87
Figure 4-29. Contour plots of the hoop stress distribution in the region of samples with constant density (left) and evolving density (right) at $t=200$ s.....	87
Figure 4-30. Contour plots of the hoop stress distribution in the region of samples with constant density (left) and evolving density (right) at $t=300$ s.....	87
Figure 4-31. Contour plots of the hoop stress distribution in the region of samples with constant density (left) and evolving density (right) at $t=400$ s.....	88
Figure 4-32. Contour plots of the hoop stress distribution in the region of samples with constant density (left) and evolving density (right) at $t=500$ s.....	88
Figure 4-33. Contour plots of the hoop stress distribution in the region of samples with constant density (left) and evolving density (right) at $t=600$ s.....	88
Figure 4-34. Contour plots of the hoop stress distribution in the region of samples with constant density (left) and evolving density (right) at $t=1000$ s.....	89
Figure 4-35. Contour plots of the axial stress distribution in the region of samples with constant density (left) and evolving density (right) at $t=50$ s.....	89
Figure 4-36. Contour plots of the axial stress distribution in the region of samples with constant density (left) and evolving density (right) at $t=100$ s.....	89
Figure 4-37. Contour plots of the axial stress distribution in the region of samples with constant density (left) and evolving density (right) at $t=200$ s.....	90

Figure 4-38. Contour plots of the axial stress distribution in the region of samples with constant density (left) and evolving density (right) at $t=300$ s.....	90
Figure 4-39. Contour plots of the axial stress distribution in the region of samples with constant density (left) and evolving density (right) at $t=400$ s.....	90
Figure 4-40. Contour plots of the axial stress distribution in the region of samples with constant density (left) and evolving density (right) at $t=500$ s.....	91
Figure 4-41. Contour plots of the axial stress distribution in the region of samples with constant density (left) and evolving density (right) at $t=600$ s.....	91
Figure 4-42. Contour plots of the axial stress distribution in the region of samples with constant density (left) and evolving density (right) at $t=1000$ s.....	91
Figure 4-43. Comparison of the stress profiles in the middle cross-section of the samples with constant density (left) and evolving density (right) at $t=50$ s.....	92
Figure 4-44. Comparison of the stress profiles in the middle cross-section of the samples with constant density (left) and evolving density (right) at $t=100$ s.....	92
Figure 4-45. Comparison of the stress profiles in the middle cross-section of the samples with constant density (left) and evolving density (right) at $t=200$ s.....	93
Figure 4-46. Comparison of the stress profiles in the middle cross-section of the samples with constant density (left) and evolving density (right) at $t=300$ s.....	93
Figure 4-47. Comparison of the stress profiles in the middle cross-section of the samples with constant density (left) and evolving density (right) at $t=400$ s.....	94
Figure 4-48. Comparison of the stress profiles in the middle cross-section of the samples with constant density (left) and evolving density (right) at $t=500$ s.....	94
Figure 4-49. Comparison of the stress profiles in the middle cross-section of the samples with constant density (left) and evolving density (right) at $t=600$ s.....	95
Figure 4-50. Comparison of the stress profiles in the middle cross-section of the samples with constant density (left) and evolving density (right) at $t=1000$ s.....	95
Figure 4-51. Comparison of the stress profiles along the axis of symmetry in the samples with constant density (left) and evolving density (right) at $t=50$ s.....	96
Figure 4-52. Comparison of the stress profiles along the axis of symmetry in the samples with constant density (left) and evolving density (right) at $t=100$ s.....	96
Figure 4-53. Comparison of the stress profiles along the axis of symmetry in the samples with constant density (left) and evolving density (right) at $t=200$ s.....	97
Figure 4-54. Comparison of the stress profiles along the axis of symmetry in the samples with constant density (left) and evolving density (right) at $t=300$ s.....	97

- Figure 4-55. Comparison of the stress profiles along the axis of symmetry in the samples with constant density (left) and evolving density (right) at  $t=400$  s.....98
- Figure 4-56. Comparison of the stress profiles along the axis of symmetry in the samples with constant density (left) and evolving density (right) at  $t=500$  s.....98
- Figure 4-57. Comparison of the stress profiles along the axis of symmetry in the samples with constant density (left) and evolving density (right) at  $t=600$  s.....99
- Figure 4-58. Comparison of the stress profiles along the axis of symmetry in the samples with constant density (left) and evolving density (right) at  $t=1000$  s.....99

**LIST OF TABLES**

Table 2-1. Minimum and maximum temperature in the sample region ( $^{\circ}\text{C}$ ). .....	28
Table 3-1. Minimum and maximum radial stress in the sample region (MPa).....	62
Table 3-2. Minimum and maximum hoop stress in the sample region (MPa).....	62
Table 3-3. Minimum and maximum axial stress in the sample region (MPa).....	63
Table A-1. Temperature dependent material properties of fully dense alumina.....	116
Table A-2. Temperature dependent material properties of fully dense ceria.....	117
Table A-3. Temperature dependent material properties of fully dense copper.....	118
Table A-4. Temperature dependent material properties of fully dense tungsten. ....	119
Table A-5. Temperature dependent material properties of fully dense graphite. ....	120

## ACKNOWLEDGEMENTS

I would like to express my sincere gratitude to my advisor, Professor Albert E. Segall, for providing me with the opportunity to study under his direction, and the support and encouragement he gave to me throughout my study at The Pennsylvania State University. In addition to my advisor, I also would like to thank my committee members, Professors Ivica Smid and Corina Drapaca for patiently reading my thesis and for their insightful comments and advices.

I would also like to acknowledge the Idaho National Laboratory for the financial support during the course of this work. The help that came from other collaborative groups of this project is also highly appreciated. Special thanks should go to Mr. Jeffrey Perkins from the Department of Materials Science and Engineering at Boise State University for providing me with all the experimental data.

I also want to take this opportunity to thank my colleagues in the Department of Engineering Science and Mechanics at The Pennsylvania State University. Without their help, it would have been impossible for me to finish my M.S. study. Particular thanks to Mr. Jason Harris, one of the members in our research group, for all the help he provided to me.

Last, but not least, I would like to thank my family and friends for their love and supports. This work is dedicated to my great parents.

## **Chapter 1**

### **Introduction**

#### **1.1 Motivation**

Spark plasma sintering (SPS), also known as field assisted sintering, plasma activated sintering, pulsed electric current sintering, pulsed discharge pressure sintering, and/or the current activated sintering[1-3], which belongs to a class of techniques that use electric current to make sintering easier, has emerged as one of the most significant and effective sintering techniques. As an important tool for consolidation of powders, the SPS process is different from the conventional hot pressing and hot isostatic pressing processes which involve an external heating scheme. Instead, the SPS process simultaneously combines the application of electric current and pressure directly on the powders. According to the description of the SPS process, powders are placed in an electrically conducting die (typically graphite), as shown in Figure 1-1, and high-density electric currents (usually pulsed DC) are allowed to pass the die and in applicable cases, through the powders, to produce high heating rates by Joule heating and potentially enhance the diffusion and/or reaction processes significantly while uniaxial external pressures are also applied. The stresses generated by external pressures play a significant role in the densification process of the powders. Based on these factors, the defining characteristics of the SPS process include relatively high heating rates, moderate to high

pressures, as well as any potential symbiotic reactions within the materials caused by the current interacting with the grain boundaries and internal structures [3].

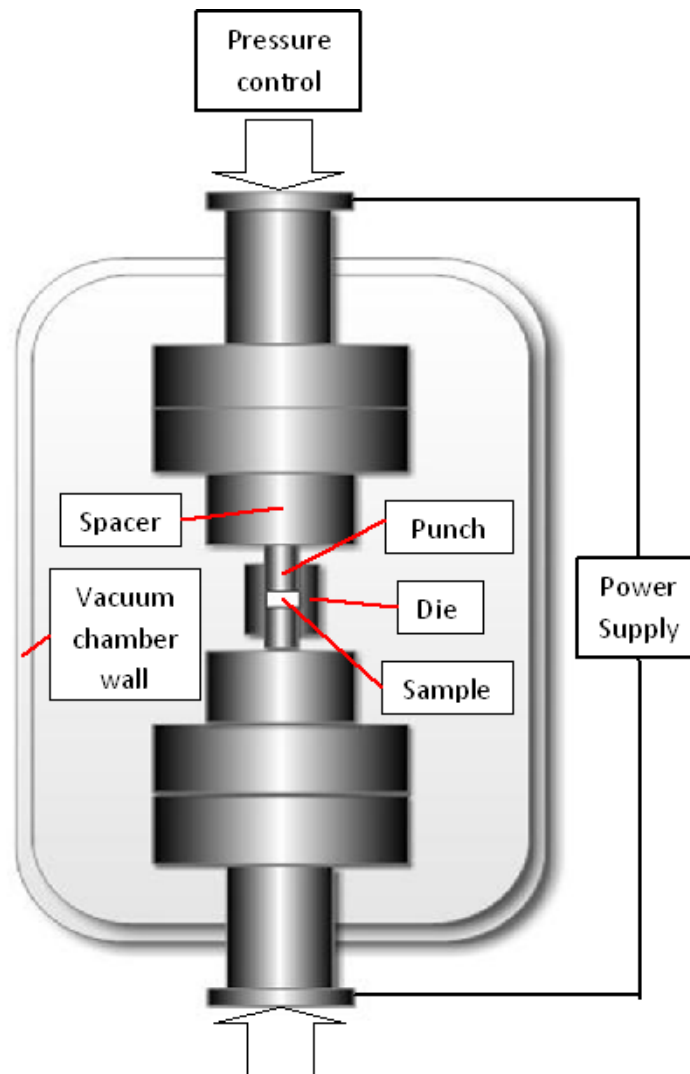


Figure 1-1. Schematic of the spark plasma sintering (SPS) apparatus.

Considerable benefits of the SPS technique over other conventional processing methods, i.e., hot pressing or hot isostatic pressing, such as relatively high heating rates and short holding times that allow the grain growth process to be minimized, have

already been demonstrated [3]. In addition, this technique has been extensively used to produce a wide range of materials, i.e., metals, ceramics, glass, biomaterials, and composites, with excellent properties [2, 4-8] that are often unattainable by other densification methods, especially for the production of bulk nano-structured materials [9-12]. The achievements during the past few decades show that the SPS technique has successfully accelerated the development of novel micro- and nano-structures. This success has been attributed to the following mechanisms of the SPS process: spark impact pressure, rapid Joule heating, powder surface activation caused by electrical discharge, in situ cleaning of grain boundaries and particle surfaces, enhancement of the surface diffusion, local melting and evaporation, and microscopic electrical discharge between particles [3, 13-15].

Despite the successful application of the SPS technique, there is still a large gap between the fundamental understanding of the principle mechanisms of SPS process mentioned above and the technological advancements garnered by this process [3]. Without a fundamental comprehension of the principle mechanisms, it is expected that further advancements in the state of the art will be significantly delayed. Therefore, more experimental and modeling work is urgently needed in order to obtain a clear insight into the process.

## **1.2 Experimental and Modeling Backgrounds**

The concept of applying an external electric current to assist sintering was first introduced by Taylor [16] in 1933 when he incorporated the idea of resistance sintering

into the hot pressing process of cemented carbides. However, due to the lack of fundamental understanding of the basic principles of this technique, as well as the poor condition of the energy supply, controlling systems, etc., sporadic progress of this technique was made in the following several decades. In the 1960s, Inoue [17, 18] proposed to utilize an electric discharge process to compact metallic materials in order to obtain a relatively high density. In the electric discharge process, different electric current waveforms, such as low-frequency AC, high-frequency unidirectional AC and/or pulsed DC, were adopted. This new basic sintering principle led to unprecedented technological innovations of the sintering techniques, and inspired the development of the subsequent spark plasma sintering technique. Based on the design of Inoue [17], the first commercially available spark plasma sintering machine was developed in Japan by Sumitomo Heavy Industries, Ltd. in 1990. The naissance of the machine greatly triggered interest in the SPS technique, and substantive progress has been made ever since.

### **1.2.1 Experimental Investigations**

As the SPS uses electric currents and moderate uniaxial pressures to densify powders, there are a number of mechanisms that can account for the enhancement of the sintering behavior. In order to gain a fundamental understanding of the principle mechanisms of SPS process, extensive experiments have been conducted in the past few years.

In 2004, Anselmi-Tamburini et al. [19] examined the effect of various SPS sintering parameters and claimed that the applied uniaxial pressure had a significant

influence on the final density, but no apparent effect on crystallite size. Munir et al. [3] pointed out that the increment of densification driving force due to the application of pressure could lead to a decrease in the sintering temperature, and thus limit grain growth. As with the conventional hot pressing process [20], the pressure can not only enhance the densification driving force and promote the densification kinetics [21], but also significantly influence the overall bulk electrical, thermal, and stress fields by changing the bulk material properties [22].

High heating rate, which can be achieved as high as 1000 °C/min, distinguishes the SPS technique from conventional hot pressing processes and has been investigated considerably for both pressure-less and pressure-assisted sintering. It is well recognized that the high heating rate plays an important role in enhancing densification while simultaneously limiting grain growth [23, 24]. However, such high heating rate can lead to large temperature gradients [25-29] that will result in differential densification and subsequent microstructure inhomogeneity in the powder compact, as well as graded mechanical properties [26]. In addition, studies on the densification of nano-size powders of fully stabilized zirconia [19] revealed that the heating rate had no significant influence on the final density.

As pointed out above, the major distinction between the conventional hot pressing process and SPS technique relates to the differences in heating rates, which are in turn, due to the different heating schemes adopted to heat the powder and the die [1, 3]. Specifically, in the hot pressing process, the punch/sample/die assembly is heated indirectly by radiation from an enclosing furnace, and eventually by convection and/or conduction. Thus, the heating rate is limited by the rate of radiation and/or convection

and conduction [1]. In the SPS process, however, high-density electric currents (usually pulsed DC) are allowed to pass through the punch and die, as well as the powder if it is conducting, with high heating rates obtained by Joule heating. The effects of pulse frequency on the density, electrical resistivity, and tensile properties of the powder compacts were investigated by Xie et al. [30], and the influences of the pulse frequency on the densification, deformation, and microstructure of the powder compacts sintered by SPS process were found to be not significant. Conrad [31] explored the effect of electric current on the flow stress of metals and fine-grained oxides. He claimed that the “electron wind” generated by electric current had a large effect on the plastic strain of metals, and high density electric current ( $10^3$ - $10^6$  A/cm<sup>2</sup>) could significantly increase the plastic strain of metals while a modest electric field with strength about 100-300 V/cm was enough to substantially reduce the flow stress of fine-grained oxides. Additionally, Chen et al. [32] investigated the effect of pulsing on the reactivity between silicon (Si) and molybdenum (Mo), Anselmi-Tamburini et al. [33] studied the influence of the current on the diffusion kinetics of the reaction between Si and Mo layers. Their work showed there was an enhancement in reactivity kinetics in the presence of current, but no noticeable effect of pulsing was observed. However, the pulsed DC current was thought to induce another non-thermal effect - creating plasma, and that was the reason why the process was named spark plasma sintering. The plasma was deemed to cause a cleansing effect on the particle surfaces, and lead to sintering enhancement [34-36]. Nevertheless, more recent experimental results by Hulbert et al. [14, 15] showed that plasma, sparking, or arcing was not generated during the SPS process. He recommended that other salient factors of the SPS process might play a more important role than previously thought, and more

fundamental research needed to be conducted in order to understand the underpinnings of the sintering mechanisms of the process.

### **1.2.2 Computational Modeling**

In addition to the extensive experiments that have been done in the past several years, considerable efforts also have been made to simulate the SPS process and investigate the underlying mechanisms that contribute to the enhanced sintering of SPS over traditional sintering techniques [2, 3].

Early attempts were performed to simulate the temperature and current distributions in the SPS. In 2002, Wang et al. [37] used analytical solutions of the one-dimensional Fourier equation to calculate temperature differences in the die and sample. Based on the Ohm's and Fourier's laws, Matsugi et al. [38, 39] investigated the voltage and temperature distributions in the punch/sample/die assembly by employing the finite difference method to perform a thermal-electric analysis. In his study, titanium and alumina powder compacts were considered, and the results showed that both temperature and voltage distributions were affected by the different properties of compacts. However, this model was limited to steady-state conditions. Wang et al. [40] applied the commercial software ANSYS to simulate the SPS process with only the temperature field in the punch/sample/die assembly studied. The first thermal-electric coupling analysis of the SPS process was performed using ABAQUS by Zhang [41] and Zavaliangos et al. [42]; the entire SPS system was modeled with special attention paid to contact resistances. Anselmi-Tamburini et al. [43] used the CFD-ACE+ code to examine the

effect of the electrical and thermal conductivities of the powder compact on current and temperature distributions. The influences of the electrical properties of the samples and the thermal and electrical contact resistances on temperature gradients within the sample was evaluated by Vanmeensel et al. [44]. In addition, McWilliams et al. [45] systematically investigated the effects of the dimensions of punch and die and the heating rate on temperature distribution in the SPS system with tungsten powder compact. Cincotti et al. [46] simulated the temperature evolution in the system, and constructed a function which related the electric and thermal resistances in horizontal contacts to temperature and externally applied load. More recently, Maizza et al. [47, 48] developed a SPS finite element model using the COMSOL software that included a moving mesh technique to account for the contact resistance which varied with punch sliding. Rathel et al. [49] studied the temperature distribution for both electrically conductive and non-conductive samples during SPS, and concluded that the electrical conductivity of the samples, SPS system design, and setup strongly influenced the temperature distribution. Tiwari et al. [50] also assessed the effects of power input, thermal conductivity of powder compact, and sintering time on both thermal and electric field evolution. All of these models were qualitatively consistent and agree with the experiments. Nevertheless, mechanical aspects such as the evolution of stress distributions have been neglected in these models.

As demonstrated in [21], the externally applied pressure, which is one of the main control parameters in SPS process, is of crucial importance to the materials with tailored properties. Thus, unforeseen stress distributions, as the temperature distribution, can play an important role in the densification process, and consequently need to be investigated

carefully. Recently, Wang et al. [51] constructed a finite element model that can be used to simulate a three-way coupling of electrical, thermal, and mechanical behaviors at low temperature ( $<700$  °C) during the SPS process, and concluded that the displacement and stress distributions were dependent on the sample properties. Based on the work of Wang et al. [51], Antou et al. [52] developed another finite element model in which pure slip without mechanical friction at the sample/graphite die interfaces was considered in order to simulate the current, temperature, and stress distributions during SPS treatment of zirconium oxycarbide. The results showed that both thermal and stress gradients appeared in the sample during SPS treatment. However, the stress gradients were significantly larger than the thermal ones. Sample properties, such as the coefficient of thermal expansion and elastic modulus, as well as temperature exerted a strong influence on the magnitude of the stresses.

However, attempts to incorporate the densification effect in the modeling have been limited to date. McWilliams et al. [53, 54] developed a two-part finite element approach that can account for the evolution of material properties due to densification and the displacement of punches during the SPS process. In his model, the temperature was first obtained from the thermal-electric simulation. Based on the temperature profile of the sample, the sintering simulation was conducted to track the local relative density and estimate the shape and volume evolution of the sample. According to the estimated information, material properties such as thermal and electrical conductivity, and the mesh were updated and fed to a new thermal-electric simulation and the process was iterated. The modeling results showed that variances in local densities and material properties can dramatically affect the overall sintering behavior of the sample. Even so, only a single

sample free from external pressure and constraints can be simulated by this model and no information about stress distributions was reported. Similar to [53, 54], Maizza et al. [48] developed a combined experimental/modeling methodology which was used to simulate the temperature and current distributions during the SPS sintering process and estimate the contact resistance of the entire SPS system. Nevertheless, emphasis was placed on the contact resistance of the SPS system while the evolution of stress was still not investigated.

### **1.3 Scope of the Thesis**

Despite the significant advantages of SPS over other conventional densification methods [3], the temperature and/or stress heterogeneities in the SPS sintered samples, which can be attributed to the coupling effects of high heating rates [26-29] and the thermal [50] and electrical [44, 49] conductivities of the samples, can be a serious handicap for the further advances of this technique. This is especially true when SPS is applied to the production of very large or net-shaped components [55]. Thus, a precise understanding of the cause of potential temperature and stress heterogeneities is badly needed in order to overcome these challenges and ensure fully sintered materials with more uniform properties. For this reason, the investigation of the parameters that influence the current, temperature, and stress distributions and their time evolution are urgently required and will be extremely useful for the continuing development of the SPS process.

In the present study, a finite element model, which is capable of simulating the three-way coupling of thermal, electrical, and mechanical behavior of the SPS process, was developed using the commercially available ANSYS software for the purpose to obtain a precise insight of the cause of potential temperature and stress heterogeneities. Samples made from different materials, including alumina, ceria, copper, and tungsten with different aspect ratios (the ratio between the height and the radius of the sample) were used in the simulation. Utilizing these parameters, the influences of material properties and aspect ratios on the temperature and stress distributions were then systematically investigated. In addition, an integrated experimental/numerical methodology was proposed, and the densification effect on the temperature and stress distributions was also considered by taking into account the temperature-density dependent properties of the sintering material. The model and the results provided herein are of paramount importance for understanding the phenomena in the SPS process, and can be used for the SPS system design and process optimization that could subsequently lead to the reliable production of sintered structures with controlled and tailored properties.

The remainder of this thesis has been arranged as follows: in Chapter 2, the influences of the aspect ratios and material properties of the samples on the temperature distribution are investigated; the stress distributions will be examined in Chapter 3; in Chapter 4, the densification effect on the temperature and stress distributions is uncovered; finally, the major results and conclusions from the current study are summarized in Chapter 5, and possible future studies are also discussed.

## **Chapter 2**

### **Coupled Thermal-Electric Field Analysis**

#### **2.1 Introduction**

In the three-way thermal, electrical, and mechanical coupling model used in this study, the coupling between electrical potential and temperature is strong because of the relatively high dependence of thermal and electrical coefficients on the temperature. However, the thermal and electrical coefficients are assumed to be unaffected by the stress which is generated by the external pressure and thermal expansion effect, as previously considered in [51, 52]. Thus, the three-way coupling model can be decoupled into thermal-electric and thermal-mechanical modules. In this chapter, the thermal-electric portion of the three-way coupling model is introduced, and the influences of material properties and aspect ratios of different samples on the temperature distribution are investigated.

#### **2.2 Finite Element Modeling Details**

##### **2.2.1 Theory**

For thermal-electric coupling problems, the electrical potential and temperature distributions are governed by the following system of simultaneous partial differential equations [51]:

$$\nabla \cdot \vec{J} = 0 \quad (2-1)$$

$$\nabla \cdot \vec{f} + \rho c_p \frac{\partial T}{\partial t} = q_e \quad (2-2)$$

where  $\vec{J} = \sigma \vec{E}$  is the current density,  $\sigma$  is the electrical conductivity, and  $\vec{E}$  is the electric field intensity defined as  $\vec{E} = -\nabla \phi$ , where  $\phi$  is the electric potential. In addition,  $\vec{f} = -\lambda \nabla T$  is the heat flux density,  $T$  is the temperature, and  $\lambda$  is the thermal conductivity,  $\rho$  is the density,  $c_p$  is the specific heat capacity, and  $q_e$  is the heat generated by the flowing current per unit volume per unit time. According to the Joule's law,  $q_e = \vec{J} \cdot \vec{E} = JE$ .

Substituting  $\vec{J} = \sigma \vec{E}$ ,  $\vec{f} = -\lambda \nabla T$ , and  $q_e = JE$  into Equations (2-1) and (2-2), the governing equations of the coupled system can be written as:

$$\nabla \cdot (-\sigma \nabla \phi) = 0 \quad (2-3)$$

$$\nabla \cdot (-\lambda \nabla T) + \rho c_p \frac{\partial T}{\partial t} = JE \quad (2-4)$$

### 2.2.2 Numerical Implementation

A schematic representation of the SPS apparatus used in the simulation is shown in Figure 2-1. As depicted in the figure, the spacers, die, and punches are made of graphite while the outer die surface is covered by graphite felt. Due to the axial symmetry of the system, only one half of the cross section of the system was modeled; this plane

axisymmetric model is controlled by the governing Equations (2-3) and (2-4) which involve a dynamic coupling of the charge conservation and Fourier's laws. As such, the simplified and coupled partial differential equations describing the SPS process, together with the associated boundary and initial conditions, were then solved using the finite element package ANSYS. Samples made from different materials, including alumina, ceria, copper, and tungsten with different aspect ratios (the ratio between the height and the radius of the sample) of 0.5, 1.0, and 1.5 were used in the simulation. These aspect ratios were achieved by changing the heights of the samples while keeping the radii unchanged.

The thermal and electrical properties of the graphite die, spacers, punches, and felt were all assumed to be spatially uniform and consequently, treated as an isotropic medium in the model. In addition, the sintering samples, which were composed of alumina, ceria, copper, and tungsten, were also modeled (at least initially) as isotropic and fully dense solids; all of the pertinent physical properties of the sintering materials and graphite portions of the die are comparatively listed in Appendix A. It should be noted that any changes to the listed properties occurring during the densification process were not considered in the model at this point. Hence, this model only simulates their thermal and electrical behaviors at the final stage of SPS sintering. However, such changes of material properties due to densification effect are considered in Chapter 4.

The initial and boundary conditions used to carry out the numerical analysis via finite elements were as follows: (a) the initial temperature of the entire system was  $T_0 = 27\text{ }^\circ\text{C}$ ; (b) the process takes place in vacuum so heat losses by conduction or convection through the gas were neglected. However, all of the lateral surfaces can

experience heat losses via radiation towards the chamber walls which were held at room temperature (i.e.,  $T_0 = 27^\circ\text{C}$ ). Using a radiation model, all of the corresponding heat flux per unit area,  $q_r$ , was given by  $q_r = \varepsilon\xi(T_w^4 - T_0^4)$ , where  $\varepsilon$  is the emissivity and is assumed to be equal to 1 in this analysis,  $\xi$  is the Stefan-Boltzmann constant,  $T_w$  is the temperature of the die surface, and  $T_0$  is the temperature of the chamber walls; (c) the temperature of the two extreme upper and lower spacer surfaces was also fixed at  $T_0 = 27^\circ\text{C}$ ; (d) the current flux can be considered for two operational modes, constant voltage or constant current. For the current study, a constant current mode (800 A) was used, and the thermal and electrical contact resistances were also neglected at all pertinent interfaces.

An adaptive mesh was used in the plane axisymmetric model shown in Figure 2-1: a fine mesh was used in the center areas corresponding to the sample, die, and punches. Coarser mesh was used in the spacer area. As such, the total number of elements used in the analysis was approximately 50,000, with variations occurring due to the changing of dimension of samples as the systematic study of varying materials and aspect ratios was conducted. By using the data published in [43, 51], the validation of this model was checked, and the constructed SPS model was shown to be reliable enough to be used in the further simulation.

## 2.3 Results and Discussion

The simulated temperature evolution at the center points of different samples with aspect ratios of 0.5, 1.0, and 1.5 is plotted in Figure 2-2 for the 800 A constant DC current. As shown in these figures, the temperature in each sample reaches a steady state after the application of the current for more than 800 s. Thus, in the following discussion, the steady-state temperature distribution at 1000 s is reported.

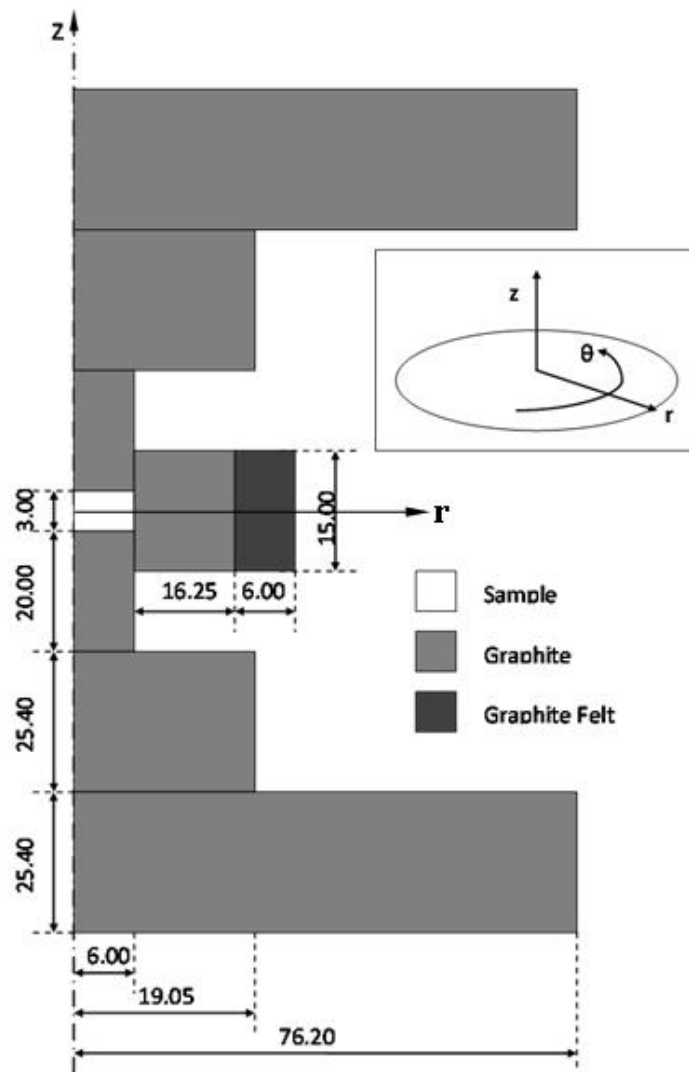


Figure 2-1. Schematic of the SPS apparatus showing dimensions (in millimeter) and coordinate system with origin at the middle of the sample.

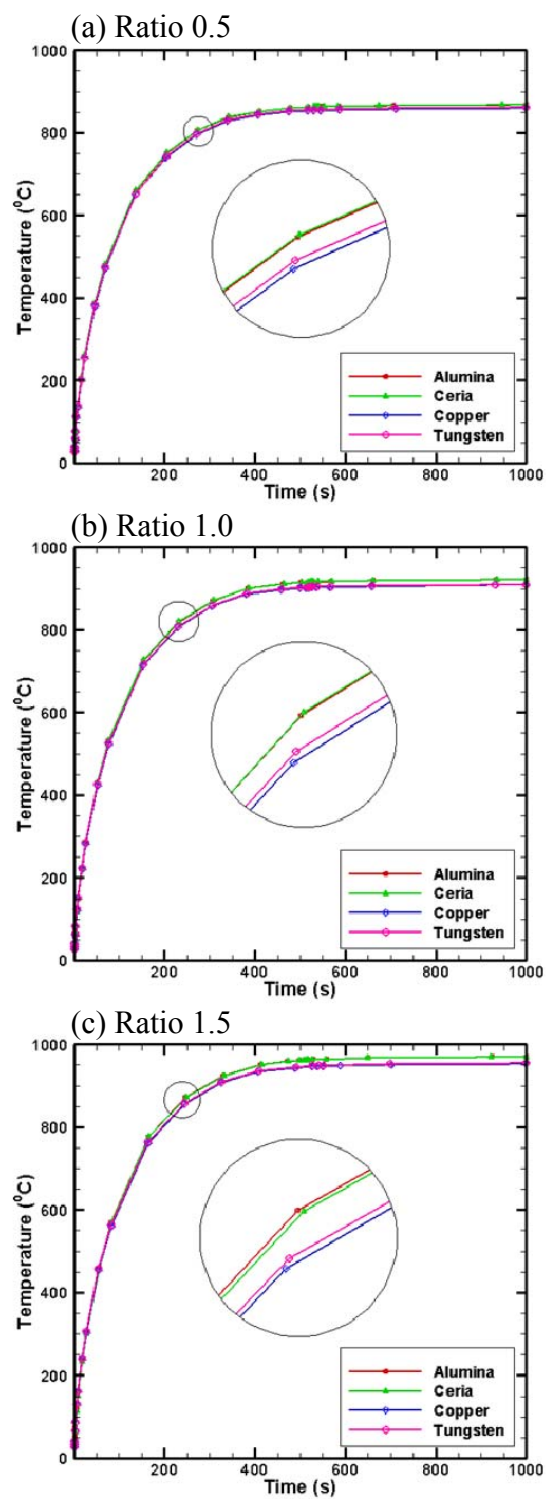


Figure 2-2. Temperature evolution at the center points of the samples with the same aspect ratios: (a) Ratio 0.5, (b) Ratio 1.0, and (c) Ratio 1.5.

### 2.3.1 Influence of Aspect Ratios

As a general rule, the temperature distribution in the SPS system is affected by the coupling effects, characterized on one hand, by the Joule heating mechanism within the graphite punches and die, and the sample if it is electrically conductive, and on the other hand, by the heat transfer mechanism within the system [52].

Contour plots of steady-state temperature distribution in the region of the punch/sample/die assembly with different sample aspect ratios, namely 0.5, 1.0, and 1.5, are shown in Figures 2-3 to 2-6; Figures 2-3 and 2-4 are for the electrically non-conductive alumina and ceria samples, while Figures 2-5 and 2-6 are for the conductive copper and tungsten, respectively. All contours are plotted in the same scale for the purpose of comparison. The temperature profiles in the radial and vertical direction of the punch/sample/die assembly are also shown in Figures 2-7 and 2-8, respectively. According to the simulation results, the highest temperatures in the system are always developed in the portion of the punch which is just enclosed by the graphite die, despite the changing of the sample aspect ratios. The reason for this is that the resistance of the punch is high due to its small diameter. Meanwhile, the small diameter of the punch can also result in a large current concentration in the region exposed outside the die, which subsequently causes an intensive local Joule heating in the corresponding part of the punch. However, due to the heat transfer mechanism, the generated heat is partially diffused into the sample and partially lost into the upper and lower spacers that are water cooled. In addition, surface radiation accounts for additional heat losses from all exposed

surfaces. Thus, the highest temperature can only appear in the portion of punch which is just enclosed by the graphite die.

As the sample aspect ratio (the ratio between the height and the radius of the sample) increases, so does the surface area of the two punches now exposed to conditions outside of the die. Therefore, more heat is generated in these regions by local Joule heating. Even though a small portion of the heat is lost because of radiation, the majority is conducted to the sample, die, and spacers to increase the temperature of the whole system. Consequently, the greater the aspect ratio of the sample, the higher the maximum overall temperature of the system.

In order to obtain more detailed information about the temperature gradients in the sample, the temperature distribution for the various materials studied are shown in Figures 2-9 to 2-12 using the same scale. In addition, Figures 2-13 and 2-14 show the temperature profiles in both radial and vertical directions of the sample, respectively. The minimum and maximum temperatures in the sample are also listed in Table 2-1.

As shown by the results, the temperature and corresponding gradients are directly proportional to the sample aspect ratio; namely, the larger the aspect ratio, the higher the maximum temperature in the sample, and the larger the temperature gradients. As evidenced by the results, the gradients become more severe with the increment of the aspect ratio, especially in the vertical direction. The gradient in the radial direction is thought to be correlated to the radiation losses from the graphite die surfaces which are especially significant at high temperatures [42]. However, the temperature gradient in the vertical direction can be attributed to the thermal and electrical material properties of the sample, which will be discussed in the next section.

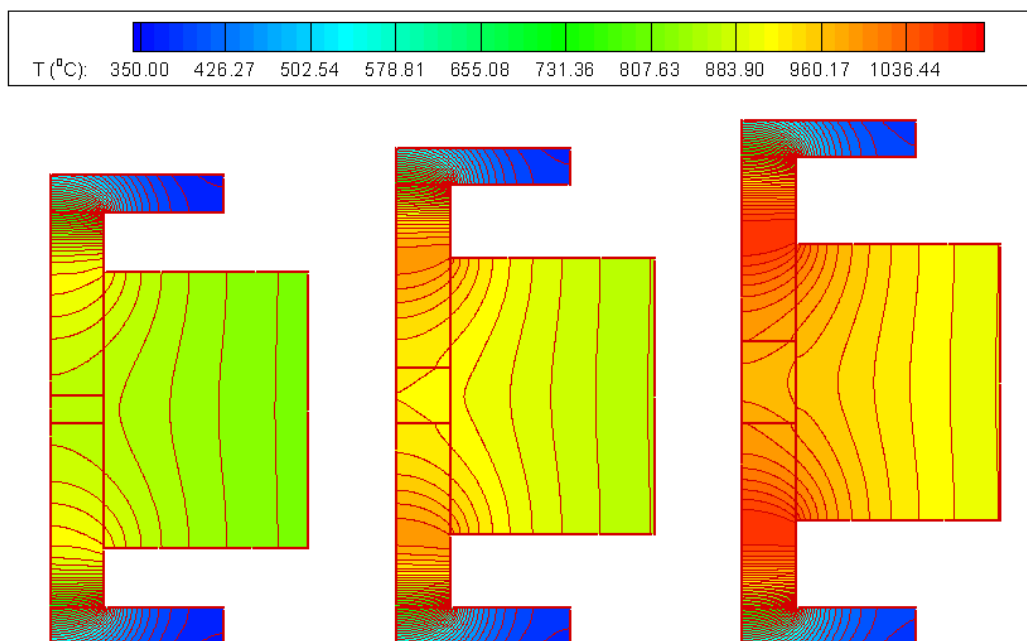


Figure 2-3. Steady-state contour plots of the temperature distribution in the punch/sample/die area of alumina samples with different aspect ratios: 0.5 (left), 1.0 (middle), and 1.5 (right).

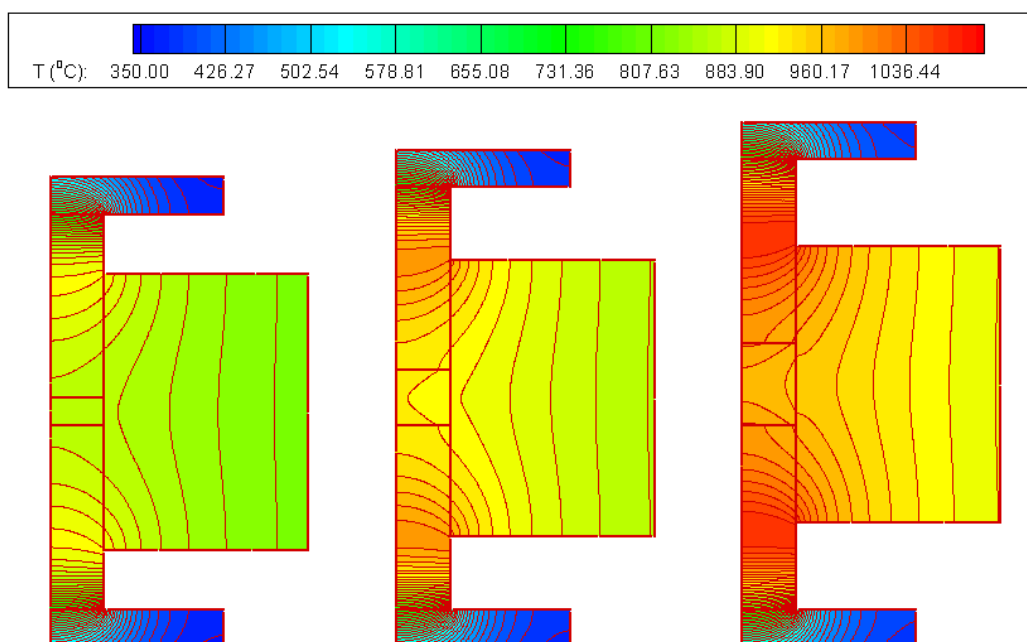


Figure 2-4. Steady-state contour plots of the temperature distribution in the punch/sample/die area of ceria samples with different aspect ratios: 0.5 (left), 1.0 (middle), and 1.5 (right).

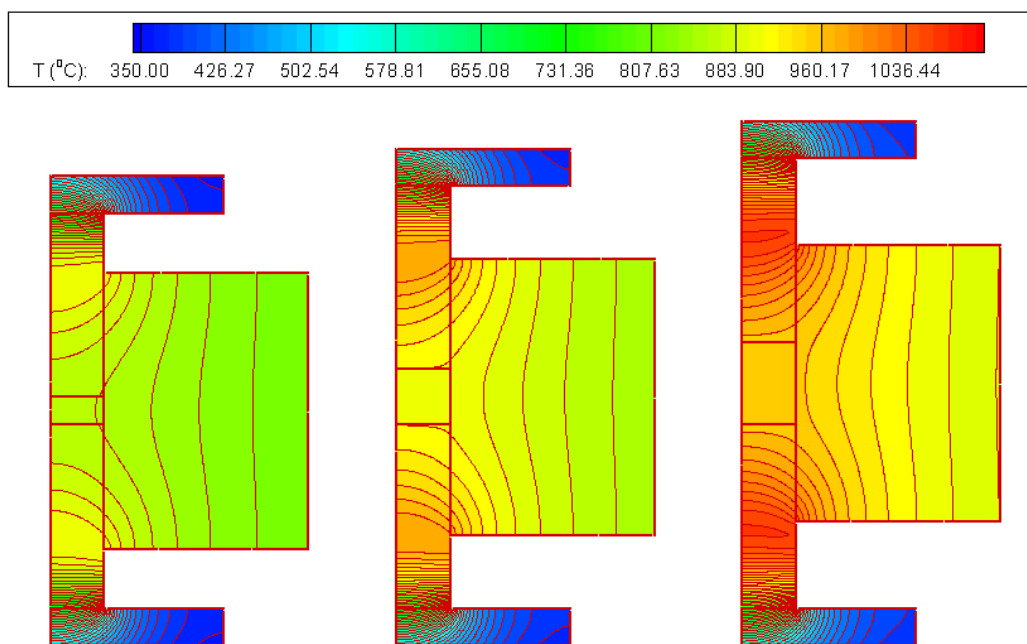


Figure 2-5. Steady-state contour plots of the temperature distribution in the punch/sample/die area of copper samples with different aspect ratios: 0.5 (left), 1.0 (middle), and 1.5 (right).

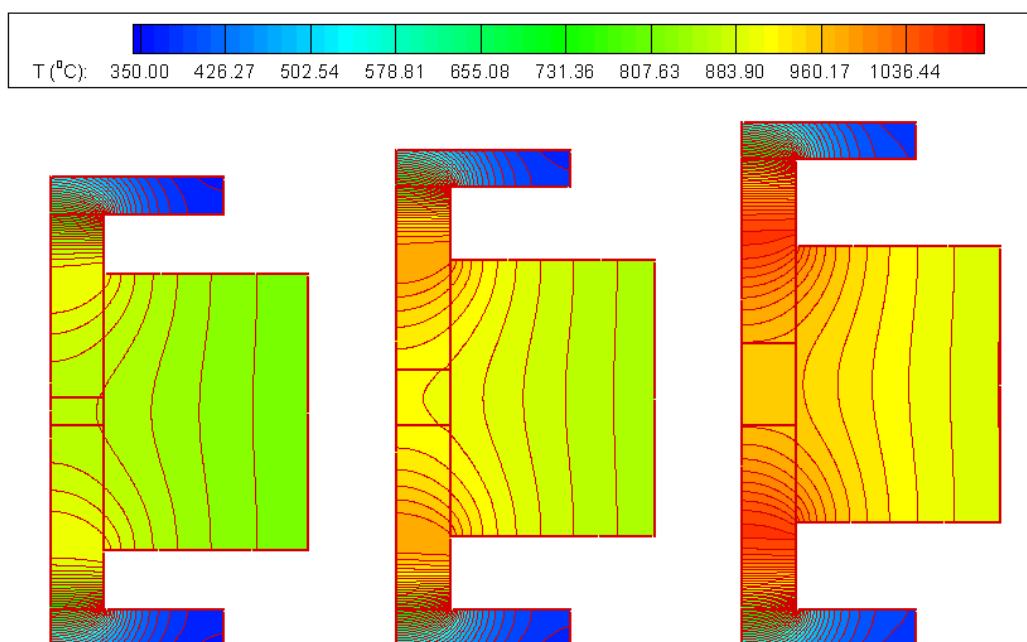


Figure 2-6. Steady-state contour plots of the temperature distribution in the punch/sample/die area of tungsten samples with different aspect ratios: 0.5 (left), 1.0 (middle), and 1.5 (right).

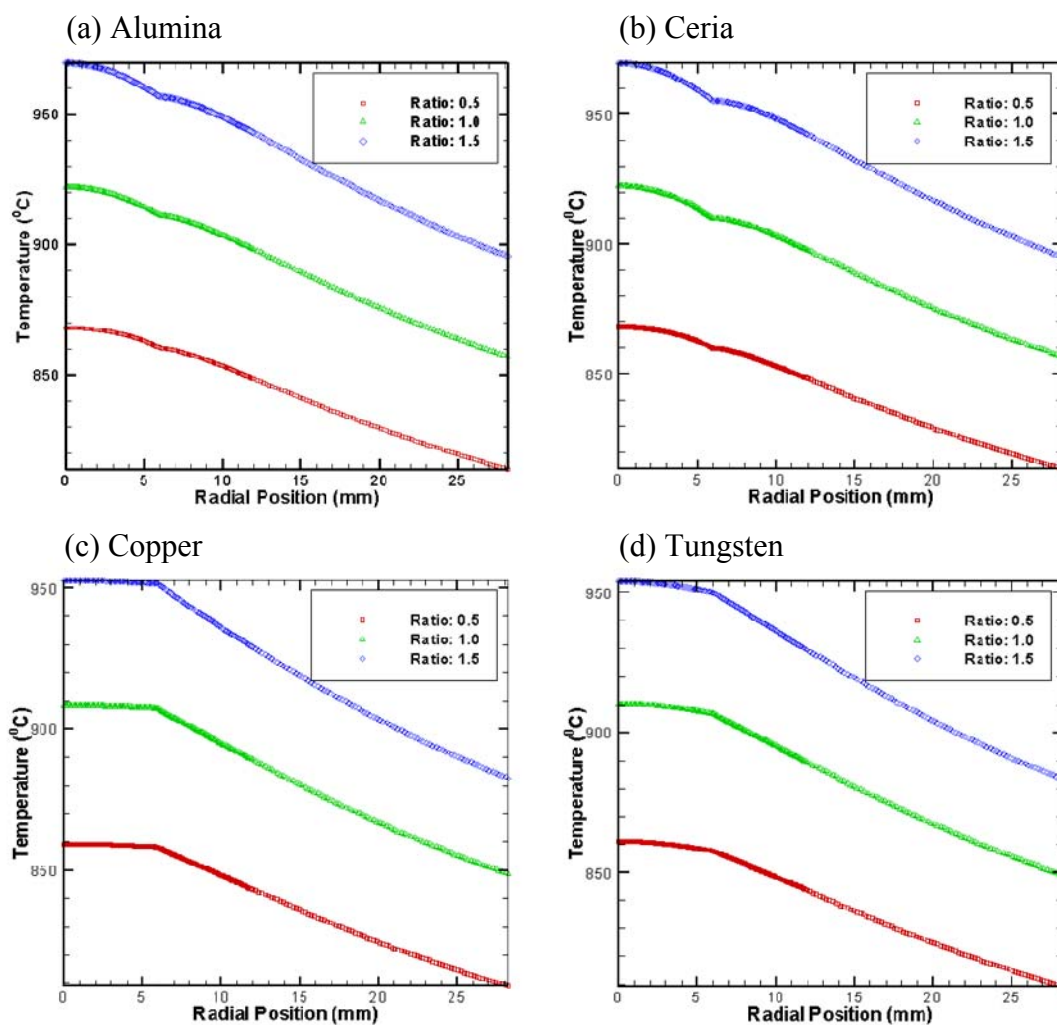


Figure 2-7. Comparison of the steady-state radial temperature profiles in the middle cross-section of the sample and the die for: (a) Alumina, (b) Ceria, (c) Copper, and (d) Tungsten.

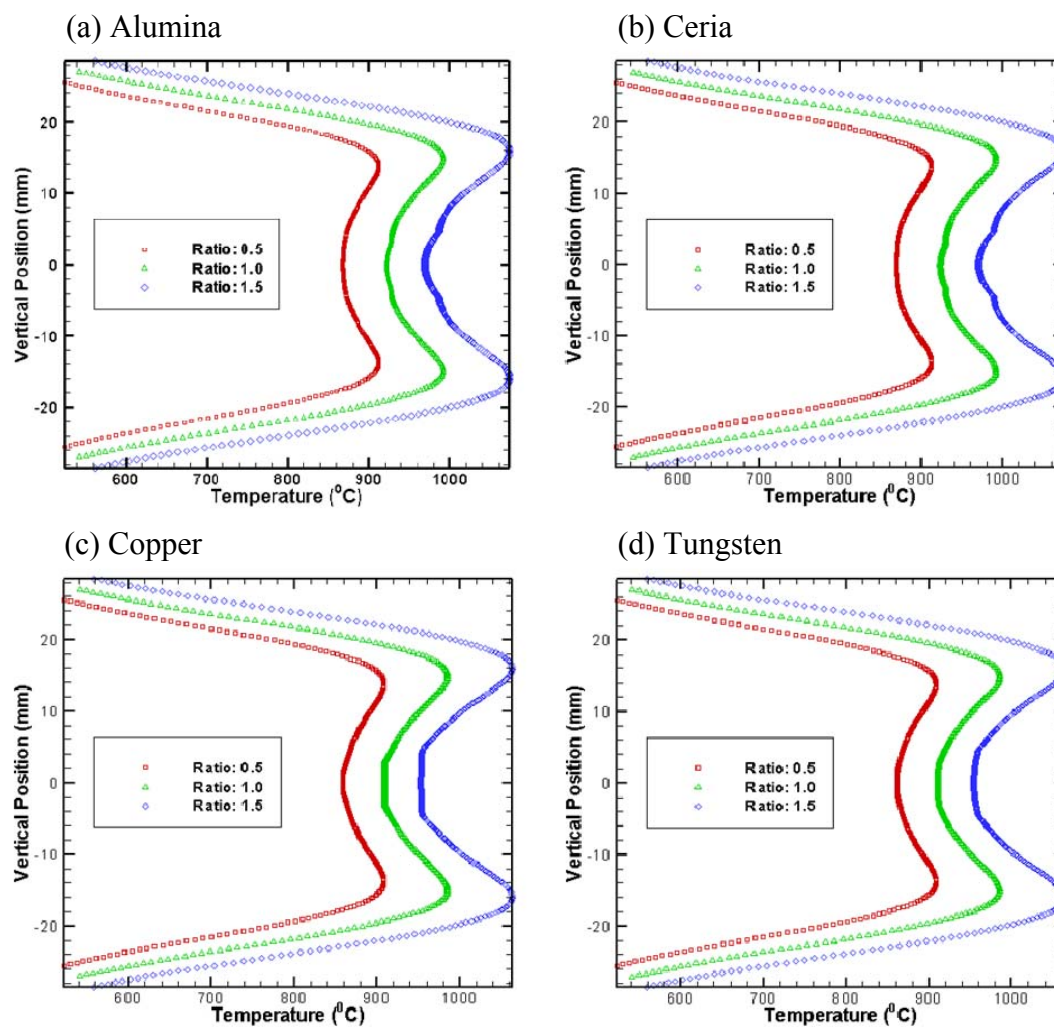


Figure 2-8. Comparison of the steady-state vertical temperature profiles along the axis of symmetry in the punch/sample/die assembly for: (a) Alumina, (b) Ceria, (c) Copper, and (d) Tungsten.

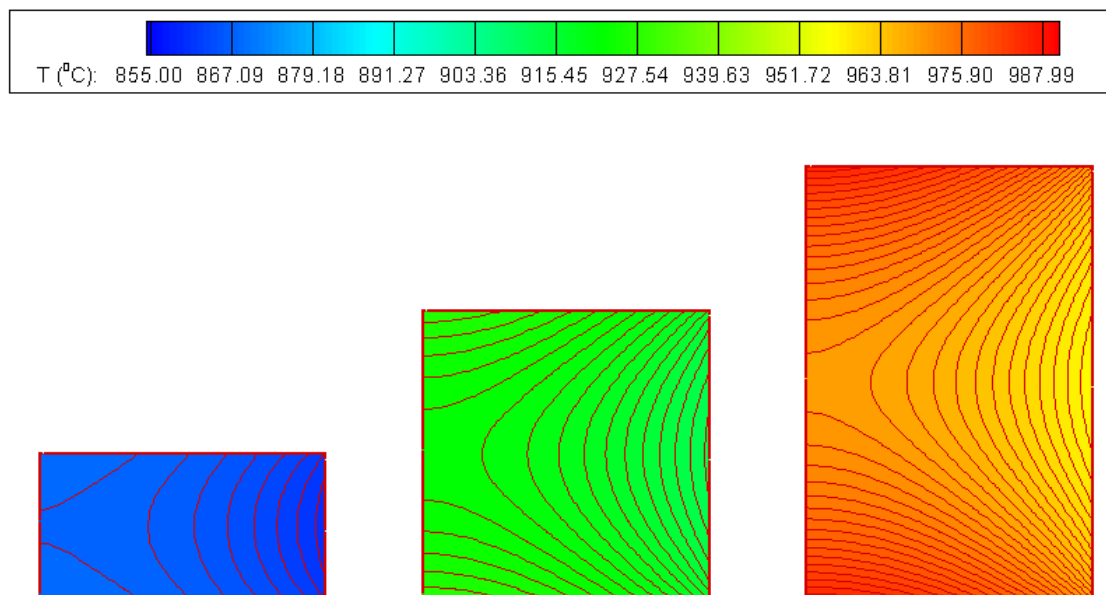


Figure 2-9. Steady-state contour plots of the temperature distribution in the region of alumina samples with different aspect ratios: 0.5 (left), 1.0 (middle), and 1.5 (right).

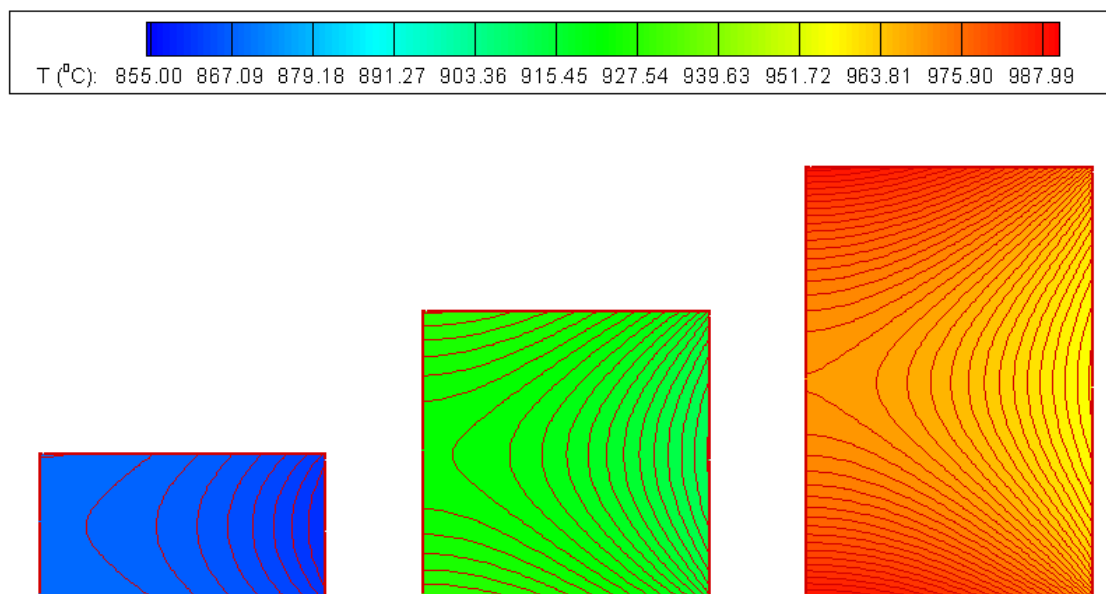


Figure 2-10. Steady-state contour plots of the temperature distribution in the region of ceria samples with different aspect ratios: 0.5 (left), 1.0 (middle), and 1.5 (right).

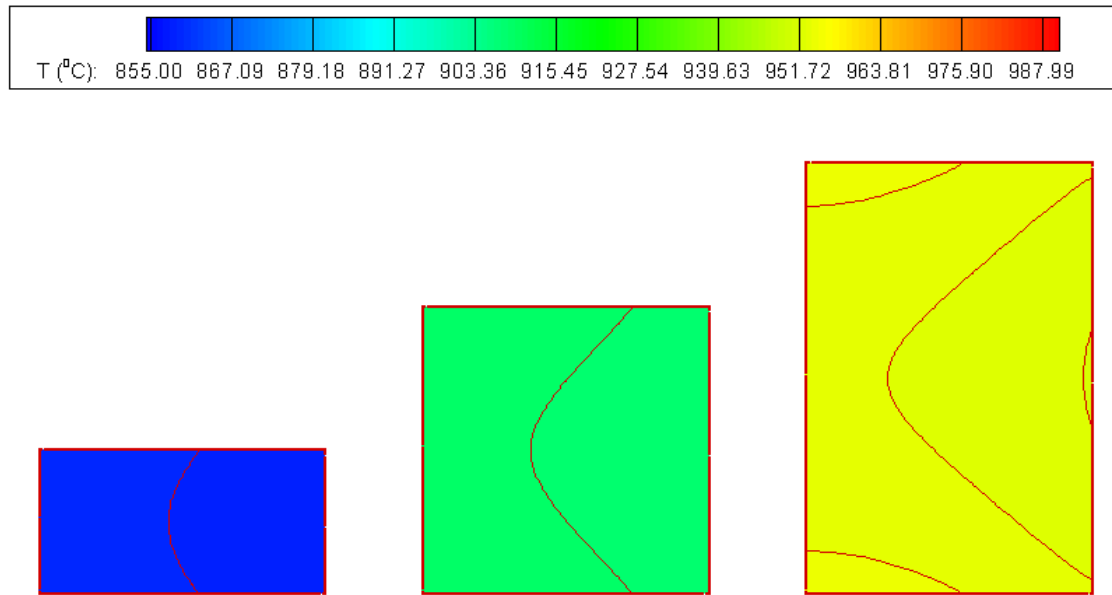


Figure 2-11. Steady-state contour plots of the temperature distribution in the region of copper samples with different aspect ratios: 0.5 (left), 1.0 (middle), and 1.5 (right).

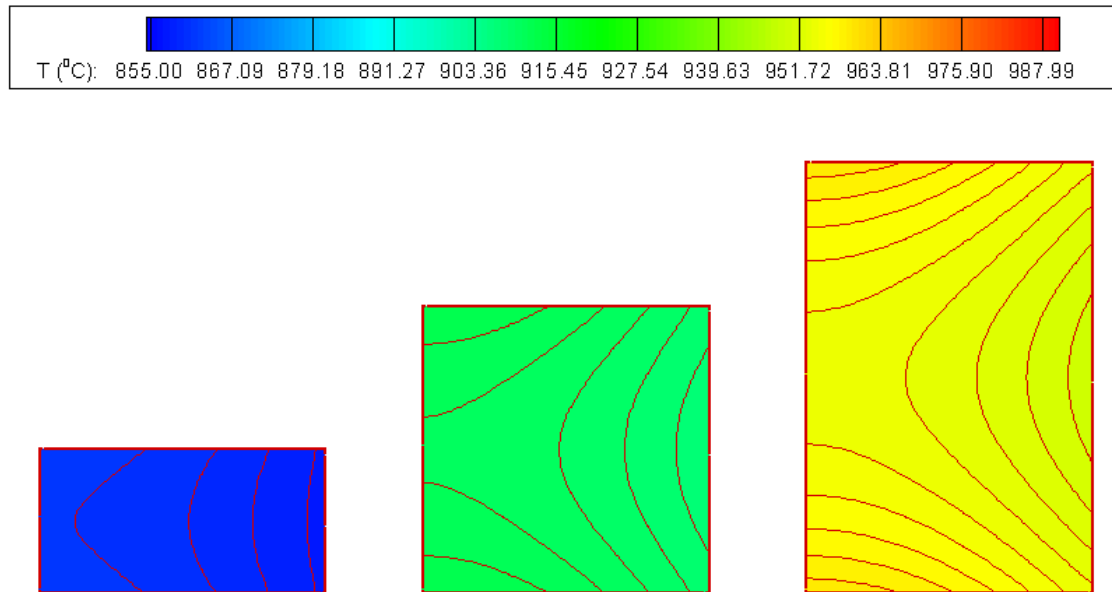


Figure 2-12. Steady-state contour plots of the temperature distribution in the region of tungsten samples with different aspect ratios: 0.5 (left), 1.0 (middle), and 1.5 (right).

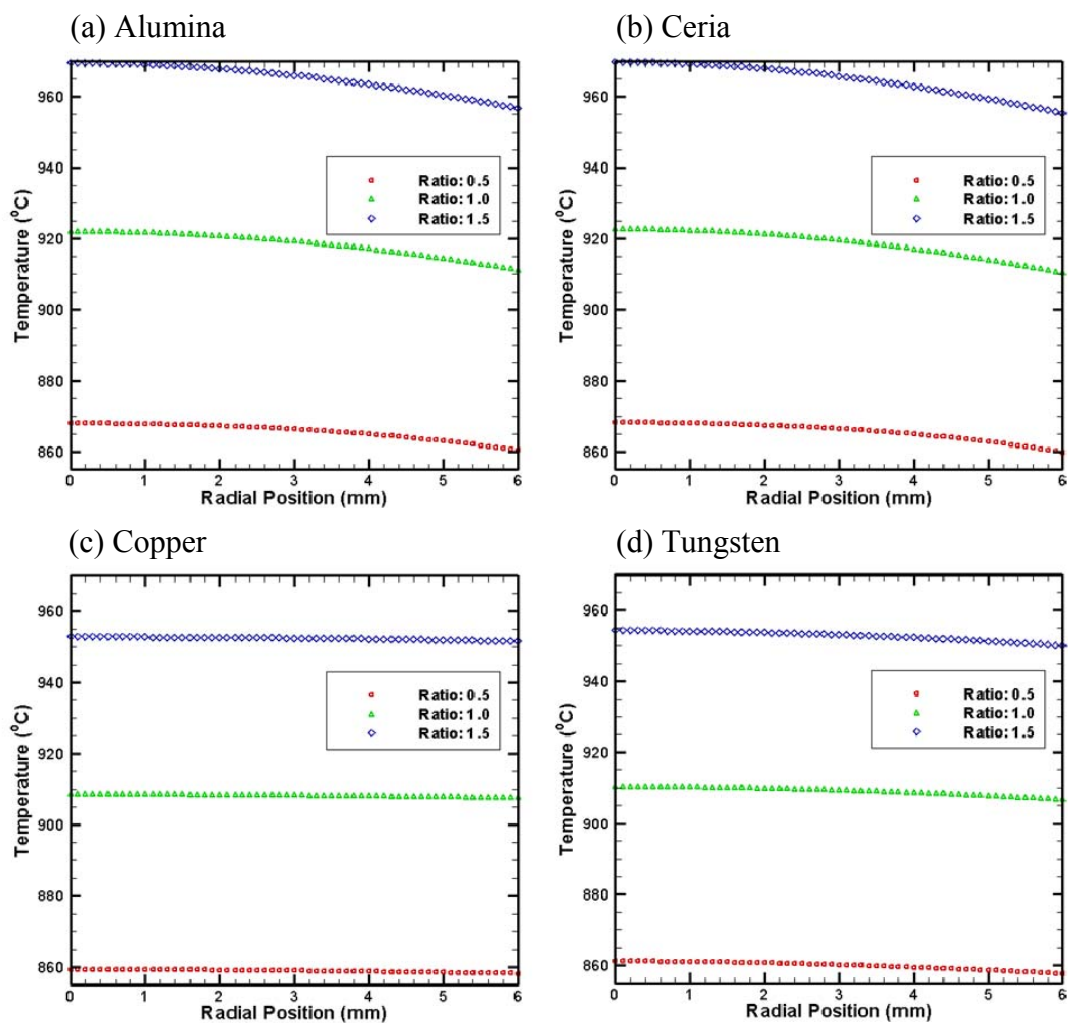


Figure 2-13. Comparison of the steady-state radial temperature profiles in the middle cross-section of the sample for: (a) Alumina, (b) Ceria, (c) Copper, and (d) Tungsten.

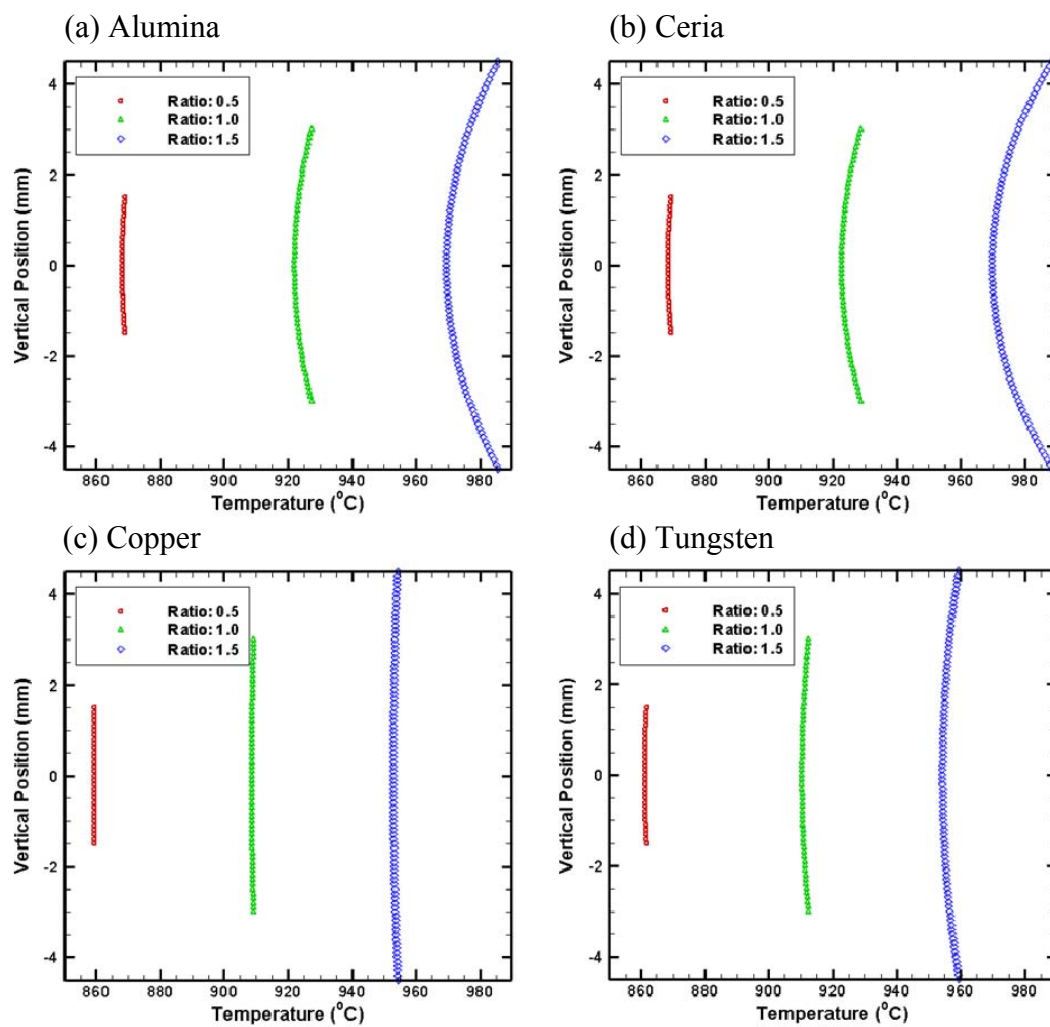


Figure 2-14. Comparison of the steady-state vertical temperature profiles along the axis of symmetry in the sample for: (a) Alumina, (b) Ceria, (c) Copper, and (d) Tungsten.

Table 2-1. Minimum and maximum temperature in the sample region ( $^{\circ}\text{C}$ ).

Sample	0.5		1.0		1.5	
	$T_{\min}$	$T_{\max}$	$T_{\min}$	$T_{\max}$	$T_{\min}$	$T_{\max}$
Alumina	860.45	868.87	911.07	927.36	956.79	985.75
Ceria	859.87	869.16	910.20	928.72	955.39	988.61
Copper	858.18	859.48	907.53	909.18	951.64	954.29
Tungsten	857.65	861.63	906.64	912.40	950.02	959.52

### 2.3.2 Influence of Material Properties

In Figure 2-15, the steady-state temperature profiles in the middle cross-section of the sample/die region for the electrically non-conductive (alumina and ceria) and conductive (copper and tungsten) samples with different aspect ratios are plotted. Figure 2-16 also shows the profiles in the vertical direction along the axis of symmetry in the punch/sample/die assembly. Comparisons show that the thermal and electrical properties of the sample have an important influence on the temperature distribution in the SPS system, especially in the sample region. With the rise of the temperature of the whole SPS system due to the increment of the sample aspect ratio, the discrepancies of both radial and vertical temperature distributions in the punch/sample/die assembly between the conductive and non-conductive sample cases increase significantly.

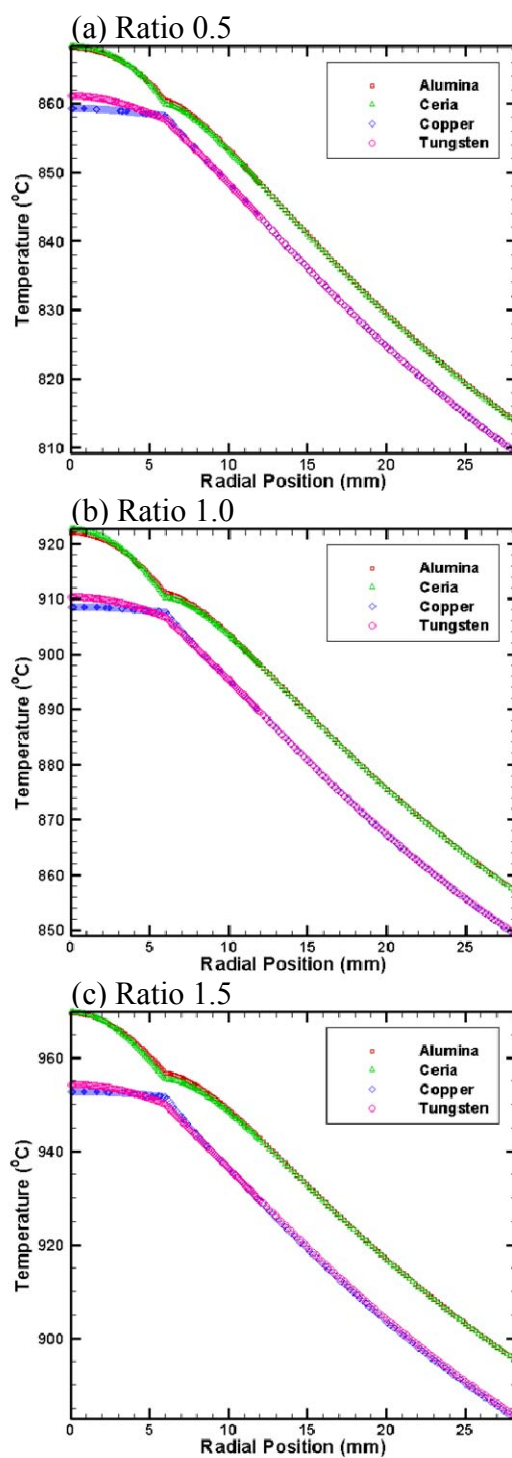


Figure 2-15. Comparison of the steady-state radial temperature profiles in the middle cross-section of the sample and the die with the same sample aspect ratios: (a) Ratio 0.5, (b) Ratio 1.0, and (c) Ratio 1.5.

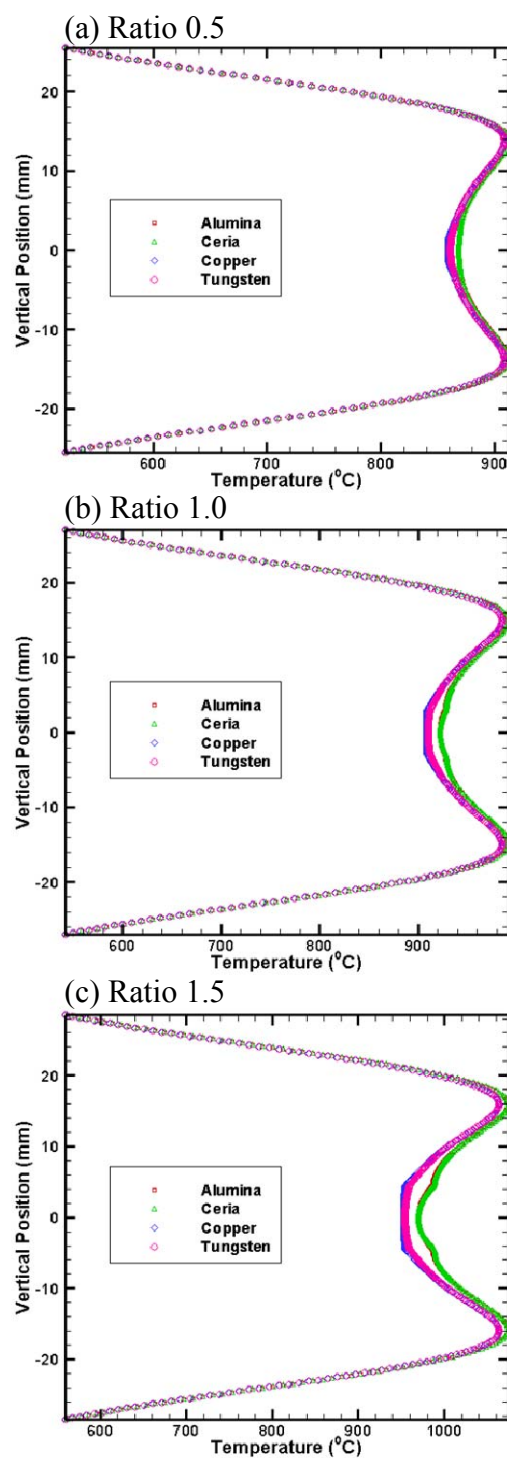


Figure 2-16. Comparison of the steady-state vertical temperature profiles along the axis of symmetry in the punch/sample/die assembly with the same sample aspect ratios: (a) Ratio 0.5, (b) Ratio 1.0, and (c) Ratio 1.5.

Figures 2-17 to 2-21 reveal that, at steady state, both the radial and vertical temperature gradients inside the electrically insulating samples (alumina and ceria) are much larger than in the conductive ones (copper and tungsten). This observation can be explained by the difference in thermal and electrical properties of the samples; for a good electrical conductor such as copper or tungsten, the main portion of the current flows through the sample. The contribution of the current to Joule heat generation in the sample region is negligible [43] due to the low electrical resistance of the sample. However, exceptions have been seen during the initial stage of the sintering process. In the case of a strong electrical insulator such as alumina or ceria, current is forced to flow through the die and no current passes through the sintering material. Thus, regardless of the electrical conductivity of the samples, the Joule heat of the SPS system is mainly generated in the graphite, particularly the punches; all the samples are heated up by the energy conducted from the punches and die.

As stated above, the current is forced to pass through the die for non-conductive sample cases. Hence, a relatively large amount of the Joule heat generated in the die can be used to counteract the heat losses due to radiation from the surfaces of the outer die. For the conductive samples, the Joule heat generated in the die is not sufficient as the main portion of the current passes through the sample instead of the die. Therefore, substantial heat has to be transferred from the punches and sample to the outer die to compensate for the heat losses on the radiation surfaces. This is the reason why the temperature in the entire assembly with a conductive sample is comparatively lower than an assembly with a non-conductive sample material as clearly shown in Figures 2-15 to 2-21.

In addition to the electrical characteristics, the thermal properties of the samples also play an important role in the temperature distribution in the SPS system. As the heat in both electrically non- and conductive samples is transferred from the punches and die, the thermal conductivity of the samples determines the resulting temperature gradients. The simulation results shown in Figures 2-15 to 2-21 reveal that the temperature gradients in the punch/sample/die assembly are higher for sample with higher aspect ratio and/or lower thermal conductivity.

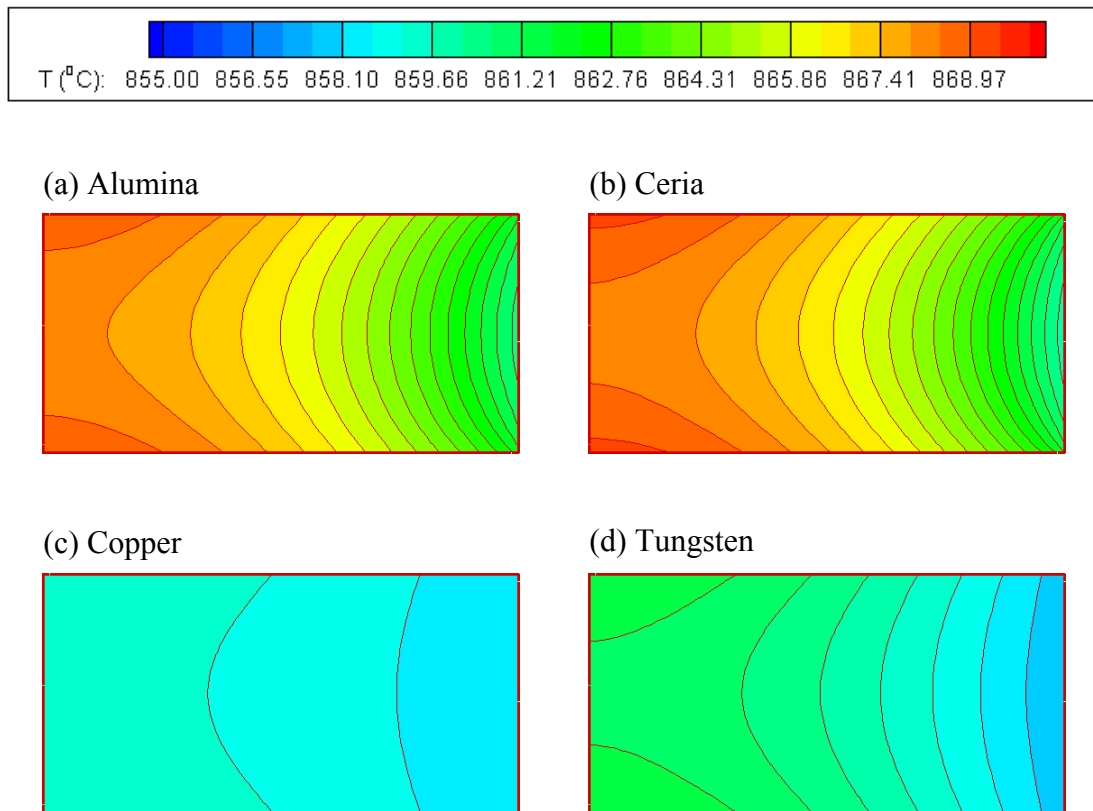


Figure 2-17. Comparison of the steady-state temperature distributions in the samples with the same aspect ratio of 0.5 for: (a) Alumina, (b) Ceria, (c) Copper, and (d) Tungsten.

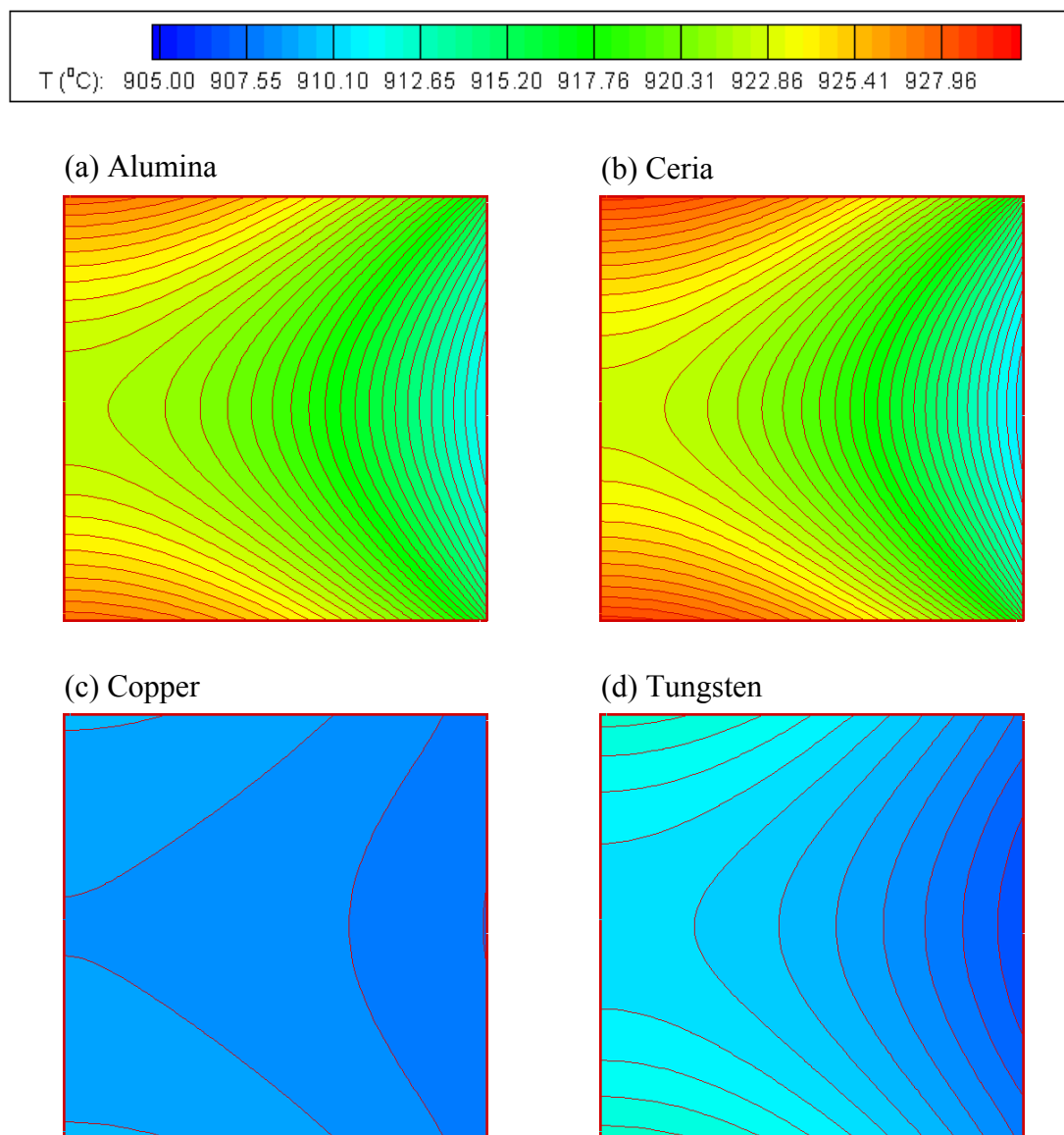


Figure 2-18. Comparison of the steady-state temperature distributions in the samples with the same aspect ratio of 1.0 for: (a) Alumina, (b) Ceria, (c) Copper, and (d) Tungsten.

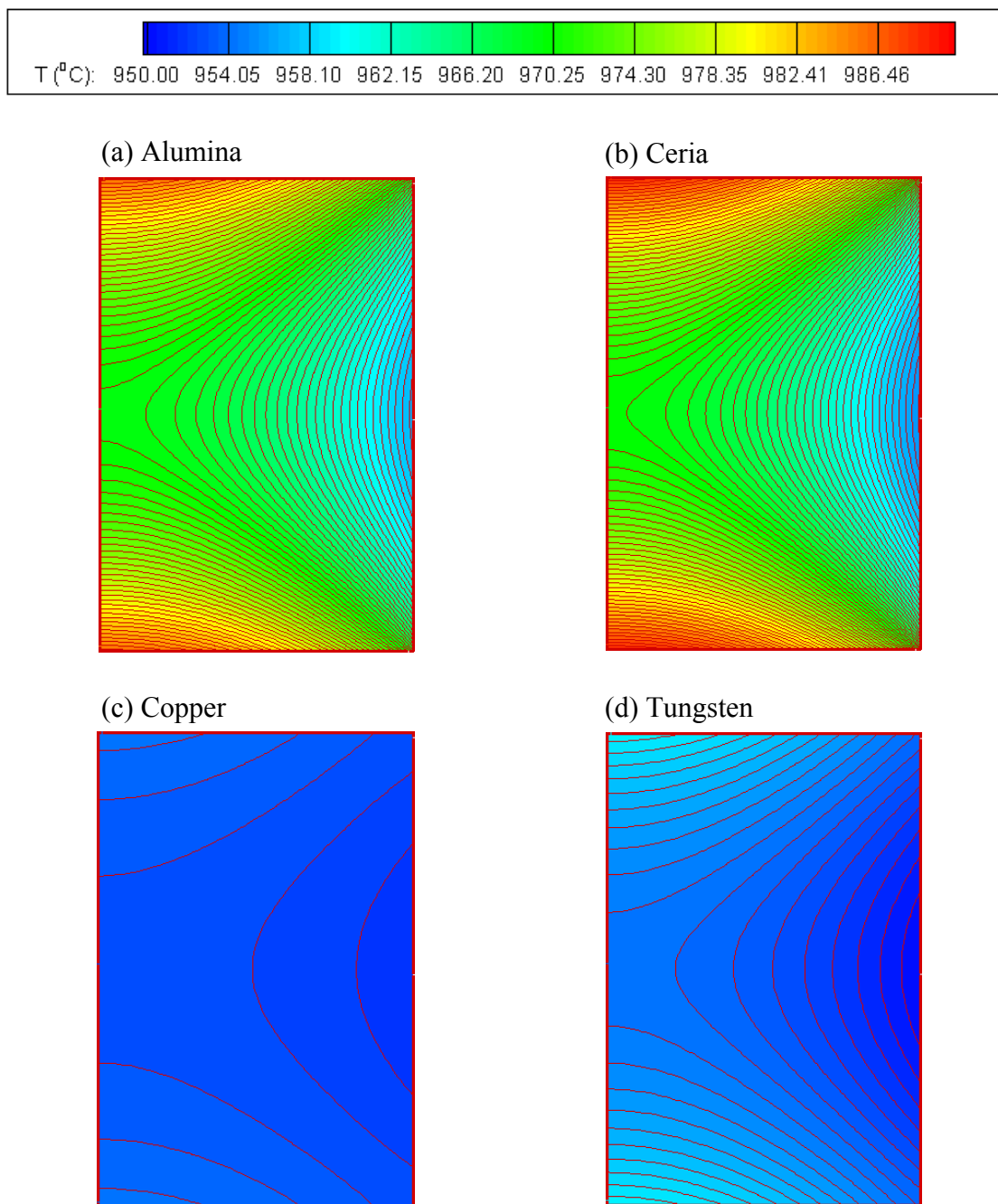


Figure 2-19. Comparison of the steady-state temperature distributions in the samples with the same aspect ratio of 1.5 for: (a) Alumina, (b) Ceria, (c) Copper, and (d) Tungsten.

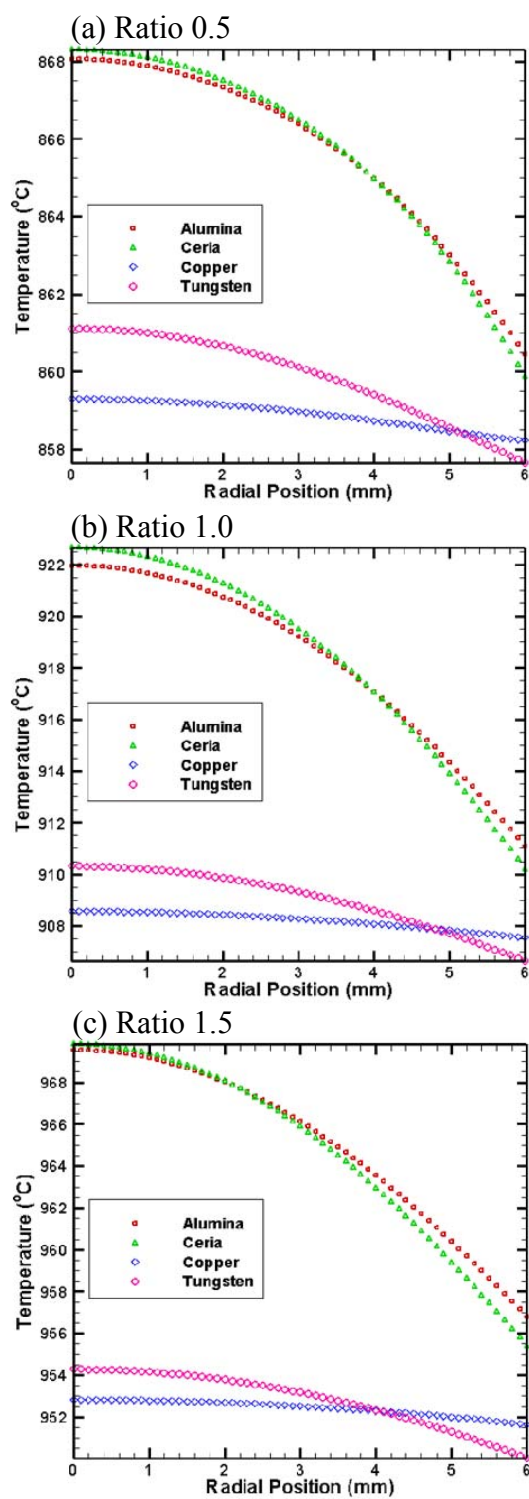


Figure 2-20. Comparison of the steady-state radial temperature profiles in the middle cross-section of the sample with the same aspect ratios: (a) Ratio 0.5, (b) Ratio 1.0, and (c) Ratio 1.5.

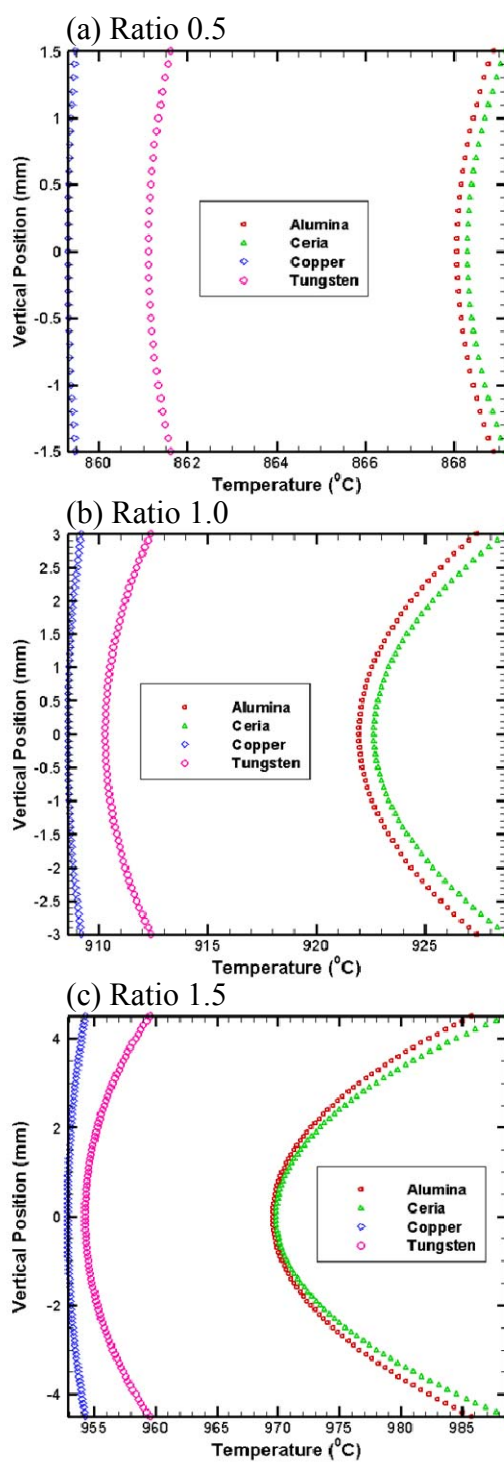


Figure 2-21. Comparison of the steady-state vertical temperature profiles along the axis of symmetry in the sample with the same aspect ratios: (a) Ratio 0.5, (b) Ratio 1.0, and (c) Ratio 1.5.

## 2.4 Conclusions

The thermal-electric portion of the three-way coupling of thermal, electrical, and mechanical model was developed in this chapter. Based on the model, influences of material properties and aspect ratios of the samples on the steady-state temperature distribution were then investigated.

It was found that the highest temperatures in the SPS system are always developed in the portion of punch which is enclosed by the graphite die, despite the changing of the sample aspect ratios. Additionally, the temperature and corresponding gradients are directly proportional to the aspect ratio of the sample. With the increment of the aspect ratio, the temperature gradients in the sample region become more severe, especially in the vertical direction.

The simulation results also showed that the thermal and electrical properties of the sample have an important influence on the temperature distribution in the SPS system, particularly in the sample region. Relatively low temperatures were obtained for the modeling cases with electrically conductive samples, due to heat transfer from the system to compensate for radiation losses. However, much higher temperature gradients were observed in the electrically non-conductive samples because of their comparatively low thermal conductivities.

## **Chapter 3**

### **Coupled Thermal-Mechanical Field Analysis**

#### **3.1 Introduction**

Based on the results obtained in Chapter 2, the thermal-mechanical portion of the three-way thermal, electrical and mechanical coupling model is introduced in this chapter. The load transfer method, which applies the temperature results from the thermal-electric field analysis as loads into the mechanical analysis, is used to decouple the thermal and mechanical fields. Comparisons between the samples with different material properties and aspect ratios are made, and the influences of material properties and aspect ratios on the stress distributions are also investigated.

#### **3.2 Finite Element Modeling Details**

##### **3.2.1 Theory**

In the current coupled thermal-mechanical field analysis, the mechanical motion of the whole system was assumed to be quasi-static, and only undergo linear elastic deformation. Since load transfer method was used, the stress field was computed for each instantaneous temperature distribution in an isotropic material according to the following governing equation:

$$\nabla \cdot \boldsymbol{\sigma} + \vec{X} = 0 \quad (3-1)$$

where  $\boldsymbol{\sigma}$  is the stress tensor and  $\vec{X}$  is the body force per unit volume. Based on the linear elastic assumption, the components of the stress tensor are defined by:

$$\sigma_{ij} = \lambda \varepsilon_{kk} \delta_{ij} + 2\mu \varepsilon_{ij} - \beta \delta_{ij} (T - T_0) \quad (3-2a)$$

$$\lambda = \frac{\nu E}{(1+\nu)(1-2\nu)} \quad (3-2b)$$

$$\mu = \frac{E}{2(1+\nu)} \quad (3-2c)$$

$$\beta = \frac{\alpha E}{1-2\nu} \quad (3-2d)$$

where  $E$  is the Young's modulus,  $\nu$  is the Poisson's ratio,  $\varepsilon_{ij}$  are the components of the strain tensor,  $\delta_{ij}$  is the Kronecker delta,  $\alpha$  is the linear coefficient of thermal expansion,  $T$  is the instantaneous temperature, and  $T_0$  is still the reference temperature.

### 3.2.2 Numerical Implementation

According to the load transfer method, the decoupled thermal and mechanical analyses are based on the same finite element mesh. Thus, the finite element meshes used in Chapter 2 were adopted in this analysis. However, the thermal-electric coupling elements were changed into structural elements. Samples made from different materials, including alumina, ceria, copper, and tungsten with different aspect ratios were considered in the simulation.

In the experiments conducted by the other participating institutes, a constant load of 7.2 kN was applied to the top spacer; in the current simulations, the corresponding constant pressure of 0.39 MPa was applied directly to the top spacer with a diameter of 152.4 mm translating to a 63.7 MPa of nominal applied pressure on the sample. Zero axial displacements were assumed for the lower boundary and the middle point of the outer surface of the die. Since a high purity Grafoil was used at the ends of each punch and on the inner die wall to act as a lubricant between the sample, punches, and graphite die, “pure” slips without friction at the contact interfaces were assumed for all of the simulation. Additionally, the steady-state nodal temperature at 1000s from the thermal-electric analysis was used as load transferred to the new models for the stress analysis.

Based on the thermoelasticity assumptions, both displacements and stresses were generated by coupling the effects of the thermal expansion mismatch due to the temperature gradients as discussed in Chapter 2, and the Poisson-type expansion due to the uniaxial applied load on the top of spacer. Given these considerations, the radial, circumferential (hoop), and vertical (axial) stresses developed in the SPS system at 800 A DC current input and steady-state temperature were calculated, and the influences of material properties and aspect ratios of the samples on the stress distributions were also investigated.

### **3.3 Results and Discussion**

The distribution of stresses in the radial, hoop, and axial directions in the punch/sample/die assembly with the candidate materials with different aspect ratios are

shown in Figures 3-1 to 3-12, respectively. Local views of the stress distribution in different sample regions are plotted in Figures 3-13 to 3-24. The stress profiles in the middle cross-section and along the axis of symmetry in the punch/sample/die assembly are also displayed in Figures 3-25 to 3-30. In addition, Tables 3-1 to 3-3 list the minimum and maximum components of the stresses in the samples.

As revealed in Figures 3-1 to 3-4, compressive radial stresses are well distributed through nearly the entire punch/sample/die assembly. For the cases of alumina and tungsten samples (Figures 3-1 and 3-4), the maximum radial stress gradients appear in the regions where the punches come into contact with the spacers, and the radial stress changes from compressive in the spacers to tensile in the punches. However, the maximum radial stress gradients occur at the region across the sample-die interfaces for both the cases of ceria and copper samples (Figures 3-2 and 3-3). A local view of the sample also shows that there are larger differences of the radial stress distribution among the various materials. In the cases of alumina and tungsten (Figures 3-13 and 3-16), the radial stress distributions are uniform, while inhomogeneous compressive radial stress with extremely higher magnitudes dominates the sample regions of ceria and copper (Figures 3-14 and 3-15). These stress states are linked to the fact that the ceria and copper exhibit higher coefficients of thermal expansion compared with alumina and tungsten. With increments of temperature, the samples expand and push the die wall, causing deformation and relatively high radial stress in both the sample and die in the contact regions. The higher the temperature, the greater the radial compressive stress within the samples and the die. In addition, Figures 3-13 to 3-16 indicate that the radial stress distributions are comparatively uniform for the samples with smaller aspect ratios, even

though the magnitudes of the stresses are different. The lower the aspect ratio, the smaller the temperature gradient and subsequently, the more uniform the radial stress distribution.

Figures 3-5 to 3-8 show the contour plots of the distributions of the hoop stress in the punch/sample/die assembly. Similar to the radial distributions, the maximum stress gradients appear at the punch-spacer interfaces for the alumina and tungsten sample cases (Figures 3-5 and 3-8), while at the sample-die interfaces for the ceria and copper (Figures 3-6 and 3-7). Due to the higher values of the coefficient of thermal expansion, the ceria and copper samples are also subjected to extremely high compressive hoop stresses. Even though the punch-die region is dominated by compressive stress, tensile stresses appear in the die area as the expansion of the samples, especially when the sample comes into contact with die. Local views (Figures 3-17 and 3-20) also show that the material properties and aspect ratios exert the same influences on the hoop stress distributions as seen in the radial direction.

According to the contour plots of the axial stress distributions (Figures 3-9 to 3-12), compression still prevails in the sample and the punches, with the magnitude of the stress largely dependents on the externally applied load. In contrast to the radial and hoop ones, the severe axial stress gradients for the all the cases with different material properties and aspect ratios appear in the regions of the punches where the temperature is the highest. Moreover, high stress gradients also show up at the region across the sample-die interfaces for both ceria and copper. In addition, the axial stresses in the graphite die are almost zero for the alumina and tungsten cases. However, high magnitude compressive stresses are developed in the die for ceria and copper, due to the expansion

of the samples. Once again, as shown in Figures 3-21 to 3-24, the axial stress gradients in the sample region are much smaller than that of the radial and hoop components. The axial stresses are more uniform across the alumina and tungsten samples, and lower gradients appear in the sample with smaller aspect ratios.

Steady-state shear stresses in the system were also calculated, even though the contour plots are not explicitly shown in this thesis. For the alumina and tungsten cases, nonzero shear stress shows up mainly at the corners of the punch-spacer and punch-die interfaces. The situation at the punch-spacer and punch-die corners is similar for the ceria and copper cases, however, shear stress is also observed at the corners of sample-die interface.

Considering the stress profiles in the middle cross-section and along the axis of symmetry in the punch/sample/die assembly as shown in Figures 3-25 to 3-30, the shear stress is always zero. More uniform distributions of all stresses correspond to the alumina and tungsten cases with smaller aspect ratios. However, the stress gradients are still much higher than temperature ones. As ceria and copper exhibit much higher coefficients of thermal expansion than that of the graphite die, extremely high radial and hoop stresses are developed in the sample region and at the sample-die interface. It should be noted that plasticity is not considered in the current study, even when high stresses were observed. Hence, the actual stress states may be somewhat different if the yield stress is exceeded as may be the case for relatively low yield threshold materials such as copper.

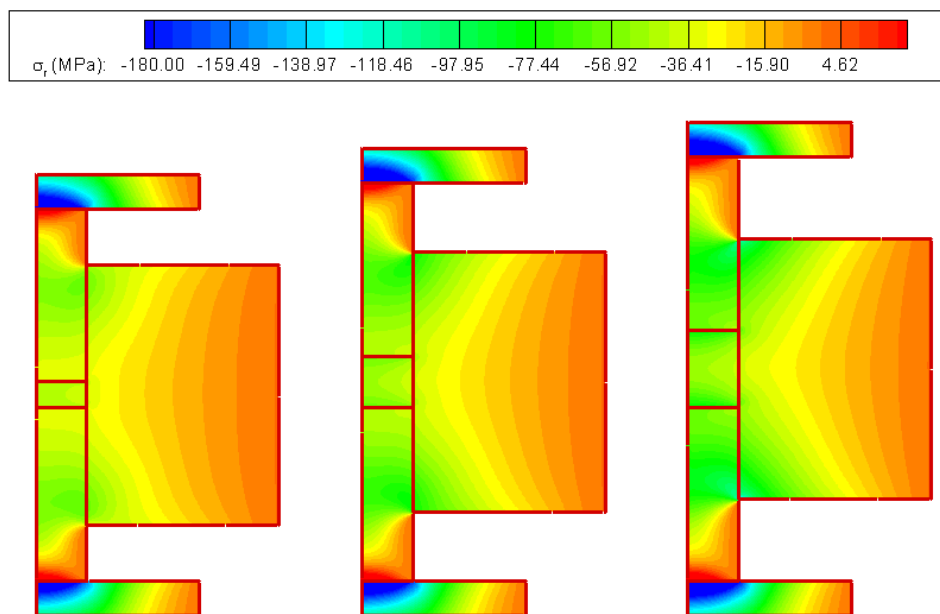


Figure 3-1. Contour plots of the radial stress distribution in the punch/sample/die area of alumina samples with different aspect ratios: 0.5 (left), 1.0 (middle), and 1.5 (right).

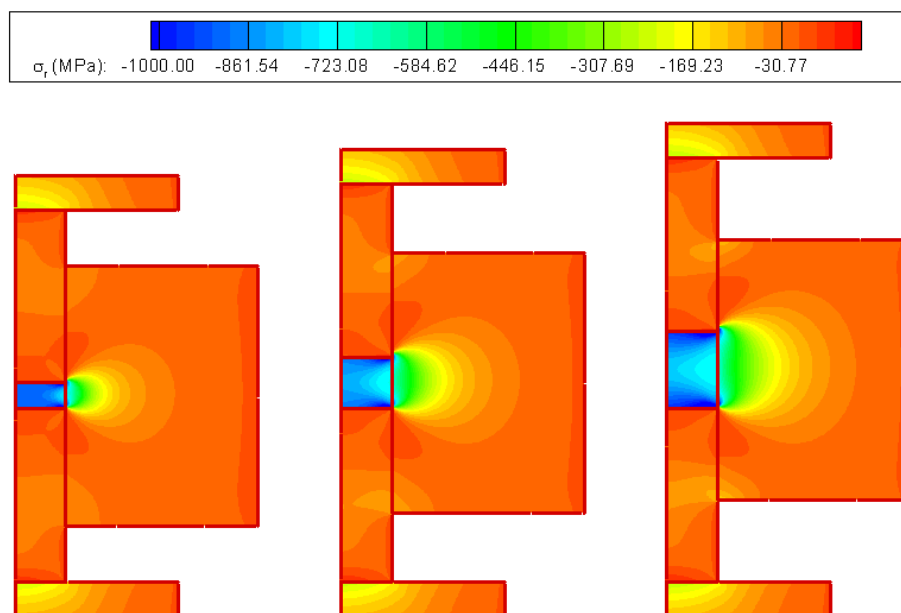


Figure 3-2. Contour plots of the radial stress distribution in the punch/sample/die area of ceria samples with different aspect ratios: 0.5 (left), 1.0 (middle), and 1.5 (right).

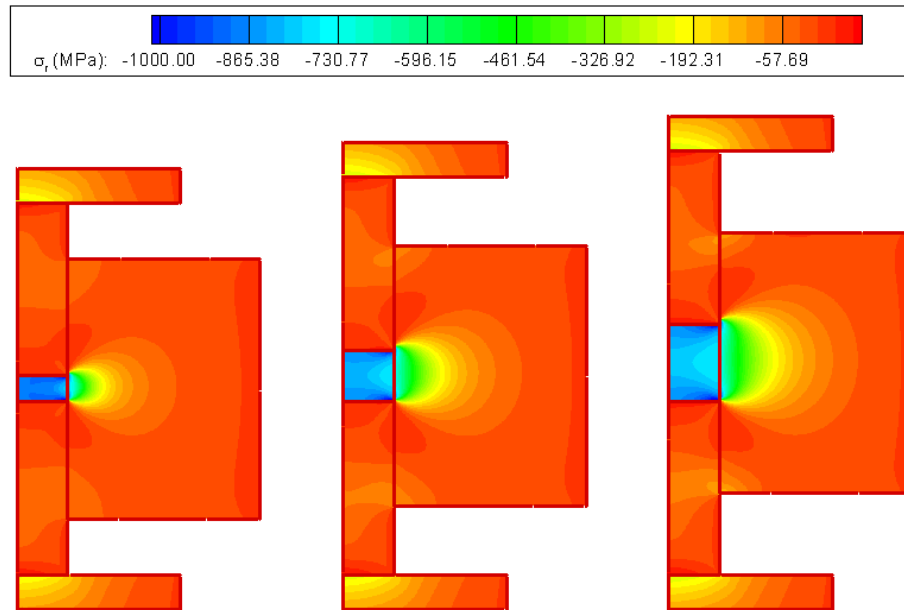


Figure 3-3. Contour plots of the radial stress distribution in the punch/sample/die area of copper samples with different aspect ratios: 0.5 (left), 1.0 (middle), and 1.5 (right).

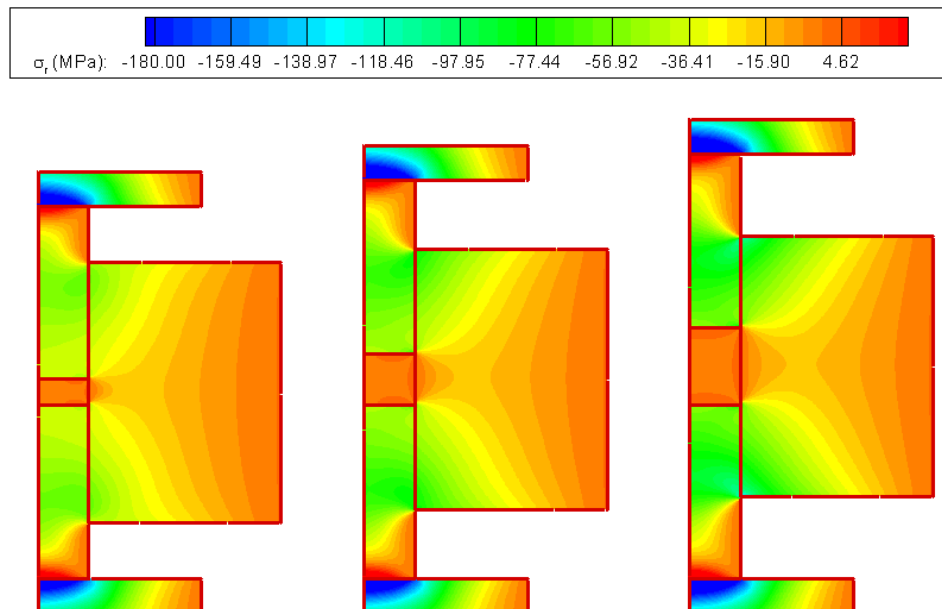


Figure 3-4. Contour plots of the radial stress distribution in the punch/sample/die area of tungsten samples with different aspect ratios: 0.5 (left), 1.0 (middle), and 1.5 (right).

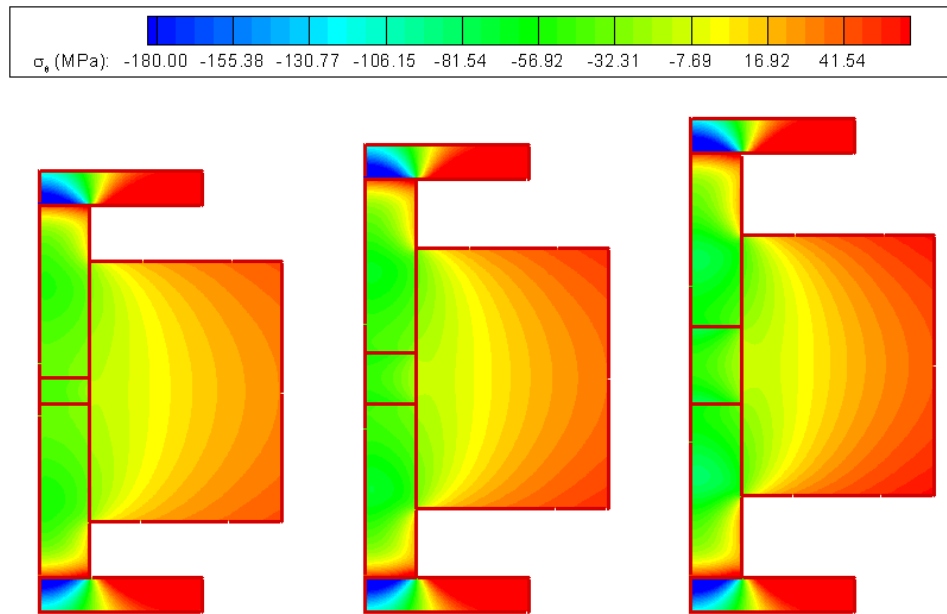


Figure 3-5. Contour plots of the hoop stress distribution in the punch/sample/die area of alumina samples with different aspect ratios: 0.5 (left), 1.0 (middle), and 1.5 (right).

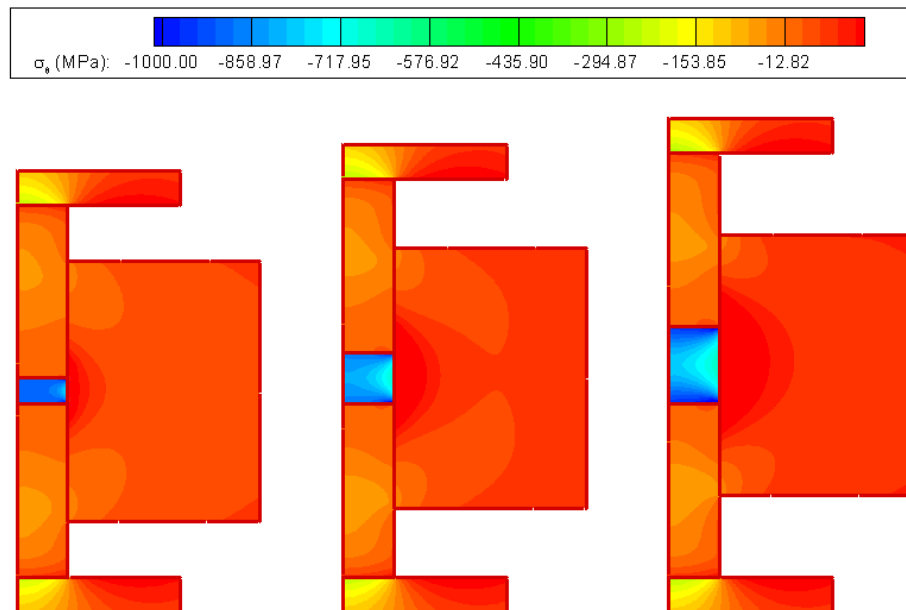


Figure 3-6. Contour plots of the hoop stress distribution in the punch/sample/die area of ceria samples with different aspect ratios: 0.5 (left), 1.0 (middle), and 1.5 (right).

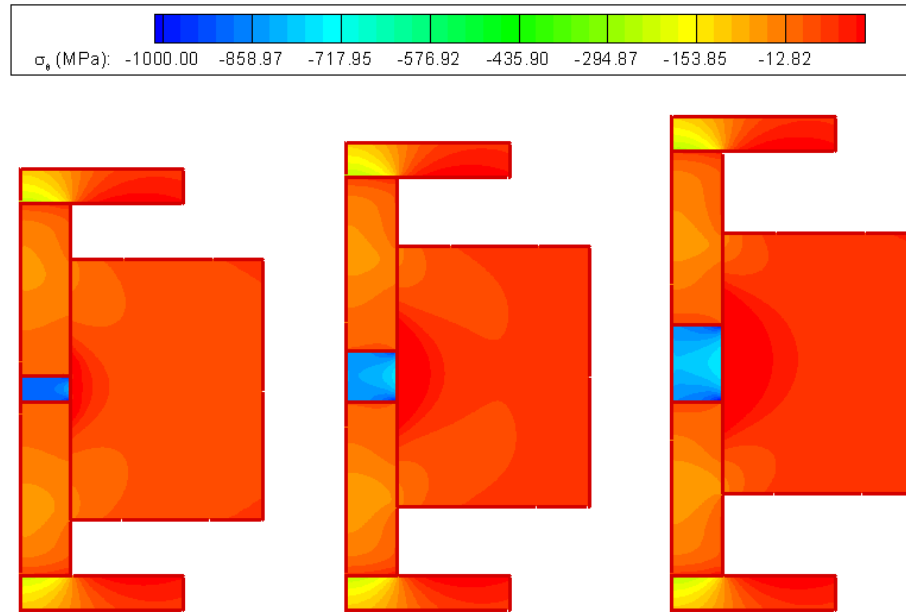


Figure 3-7. Contour plots of the hoop stress distribution in the punch/sample/die area of copper samples with different aspect ratios: 0.5 (left), 1.0 (middle), and 1.5 (right).

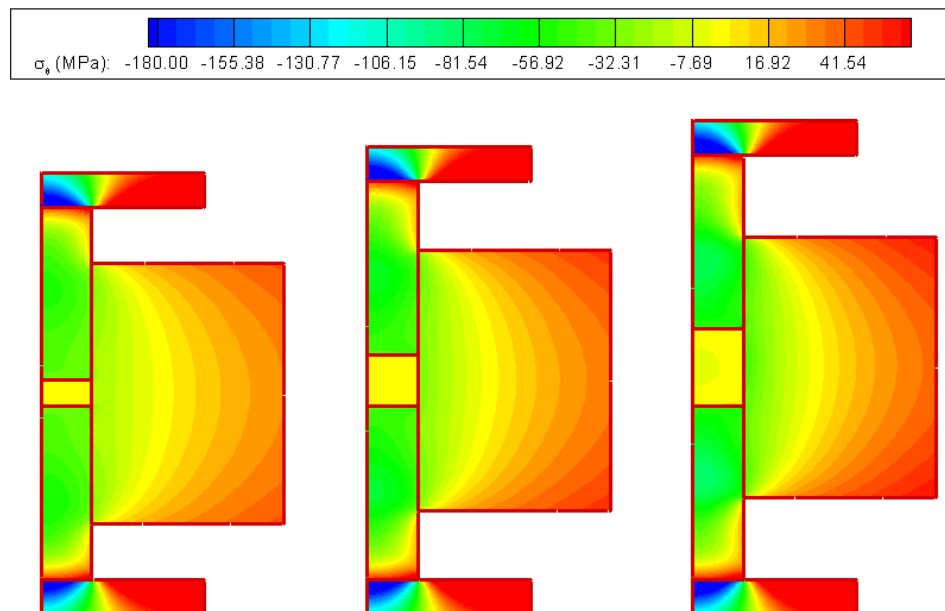


Figure 3-8. Contour plots of the hoop stress distribution in the punch/sample/die area of tungsten samples with different aspect ratios: 0.5 (left), 1.0 (middle), and 1.5 (right).

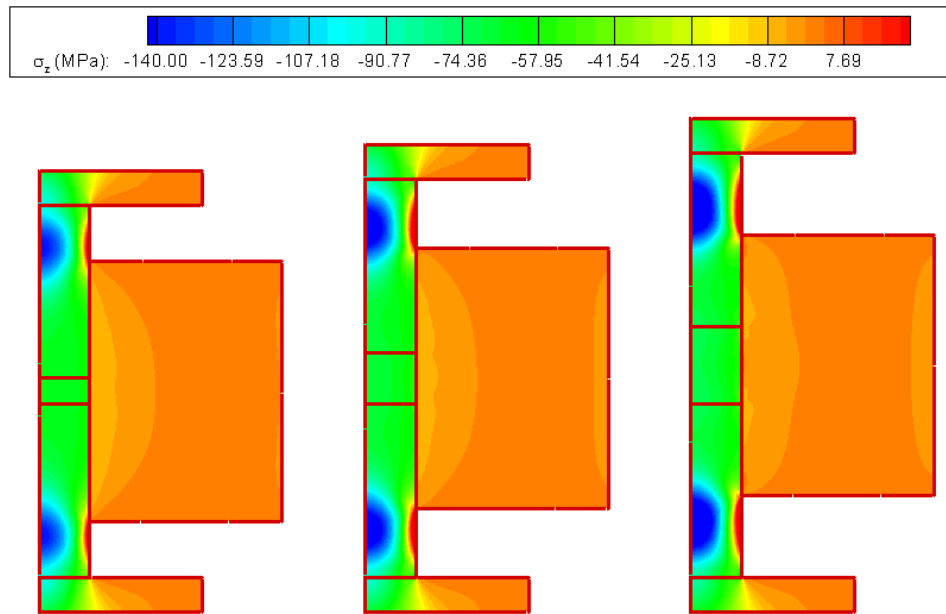


Figure 3-9. Contour plots of the axial stress distribution in the punch/sample/die area of alumina samples with different aspect ratios: 0.5 (left), 1.0 (middle), and 1.5 (right).

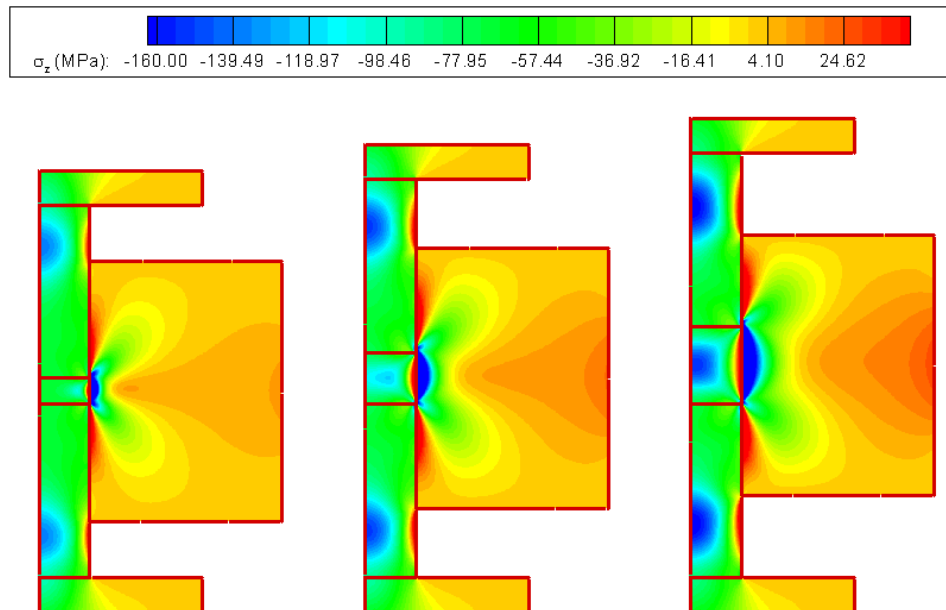


Figure 3-10. Contour plots of the axial stress distribution in the punch/sample/die area of ceria samples with different aspect ratios: 0.5 (left), 1.0 (middle), and 1.5 (right).

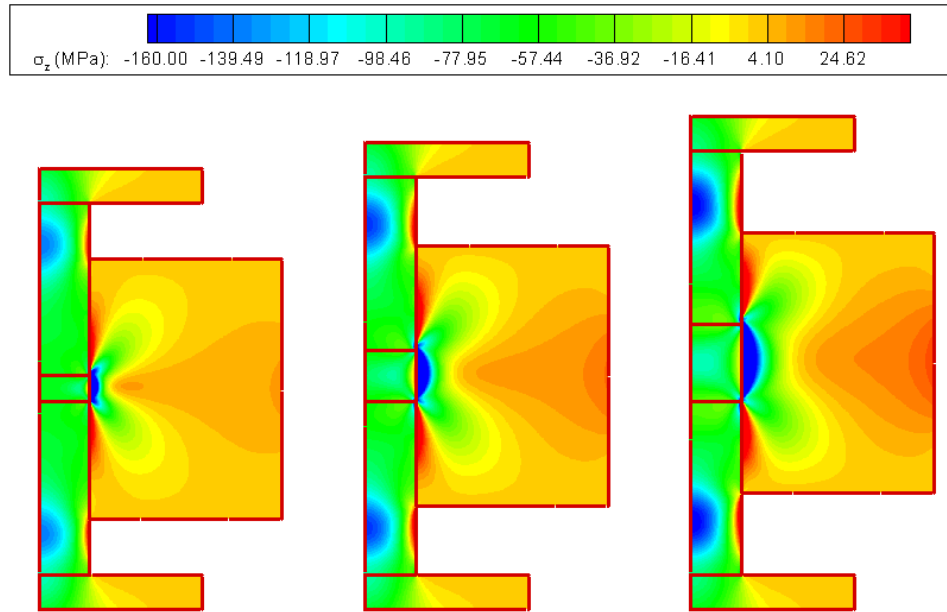


Figure 3-11. Contour plots of the axial stress distribution in the punch/sample/die area of copper samples with different aspect ratios: 0.5 (left), 1.0 (middle), and 1.5 (right).

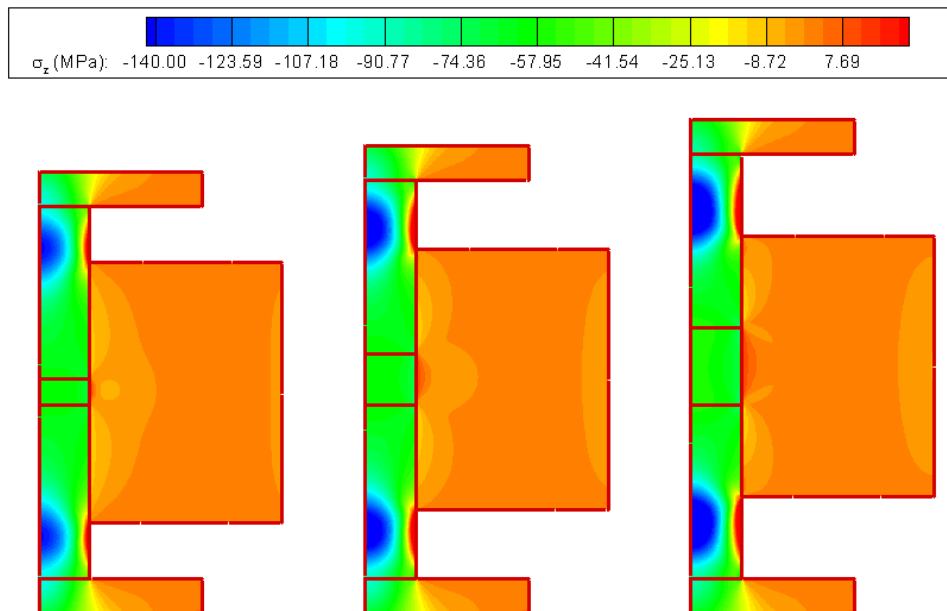


Figure 3-12. Contour plots of the axial stress distribution in the punch/sample/die area of tungsten samples with different aspect ratios: 0.5 (left), 1.0 (middle), and 1.5 (right).

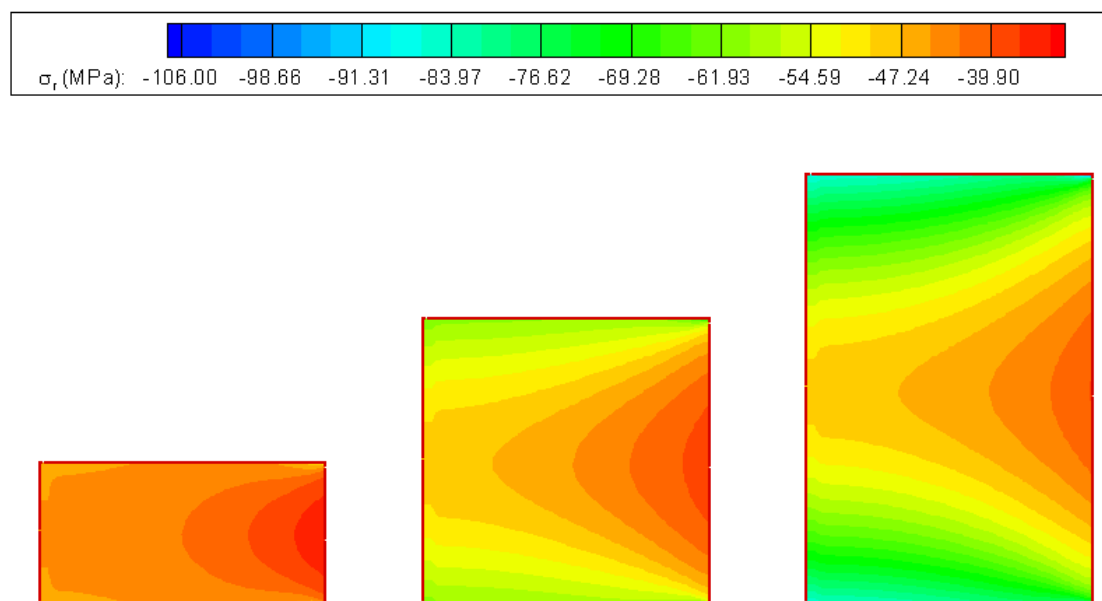


Figure 3-13. Contour plots of the radial stress distribution in the region of alumina samples with different aspect ratios: 0.5 (left), 1.0 (middle), and 1.5 (right).

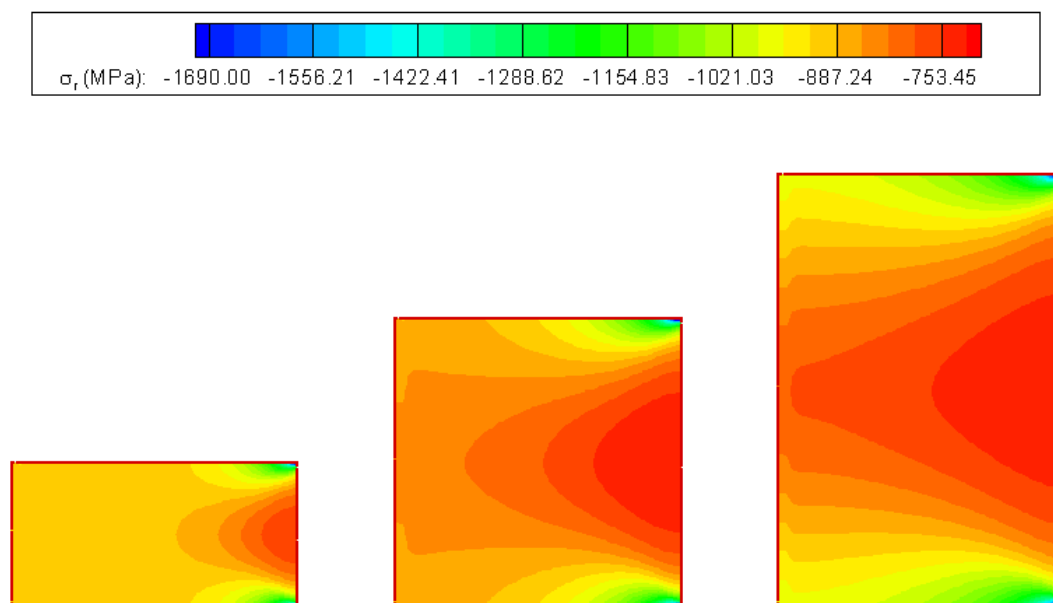


Figure 3-14. Contour plots of the radial stress distribution in the region of ceria samples with different aspect ratios: 0.5 (left), 1.0 (middle), and 1.5 (right).

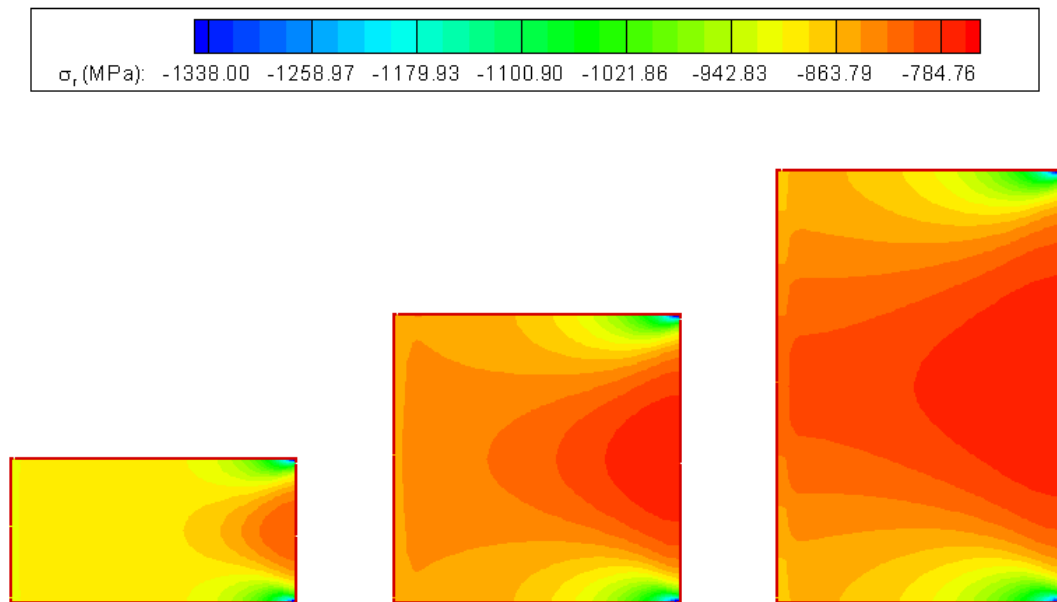


Figure 3-15. Contour plots of the radial stress distribution in the region of copper samples with different aspect ratios: 0.5 (left), 1.0 (middle), and 1.5 (right).

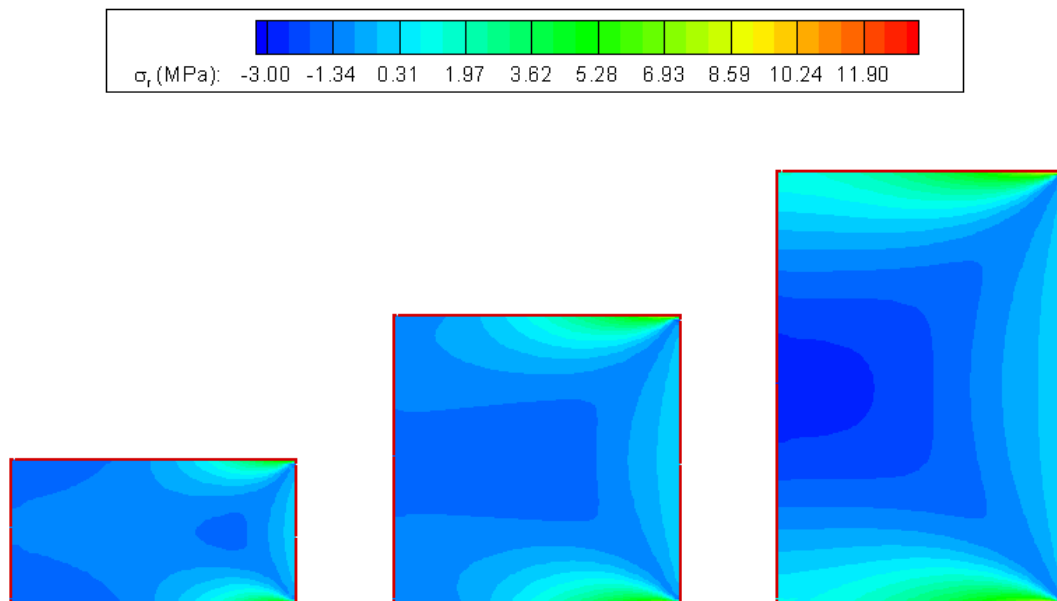


Figure 3-16. Contour plots of the radial stress distribution in the region of tungsten samples with different aspect ratios: 0.5 (left), 1.0 (middle), and 1.5 (right).

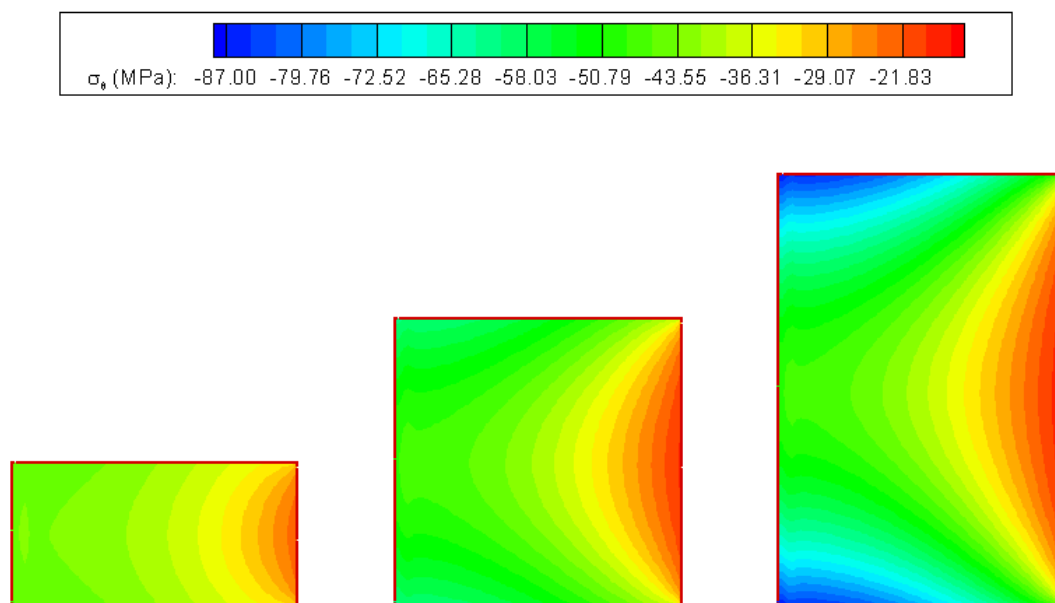


Figure 3-17. Contour plots of the hoop stress distribution in the region of alumina samples with different aspect ratios: 0.5 (left), 1.0 (middle), and 1.5 (right).

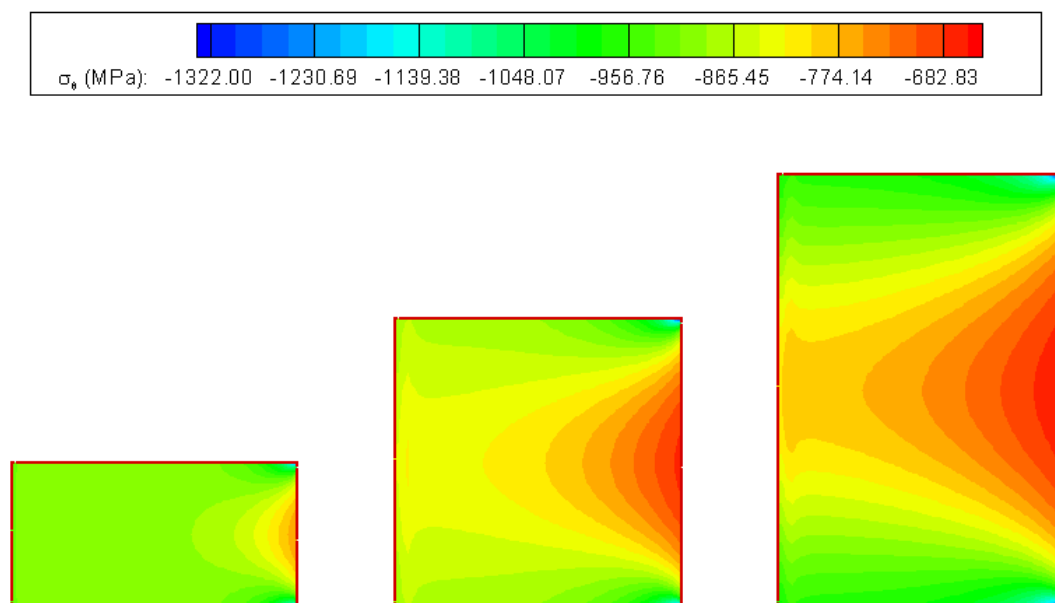


Figure 3-18. Contour plots of the hoop stress distribution in the region of ceria samples with different aspect ratios: 0.5 (left), 1.0 (middle), and 1.5 (right).

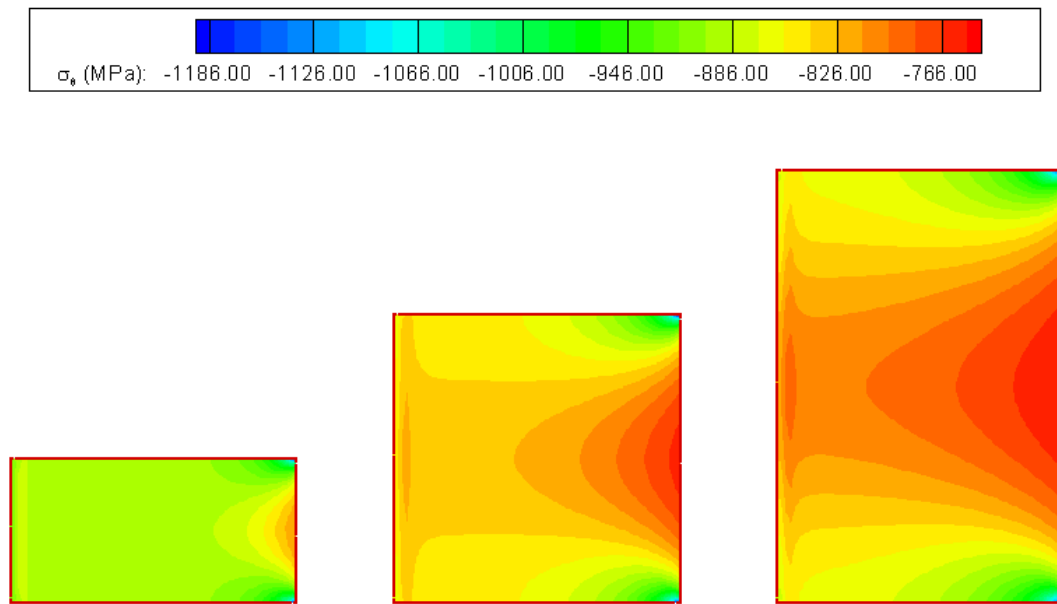


Figure 3-19. Contour plots of the hoop stress distribution in the region of copper samples with different aspect ratios: 0.5 (left), 1.0 (middle), and 1.5 (right).

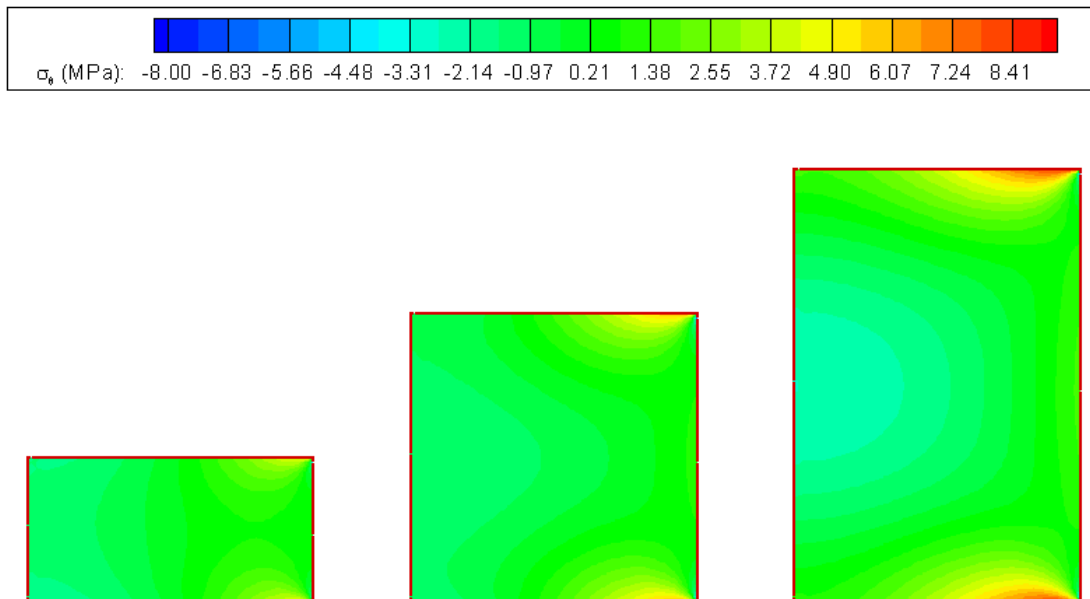


Figure 3-20. Contour plots of the hoop stress distribution in the region of tungsten samples with different aspect ratios: 0.5 (left), 1.0 (middle), and 1.5 (right).

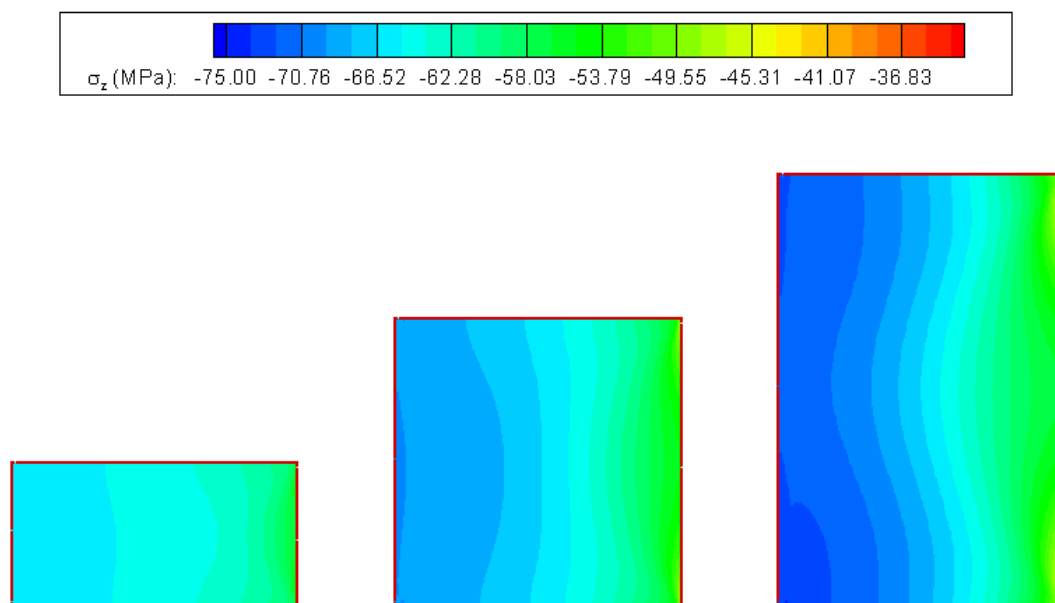


Figure 3-21. Contour plots of the axial stress distribution in the region of alumina samples with different aspect ratios: 0.5 (left), 1.0 (middle), and 1.5 (right).

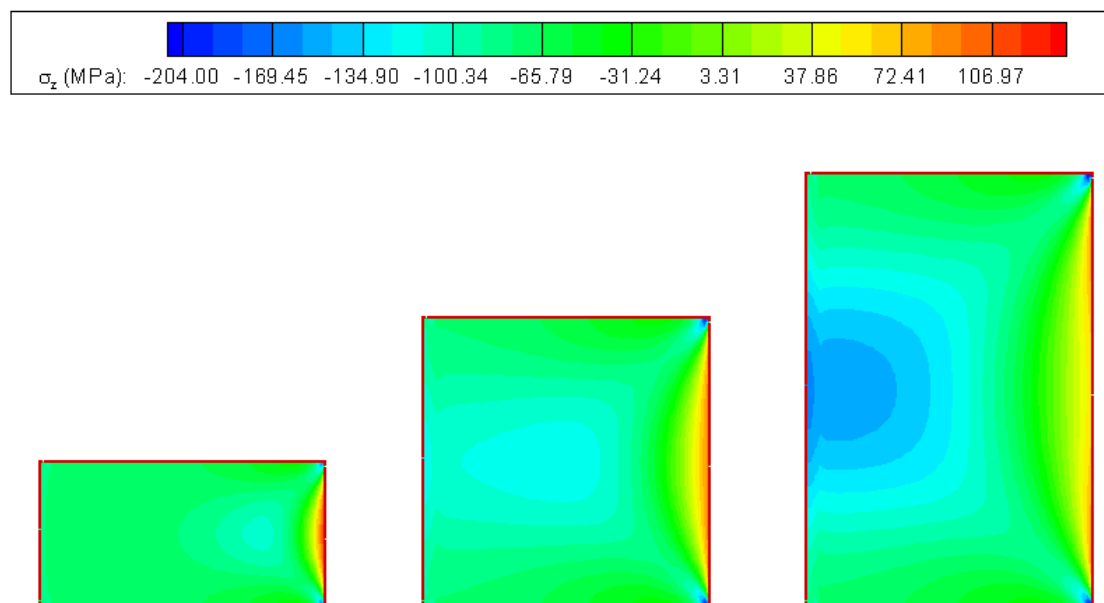


Figure 3-22. Contour plots of the axial stress distribution in the region of ceria samples with different aspect ratios: 0.5 (left), 1.0 (middle), and 1.5 (right).

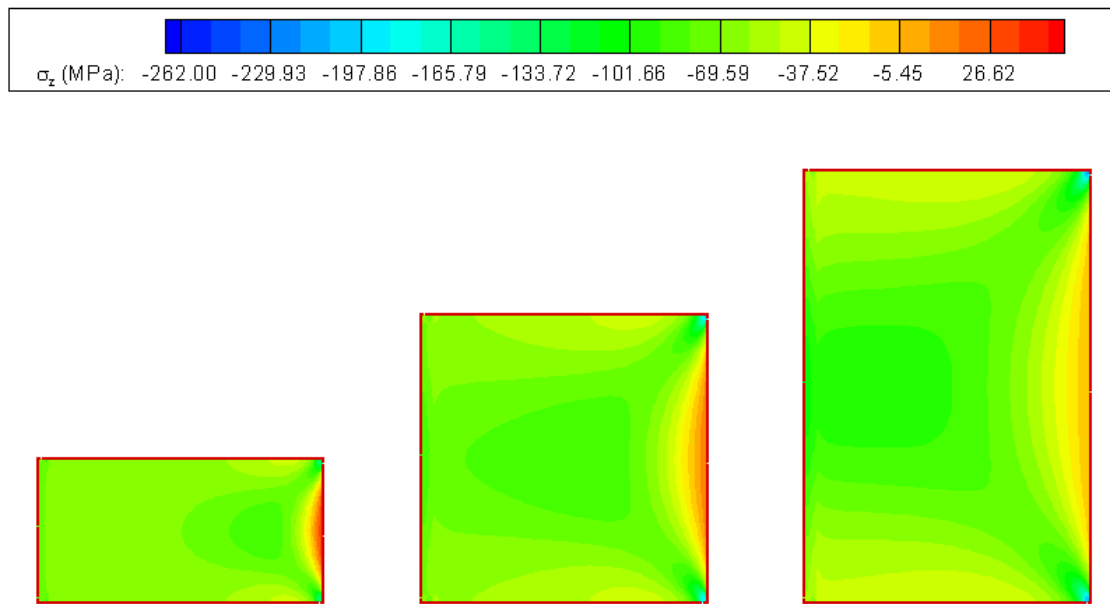


Figure 3-23. Contour plots of the axial stress distribution in the region of copper samples with different aspect ratios: 0.5 (left), 1.0 (middle), and 1.5 (right).

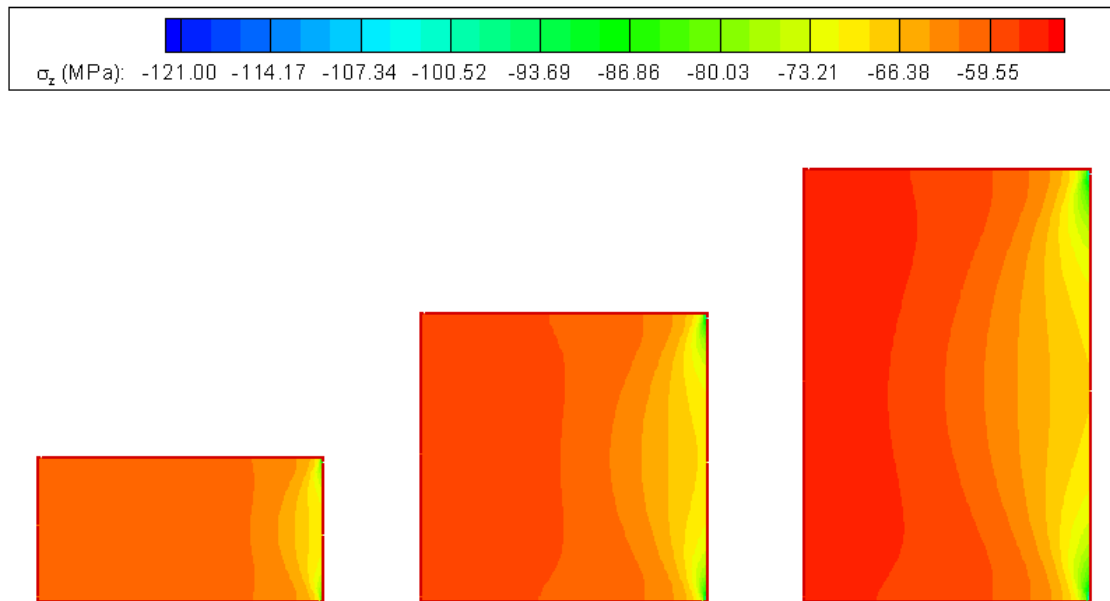


Figure 3-24. Contour plots of the axial stress distribution in the region of tungsten samples with different aspect ratios: 0.5 (left), 1.0 (middle), and 1.5 (right).

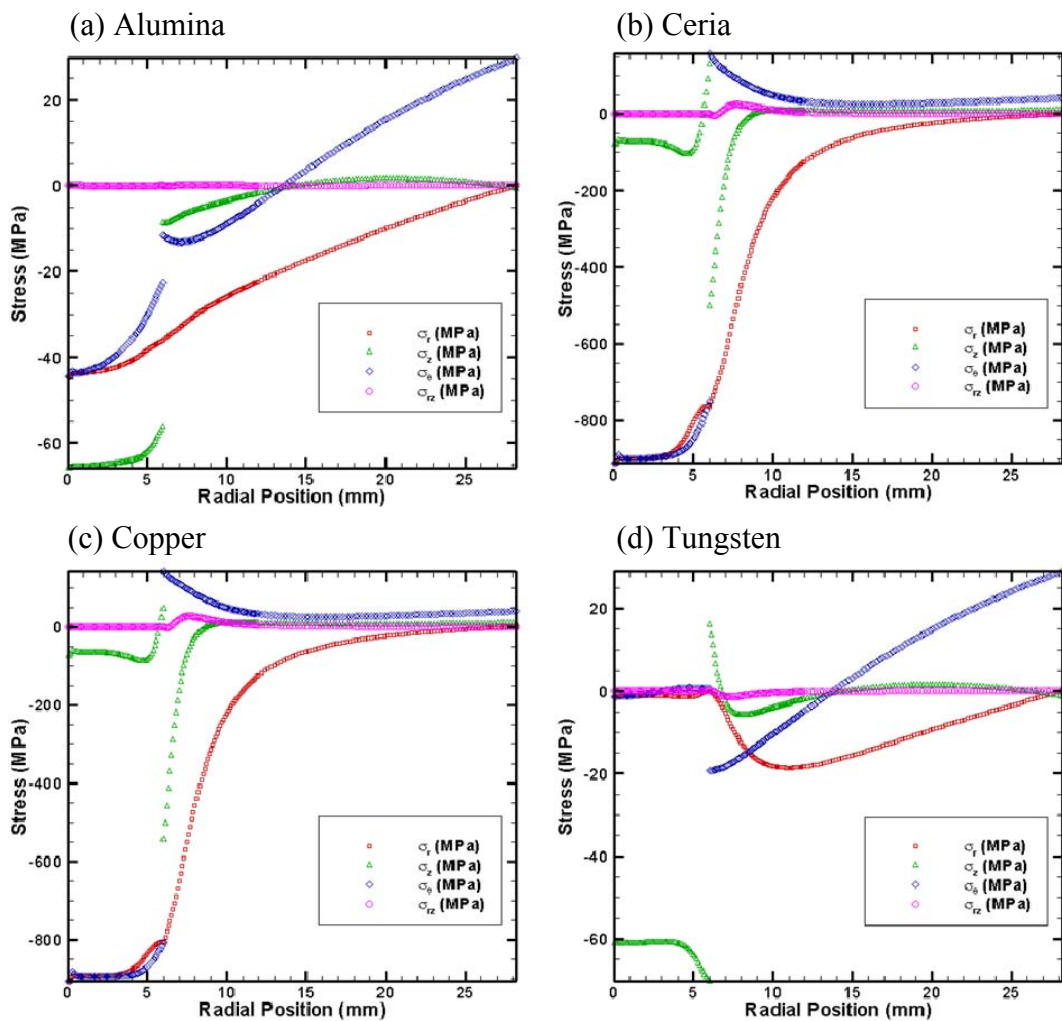


Figure 3-25. Comparison of the stress profiles in the middle cross-section of the sample and the die with the same sample aspect ratio of 0.5 for: (a) Alumina, (b) Ceria, (c) Copper, and (d) Tungsten.

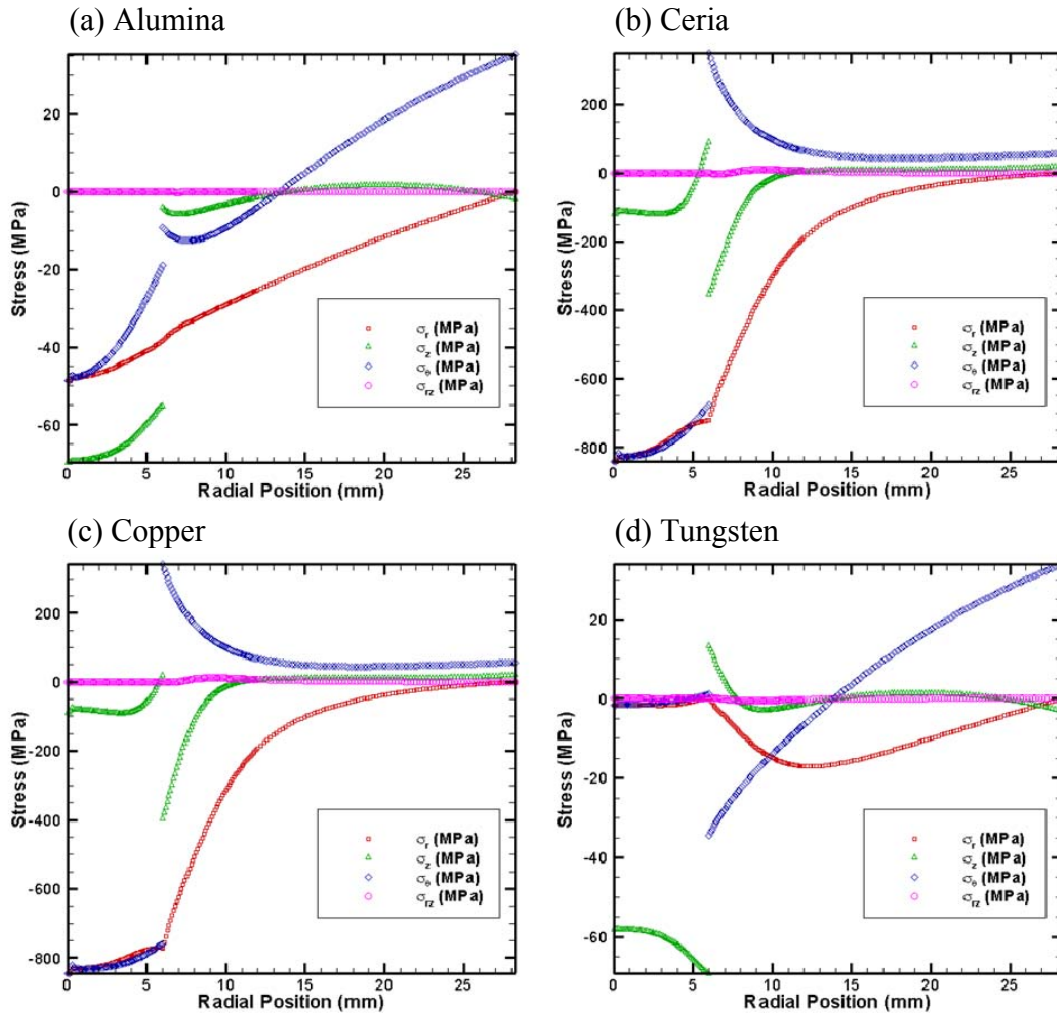


Figure 3-26. Comparison of the stress profiles in the middle cross-section of the sample and the die with the same sample aspect ratio of 1.0 for: (a) Alumina, (b) Ceria, (c) Copper, and (d) Tungsten.

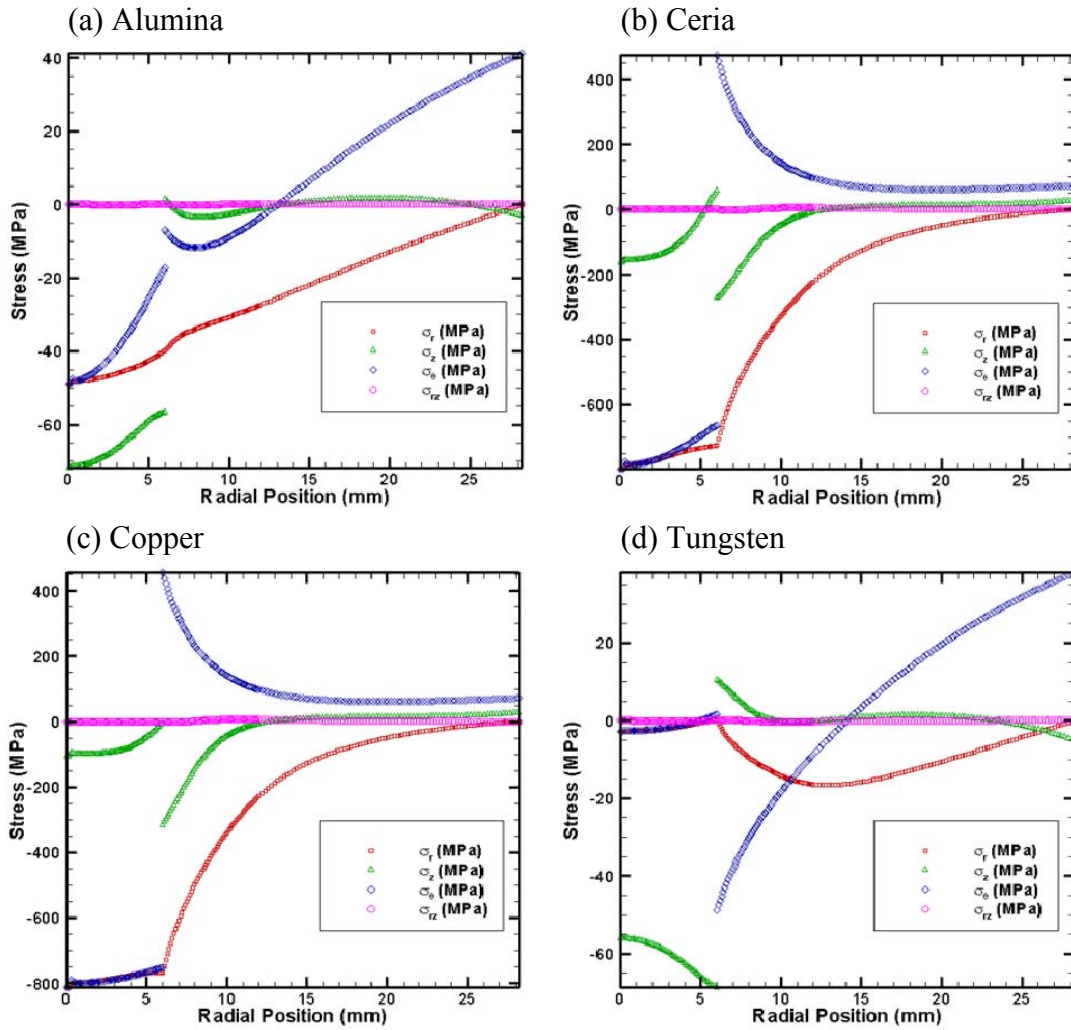


Figure 3-27. Comparison of the stress profiles in the middle cross-section of the sample and the die with the same sample aspect ratio of 1.5 for: (a) Alumina, (b) Ceria, (c) Copper, and (d) Tungsten.

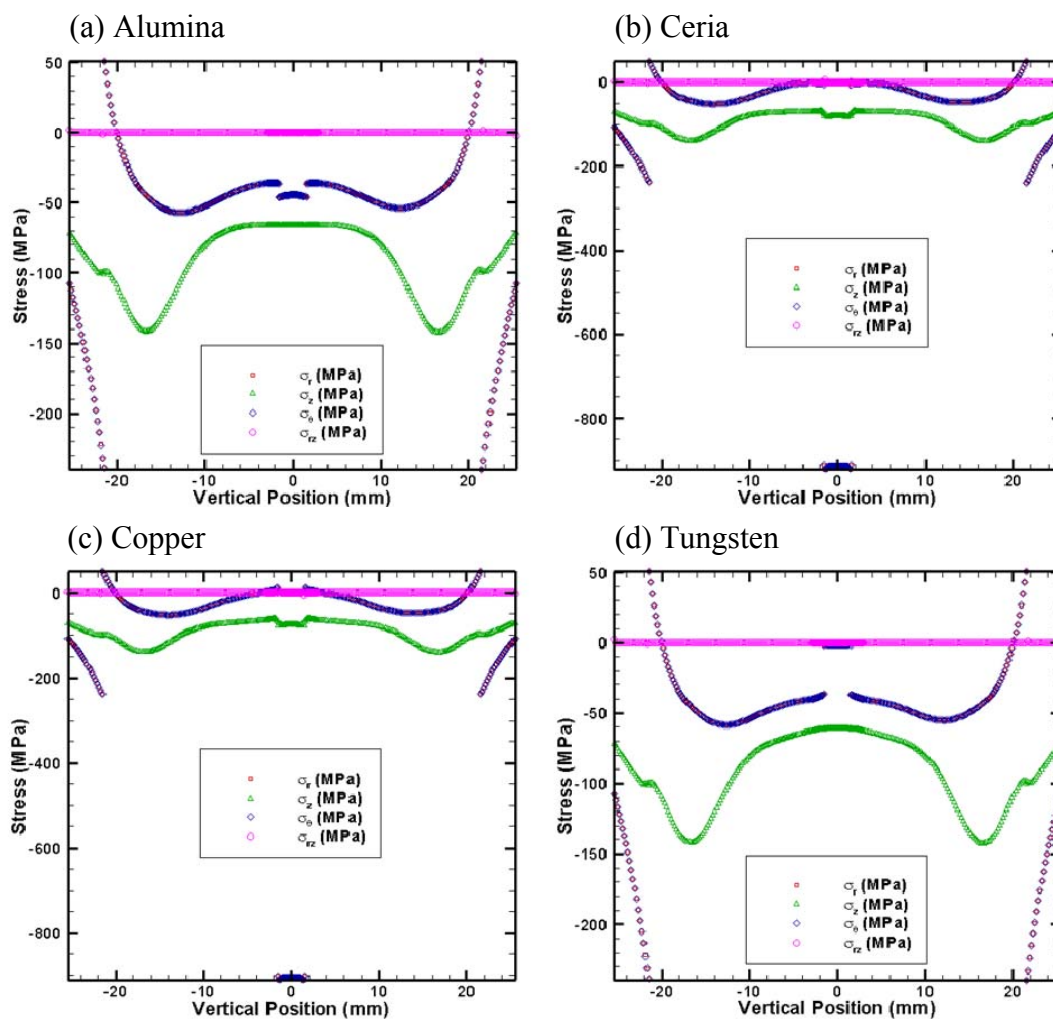


Figure 3-28. Comparison of the stress profiles along the axis of symmetry in the punch/sample/die assembly with the same sample aspect ratio of 0.5 for: (a) Alumina, (b) Ceria, (c) Copper, and (d) Tungsten.

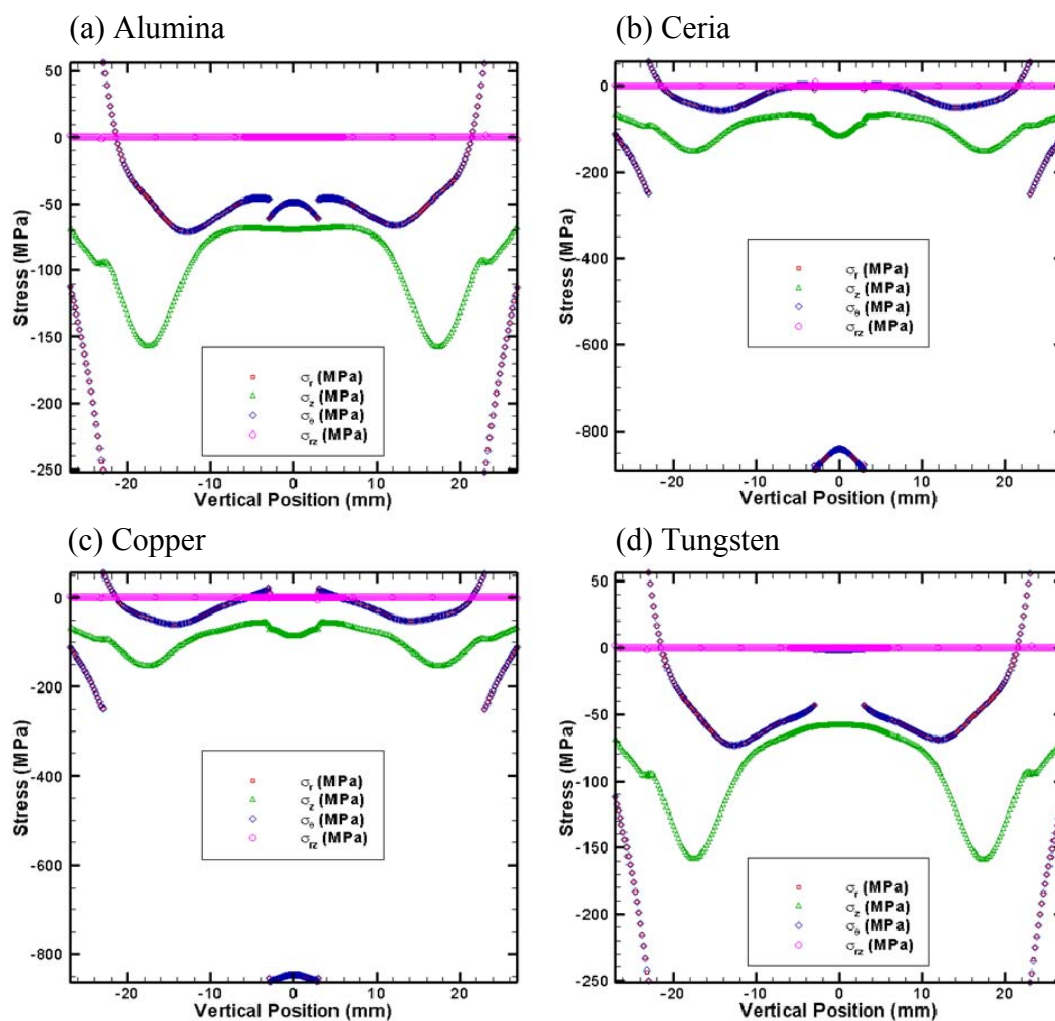


Figure 3-29. Comparison of the stress profiles along the axis of symmetry in the punch/sample/die assembly with the same sample aspect ratio of 1.0 for: (a) Alumina, (b) Ceria, (c) Copper, and (d) Tungsten.

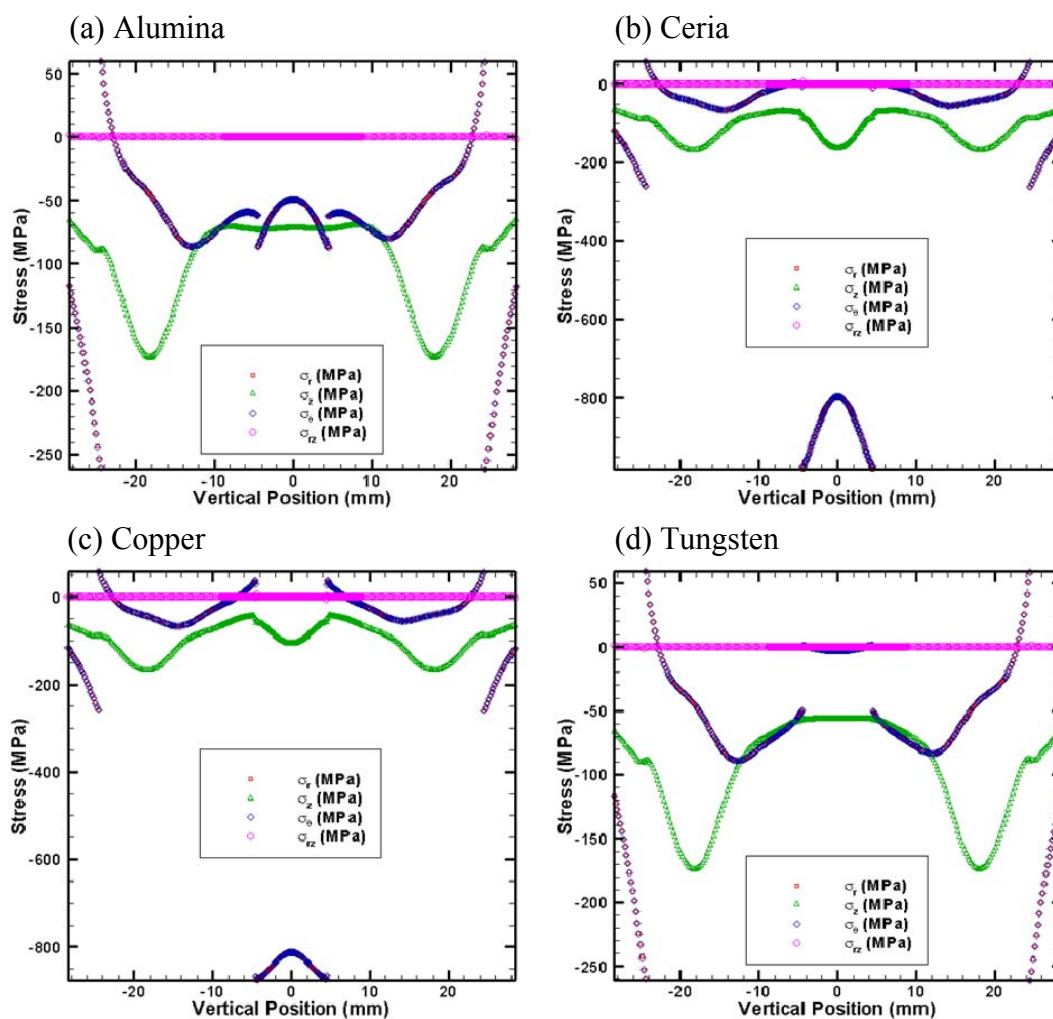


Figure 3-30. Comparison of the stress profiles along the axis of symmetry in the punch/sample/die assembly with the same sample aspect ratio of 1.5 for: (a) Alumina, (b) Ceria, (c) Copper, and (d) Tungsten.

Table 3-1. Minimum and maximum radial stress in the sample region (MPa).

Ratio	0.5		1.0		1.5	
Sample	$\sigma_{r, \min}$	$\sigma_{r, \max}$	$\sigma_{r, \min}$	$\sigma_{r, \max}$	$\sigma_{r, \min}$	$\sigma_{r, \max}$
Alumina	-57.23	-36.08	-74.55	-38.35	-105.55	-39.67
Ceria	-1453.79	-760.48	-1569.66	-720.58	-1689.52	-723.77
Copper	-1281.55	-804.96	-1295.17	-769.24	-1337.59	-765.68
Tungsten	-1.96	8.97	-1.83	10.76	-2.73	12.52

Table 3-2. Minimum and maximum hoop stress in the sample region (MPa).

Ratio	0.5		1.0		1.5	
Sample	$\sigma_{\theta, \min}$	$\sigma_{\theta, \max}$	$\sigma_{\theta, \min}$	$\sigma_{\theta, \max}$	$\sigma_{\theta, \min}$	$\sigma_{\theta, \max}$
Alumina	-46.06	-22.51	-61.08	-18.95	-86.81	-17.17
Ceria	-1188.97	-748.40	-1225.19	-675.22	-1321.03	-661.47
Copper	-1087.97	-806.61	-1122.96	-759.10	-1185.48	-751.21
Tungsten	-5.34	5.12	-6.44	6.63	-7.19	8.51

Table 3-3. Minimum and maximum axial stress in the sample region (MPa).

Ratio	0.5		1.0		1.5	
Sample	$\sigma_{z, \min}$	$\sigma_{z, \max}$	$\sigma_{z, \min}$	$\sigma_{z, \max}$	$\sigma_{z, \min}$	$\sigma_{z, \max}$
Alumina	-66.57	-52.91	-70.16	-45.45	-74.72	-34.72
Ceria	-161.21	129.75	-190.75	93.6	-203.48	95.32
Copper	-192.41	47.69	-242.36	19.06	-261.7	-2.56
Tungsten	-100.54	-60.44	-110.48	-58.01	-120.89	-55.45

### 3.4 Conclusions

In this chapter, the thermal-mechanical portion of the three-way thermal, electrical, and mechanical coupling model was introduced. Accordingly, the investigation of the steady-state stress distributions within the SPS system at the final stage of the densification was conducted. Comparisons between the samples with different material properties and aspect ratios were then made, and the influences of material properties and aspect ratios on the stress distributions were also investigated.

In agreement with Wang et al. [51] and Antou et al. [52], the simulation results show that stress gradients are much higher than temperature ones. The calculated stresses and their gradients depend on the sample mechanical properties (coefficient of thermal expansion, Poisson's ratio, and Young's modulus) and the temperature. As both ceria and

copper exhibit higher coefficients of thermal expansion, relatively large magnitudes of the radial and hoop stresses which exceed the axial components are expected. Moreover, the gradients of radial, hoop, and axial stresses in the ceria and copper are much higher than that in alumina and tungsten.

In addition, the sample aspect ratios also exert a significant influence on the stress distributions. Simulation results indicated that the stress distributions are relatively uniform for the samples with smaller aspect ratios because the temperature and corresponding gradients are directly proportional to the aspect ratio of the sample (as stated in the Chapter 2); the smaller the aspect ratio, the lower the temperature and its gradients, and subsequently, the more uniform the stress distributions.

## Chapter 4

### Densification Process Modeling

#### 4.1 Introduction

The three-way thermal, electrical, and mechanical coupling model, which is decoupled into thermal-electric and thermal-mechanical modules, was introduced in the previous chapters. However, the densification effect of the powder compact during the SPS process has not been considered yet. Based on the three-way coupling finite element model, an integrated experimental/numerical methodology, in which the densification of the sintering materials can be simulated, is developed in this chapter. To explore the capabilities of the methodology, a case study is presented and the densification effect on the temperature and stress distributions is also investigated by taking into account the temperature-density dependent properties of the sintering material.

#### 4.2 Finite Element Modeling Details

##### 4.2.1 Theory

For a given powder compact used in the SPS process, the porosity, which describes the fraction of void space in the material, is defined by:

$$\phi = \frac{V_{void}}{V_T} \quad (4-1)$$

where,  $V_{void}$  is the volume of void-space and  $V_T$  is the total volume of the powder compact.

Moreover, the instantaneous relative density of the powder compact is specified as:

$$\rho_r = \frac{\rho(t)}{\rho_0} \quad (4-2)$$

where,  $\rho(t)$  is the instantaneous density of the powder compact and  $\rho_0$  corresponds to the theoretical density of the fully dense material. Considering mass conservation, the instantaneous relative density can be rewritten as:

$$\rho_r = \frac{\rho(t)}{\rho_0} = \frac{V_0}{V(t)} \quad (4-3)$$

where,  $V(t)$  is the instantaneous volume of the compact which can be obtained through experimental measurement,  $V_0$  is the volume of the fully dense material calculated from the mass of the material, and  $V(t)$  and  $V_0$  are related by  $\rho(t) \cdot V(t) = \rho_0 \cdot V_0 = m$ , where  $m$  is the mass.

According to Equations (4-1) and (4-3), the relationship between porosity and relative density is:

$$\phi = \frac{V_{void}}{V(t)} = \frac{V(t) - V_0}{V(t)} = 1 - \rho_r \quad (4-4)$$

As the material properties of the powder compact vary with temperature and relative density during the SPS process, both temperature and density dependent thermal, electrical, and mechanical properties of the sintering material have to be considered in the simulation in order to investigate the densification effect on the temperature and stress

distributions. The temperature dependence material properties are given in Appendix A, while several empirical or semi-empirical relations are available in the literature to correlate thermal, electrical, and mechanical properties directly to porosity or relative density [56-63]. In this study, the density dependence of the material properties was assumed to be given by [60, 62, 63]:

$$\frac{k_{eff}}{k_s} = \exp(-1.5 \frac{\phi}{1 - \phi}) \quad (4-5a)$$

$$\frac{\sigma_{eff}}{\sigma_s} = \exp(-1.5 \frac{\phi}{1 - \phi}) \quad (4-5b)$$

$$\frac{E_{eff}}{E_s} = \exp(-2 \frac{\phi}{1 - \phi}) \quad (4-5c)$$

$$\frac{\nu_{eff}}{\nu_s} = 1 + \frac{3(1 - \nu_s^2)(1 - 5\nu_s)}{2\nu_s(7 - 5\nu_s)} \phi \quad (4-5d)$$

where,  $\phi$  is the porosity,  $k$  and  $\sigma$  are the thermal and electrical conductivity,  $E$  is the Young's modulus, and  $\nu$  is the Poisson's ratio. The subscripts  $s$  and  $eff$  indicate the fully dense and the effective values, respectively. It should be noted that the same effective thermal and electrical conductivity expression can only be assumed for metallic alloys [58], and not for the alumina used in this study. However, these expressions were adopted for comparative purpose since analogous relationships are not available for alumina.

#### 4.2.2 Numerical Implementation

The previous three-way coupling finite element model for alumina sample with aspect ratio equal to 0.5 was adopted for the densification analysis. All the boundary and initial conditions were kept the same. However, the temperature-density dependent material properties of alumina were used for the sample instead of temperature dependent ones.

As the displacement of the top surface of the upper spacer was measured during the SPS experiment, the instantaneous volume of the powder compact can be estimated by considering the compliance of the SPS system while ignoring the dimension change of the sample in the radial direction due to thermal and Poisson-type expansions. Hence, the instantaneous relative density of the sample can be calculated according to Equation (4-3), as shown in Figure 4-1.

In the simulation, a step-wise relative density curve was used instead. The entire densification period was evenly divided into 100 intervals, and a constant density was assumed for each. In addition, the sintering sample was treated as macroscopically homogenous. Based on the assumptions just discussed, the influence of density change on the temperature and stress distributions was investigated and then compared to a fully dense material.

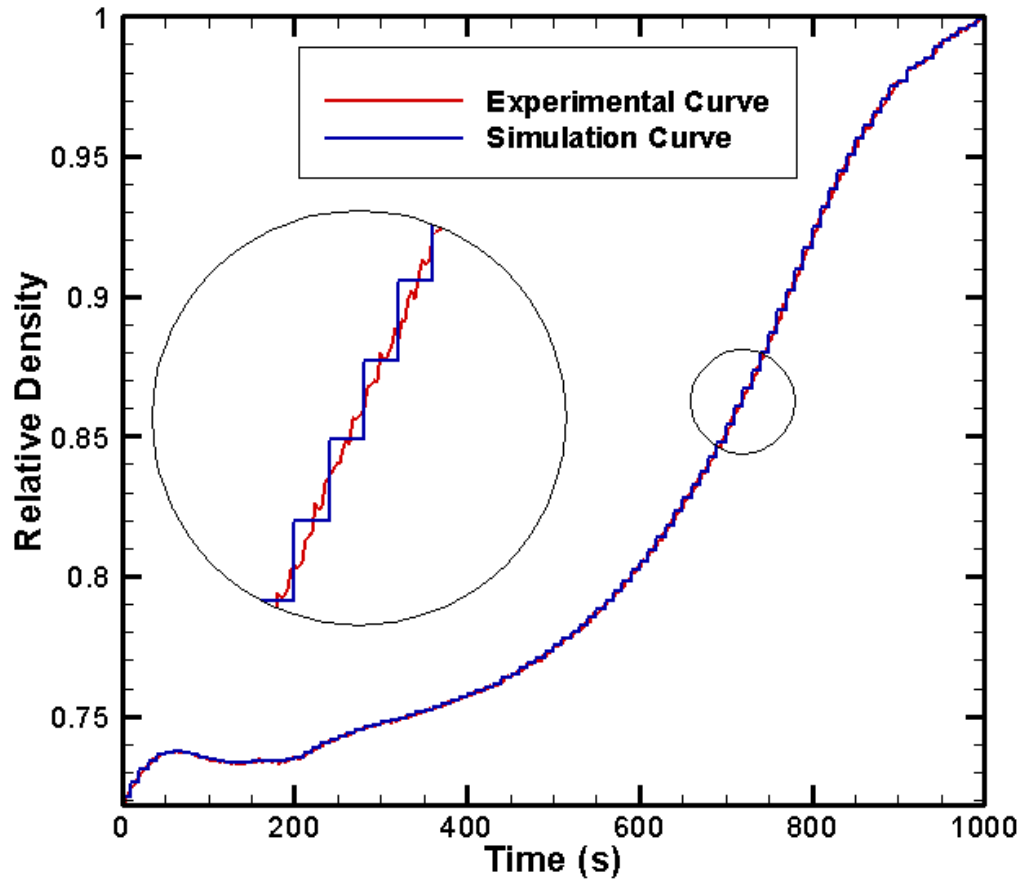


Figure 4-1. Assumed experimental curve (red) for the relative density of the powder compact; Step-wise relative density curve (blue) used in the simulation.

### 4.3 Results and Discussion

#### 4.3.1 Temperature Distribution

The simulated temperature evolution at the center points of each sample is shown in Figure 4-2 for the 800 A constant DC current. Figures 4-3 to 4-6 also show the

temperature profiles in both the radial and vertical directions of the punch/sample/die assembly at different time steps. According to these figures, the temperature in the evolving density case is slightly higher than that of the constant density, especially in the sample region. With each increment of heating time, the difference decreases gradually. When the temperature of the system reaches the steady state (after ~800 s), the temperature profiles of the two cases are almost the same. However, no conspicuous differences can be observed in the punch-die region.

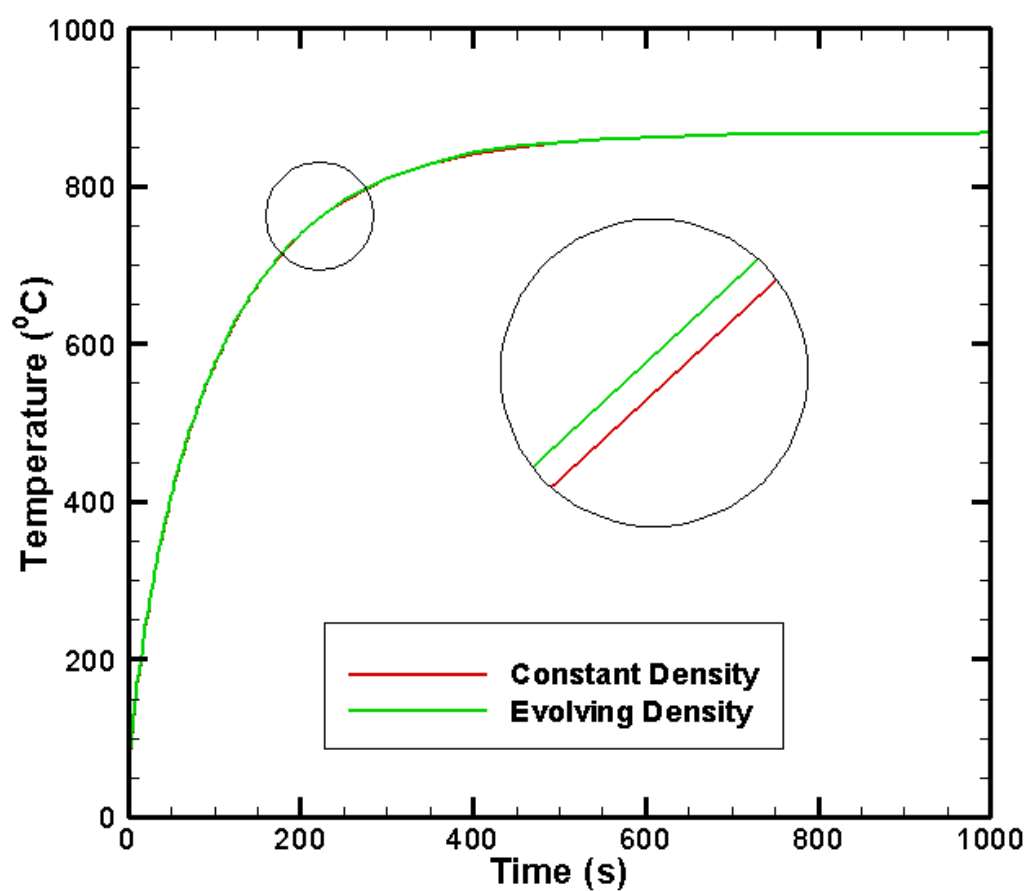


Figure 4-2. Temperature evolution at the center points of the alumina samples with constant and evolving densities.

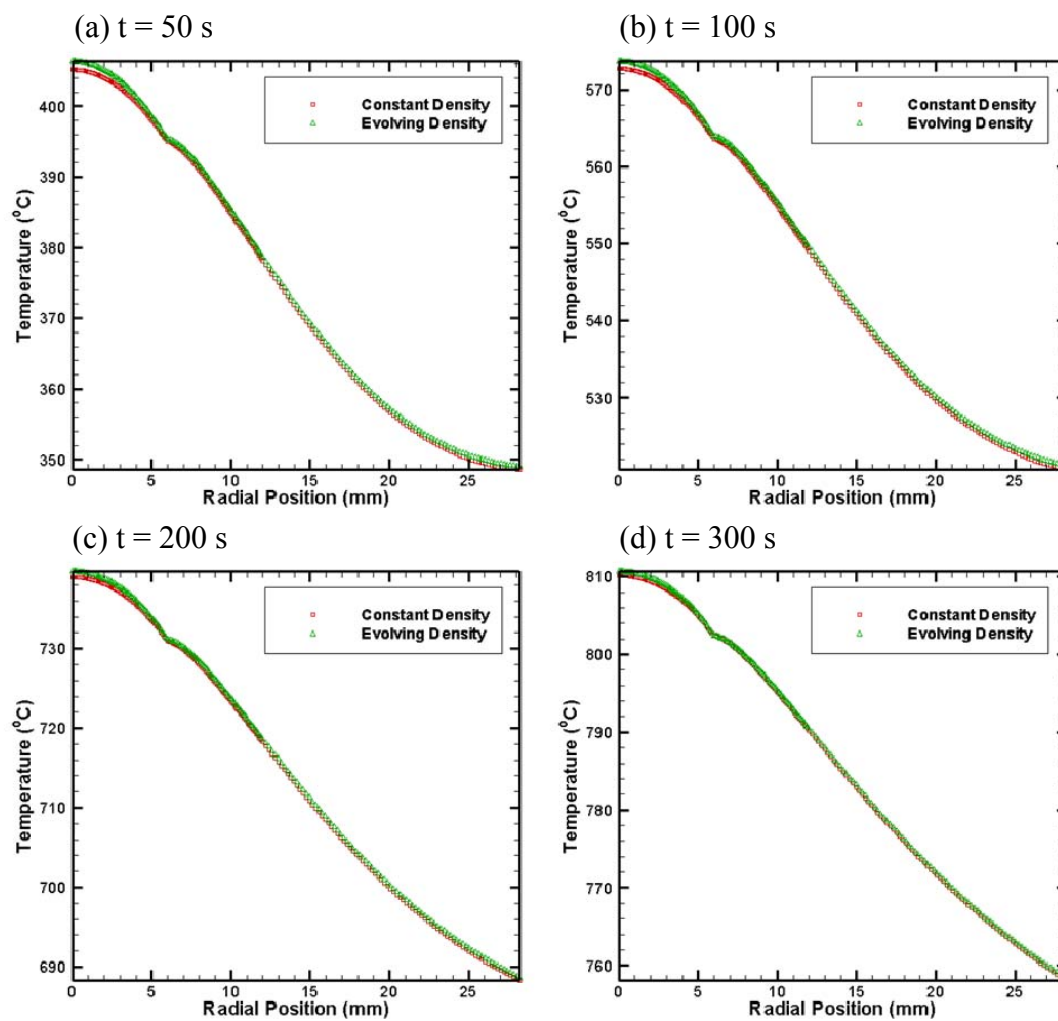


Figure 4-3. Comparison of the radial temperature profiles in the middle cross-section of the sample and the die at different time steps: (a)  $t=50$  s, (b)  $t=100$  s, (c)  $t=200$  s, and (d)  $t=300$  s.

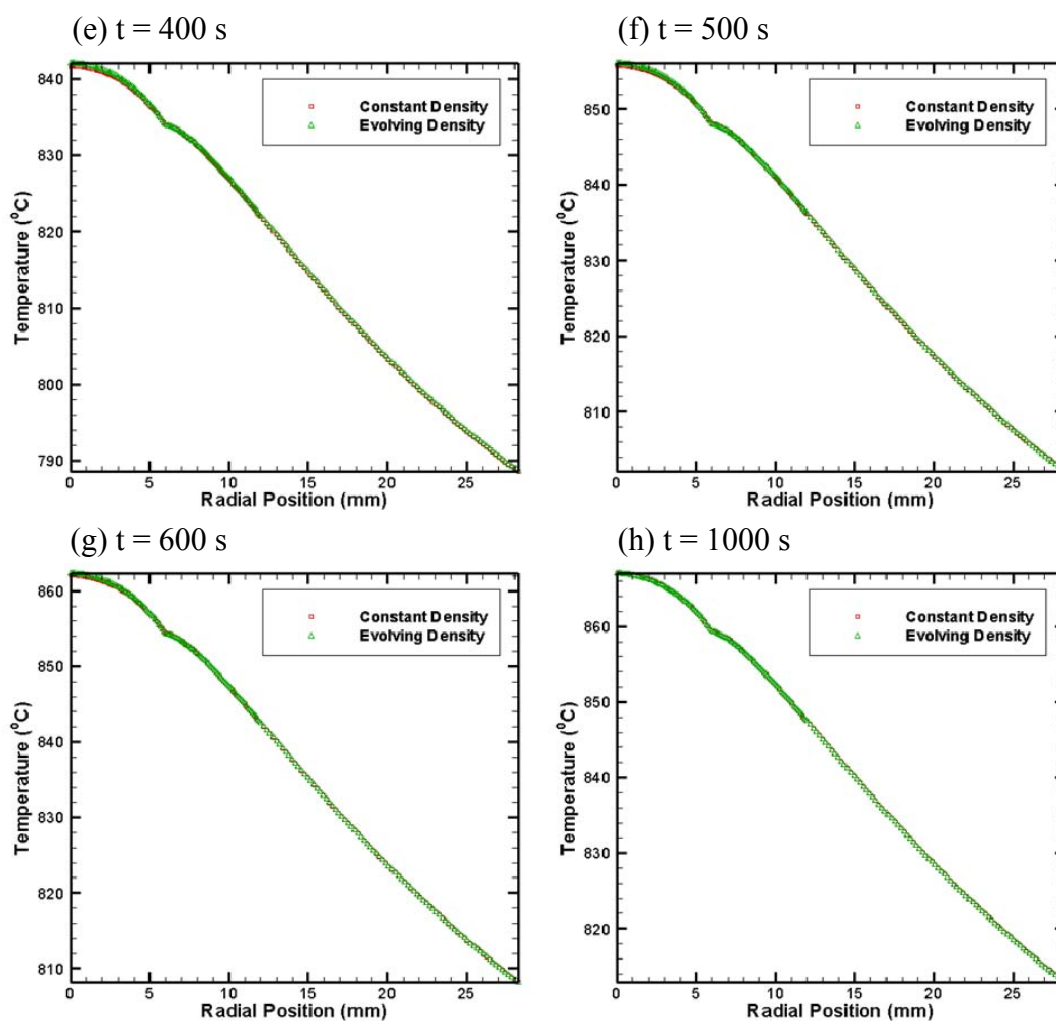


Figure 4-4. Comparison of the radial temperature profiles in the middle cross-section of the sample and the die at different time steps: (e)  $t=400$  s, (f)  $t=500$  s, (g)  $t=600$  s, and (h)  $t=1000$  s.

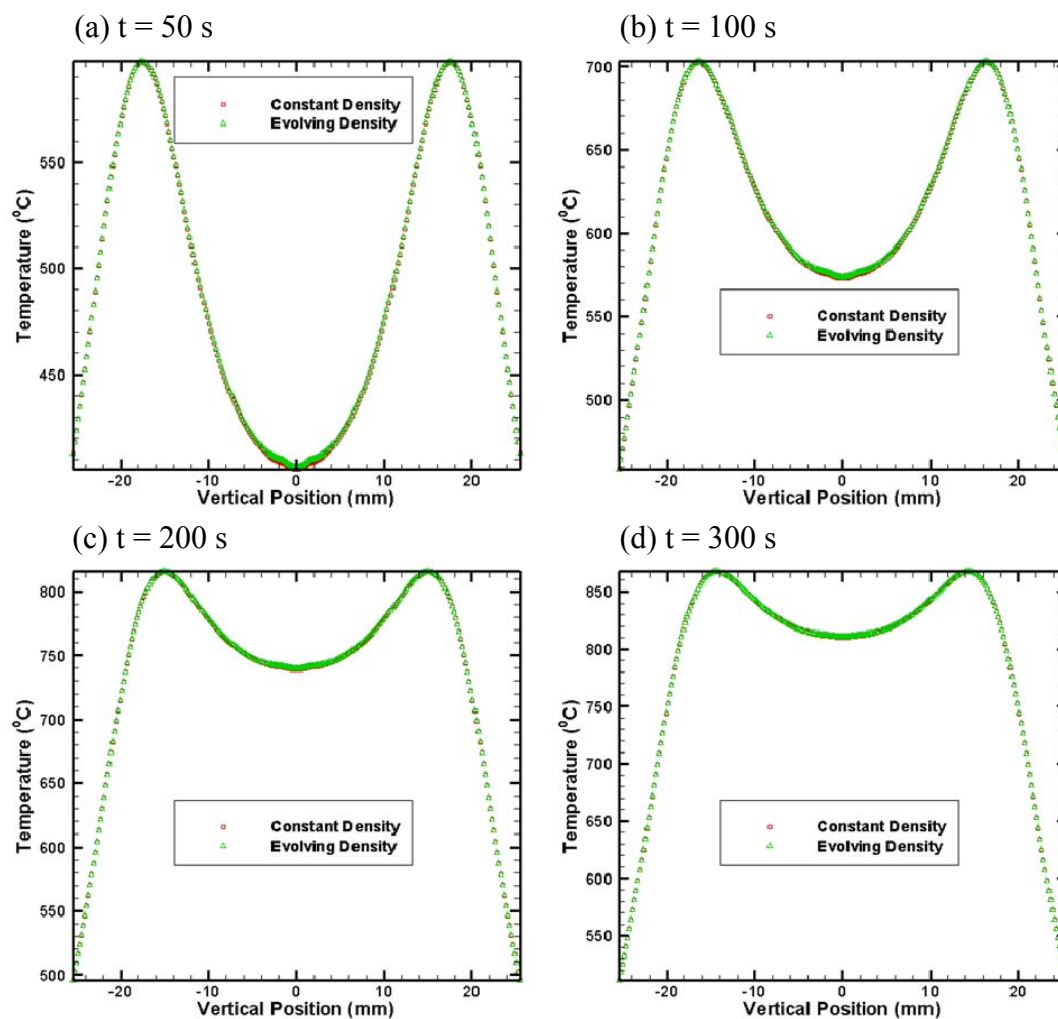


Figure 4-5. Comparison of the vertical temperature profiles along the axis of symmetry in the punch/sample/die assembly at different time steps: (a)  $t=50$  s, (b)  $t=100$  s, (c)  $t=200$  s, and (d)  $t=300$  s.

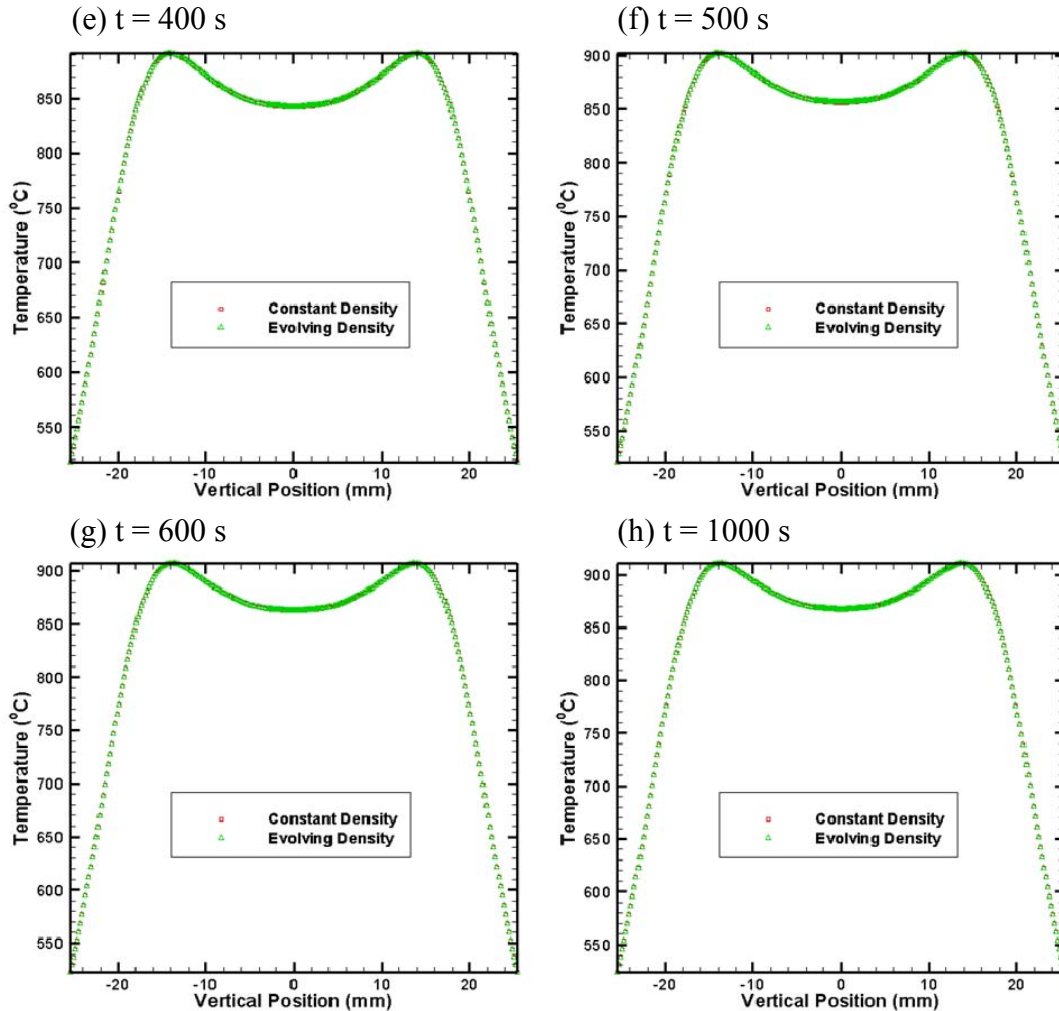


Figure 4-6. Comparison of the vertical temperature profiles along the axis of symmetry in the punch/sample/die assembly at different time steps: (e)  $t=400$  s, (f)  $t=500$  s, (g)  $t=600$  s, and (h)  $t=1000$  s.

Figures 4-7 to 4-14 show the contour plots of the temperature distribution in the alumina sample at different time steps. The magnitude difference of the temperature between the two adjacent isolines is  $0.25$  °C. Moreover, the temperature profiles in both radial and vertical directions of the sample are plotted in Figures 4-15 to 4-18. As indicated in these results, the magnitude of the temperature in the evolving density case is

higher than that of the constant density before the temperature reaches steady state; larger temperature gradients exist in the case with evolving density. This is because the thermal conductivity of the porous powder compact is lower than that of the fully dense material. When the Joule heat of the SPS system generated in the graphite punches and die transferred to the sample, more local heating can be observed in the evolving density case. However, the temperature in the sample with fully dense material properties is more uniform due to its higher thermal conductivity.

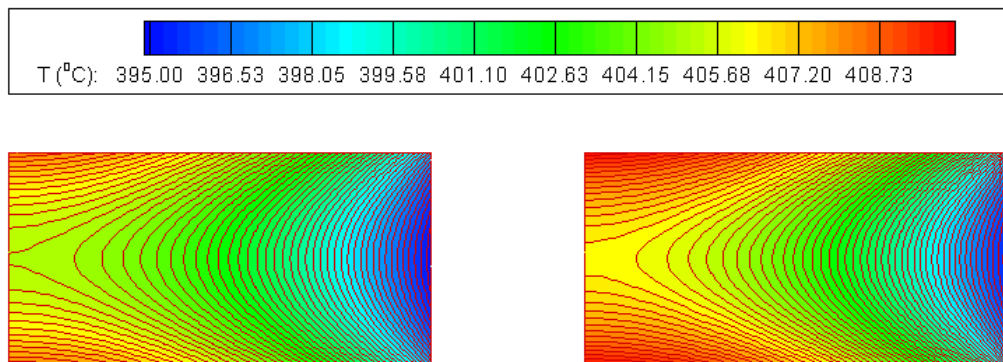


Figure 4-7. Contour plots of the temperature distribution in the region of samples with constant density (left) and evolving density (right) at  $t=50$  s.

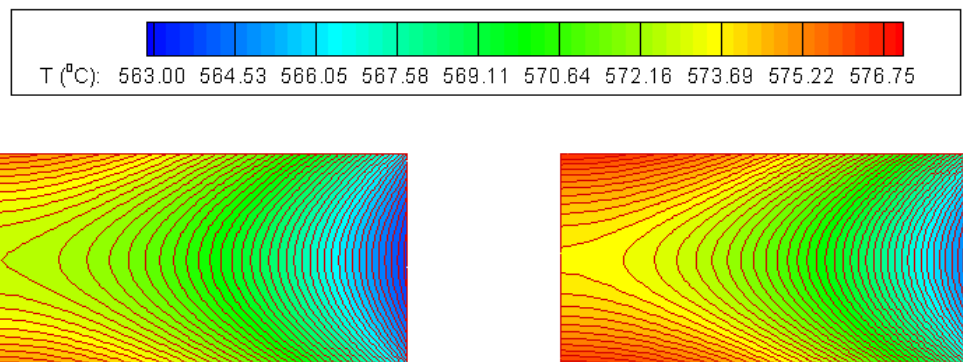


Figure 4-8. Contour plots of the temperature distribution in the region of samples with constant density (left) and evolving density (right) at  $t=100$  s.

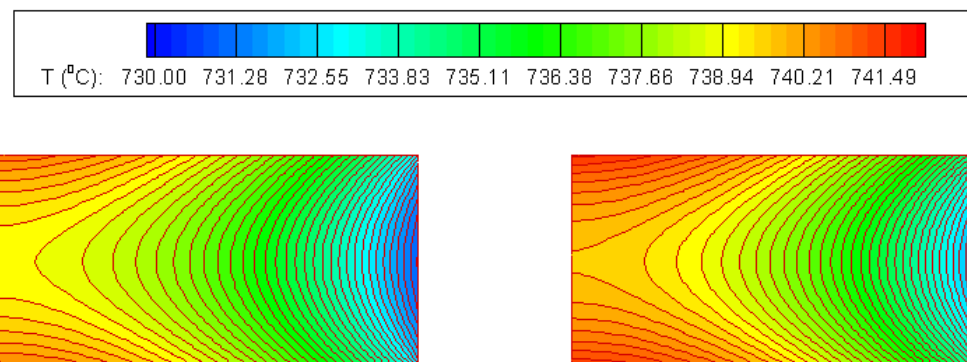


Figure 4-9. Contour plots of the temperature distribution in the region of samples with constant density (left) and evolving density (right) at  $t=200$  s.

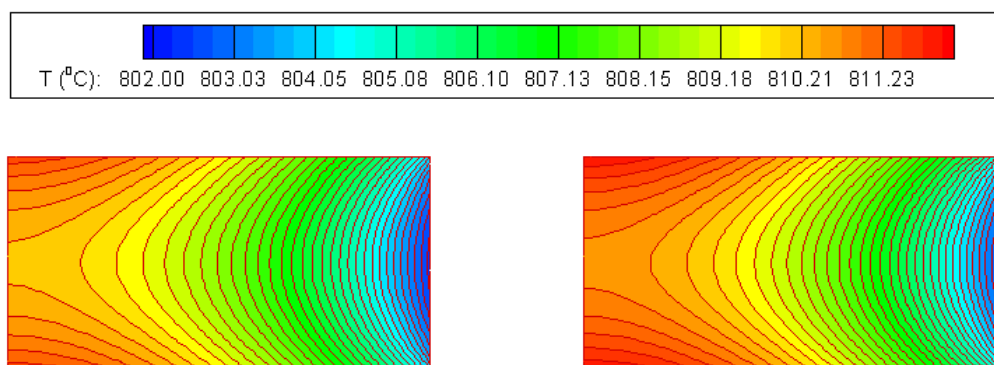


Figure 4-10. Contour plots of the temperature distribution in the region of samples with constant density (left) and evolving density (right) at  $t=300$  s.

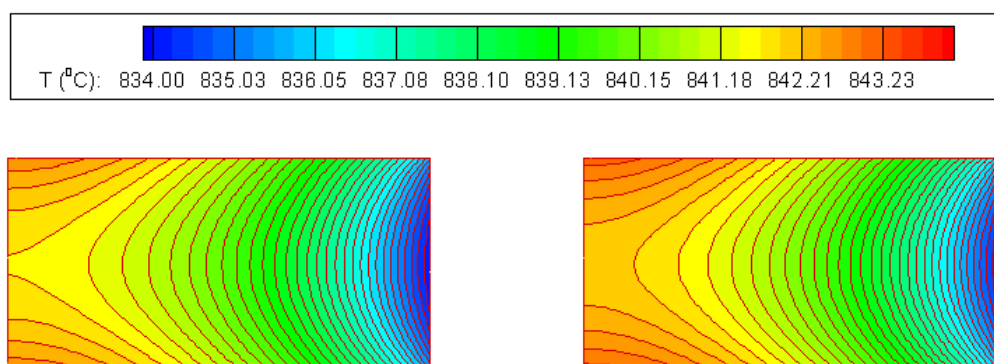


Figure 4-11. Contour plots of the temperature distribution in the region of samples with constant density (left) and evolving density (right) at  $t=400$  s.

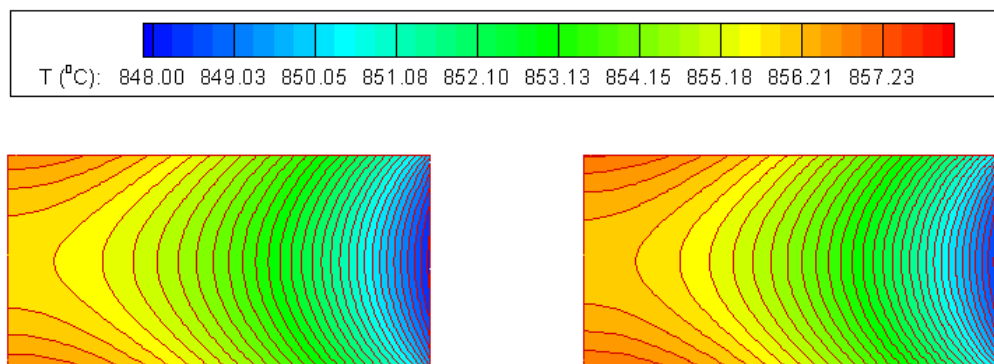


Figure 4-12. Contour plots of the temperature distribution in the region of samples with constant density (left) and evolving density (right) at  $t=500$  s.

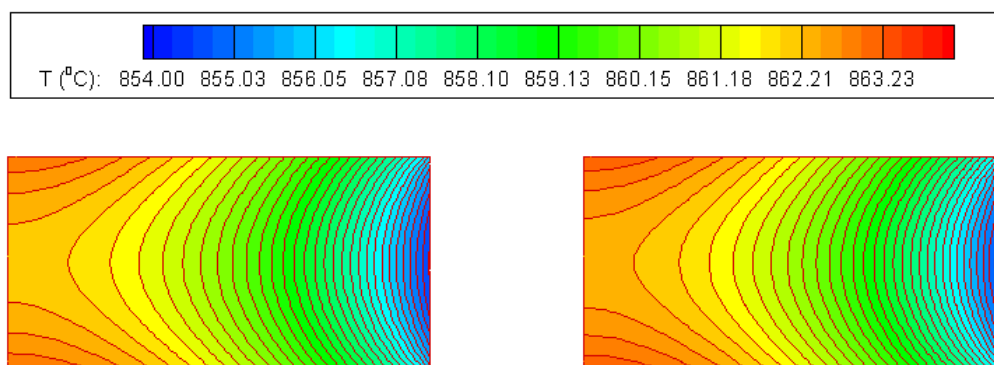


Figure 4-13. Contour plots of the temperature distribution in the region of samples with constant density (left) and evolving density (right) at  $t=600$  s.

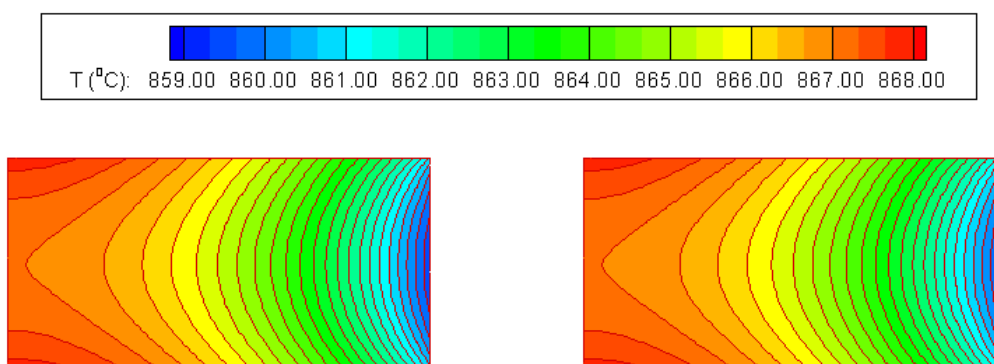


Figure 4-14. Contour plots of the temperature distribution in the region of samples with constant density (left) and evolving density (right) at  $t=1000$  s.

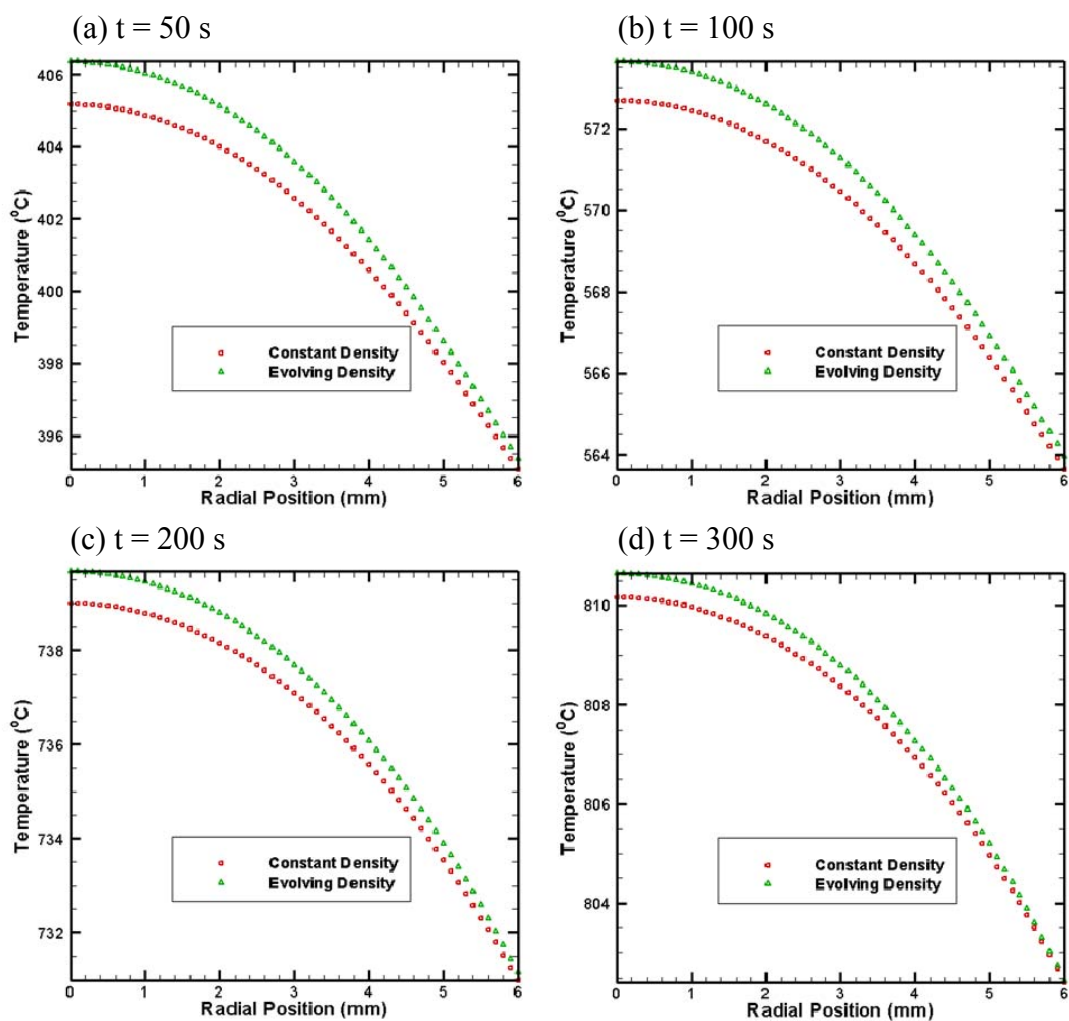


Figure 4-15. Comparison of the radial temperature profiles in the middle cross-section of the sample at different time steps: (a)  $t=50$  s, (b)  $t=100$  s, (c)  $t=200$  s, and (d)  $t=300$  s.

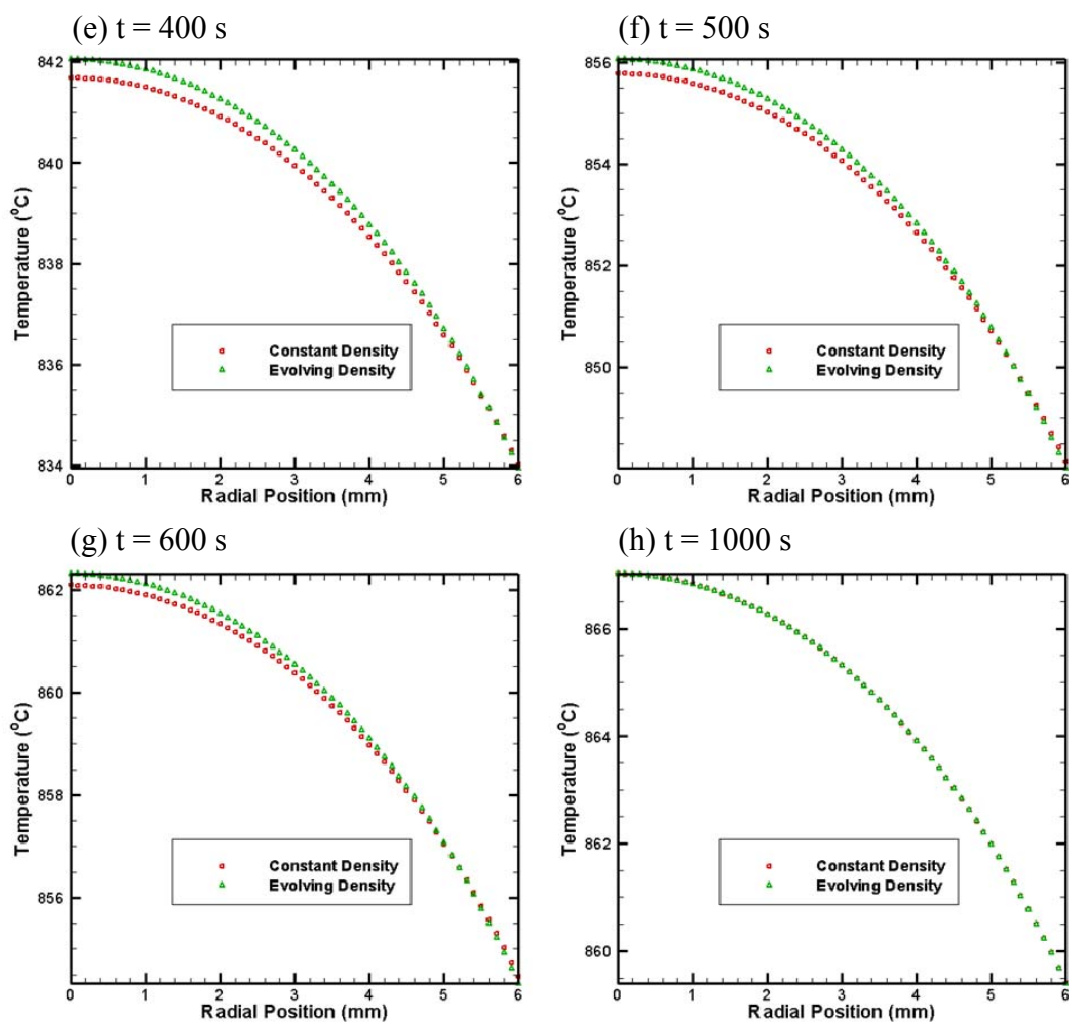


Figure 4-16. Comparison of the radial temperature profiles in the middle cross-section of the sample at different time steps: (e)  $t=400$  s, (f)  $t=500$  s, (g)  $t=600$  s, and (h)  $t=1000$  s.

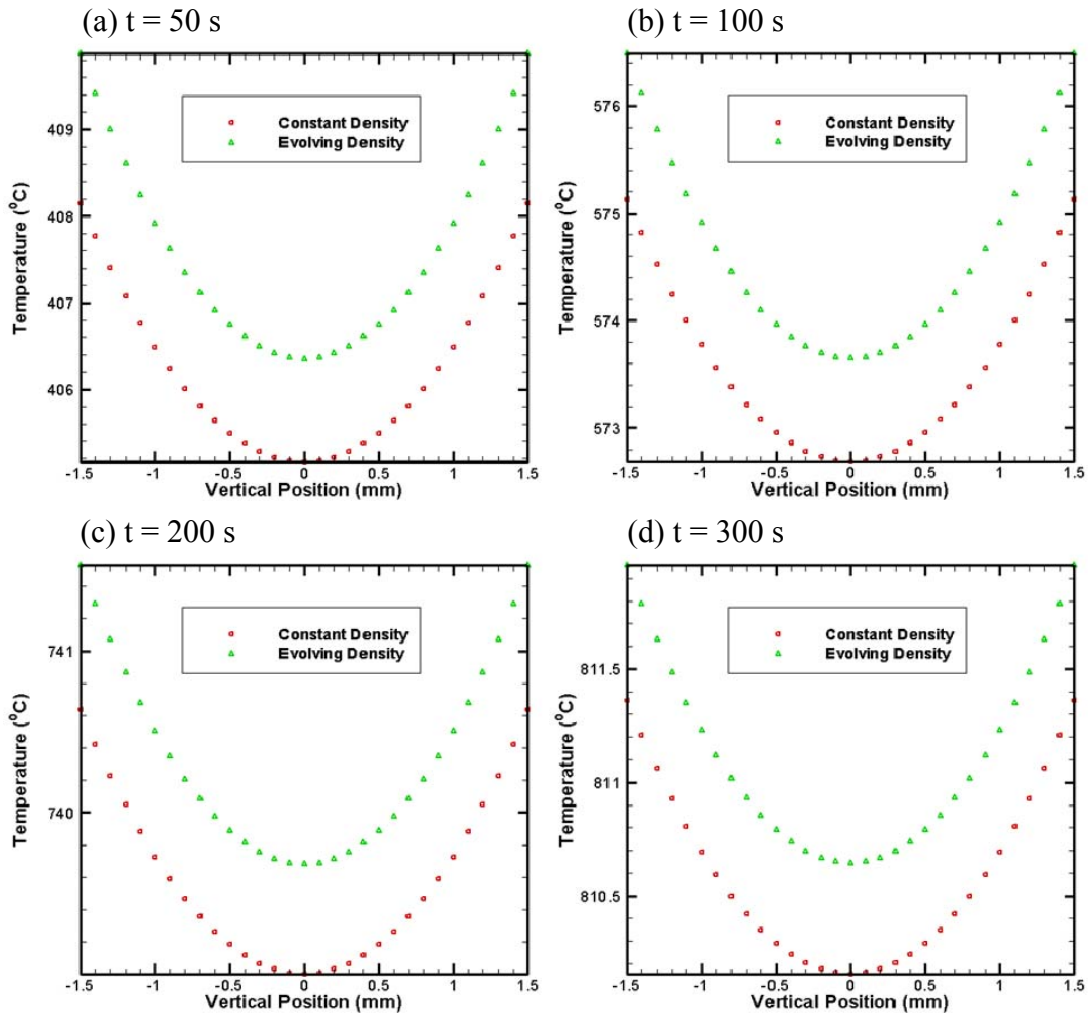


Figure 4-17. Comparison of the vertical temperature profiles along the axis of symmetry in the sample at different time steps: (a)  $t=50$  s, (b)  $t=100$  s, (c)  $t=200$  s, and (d)  $t=300$  s.

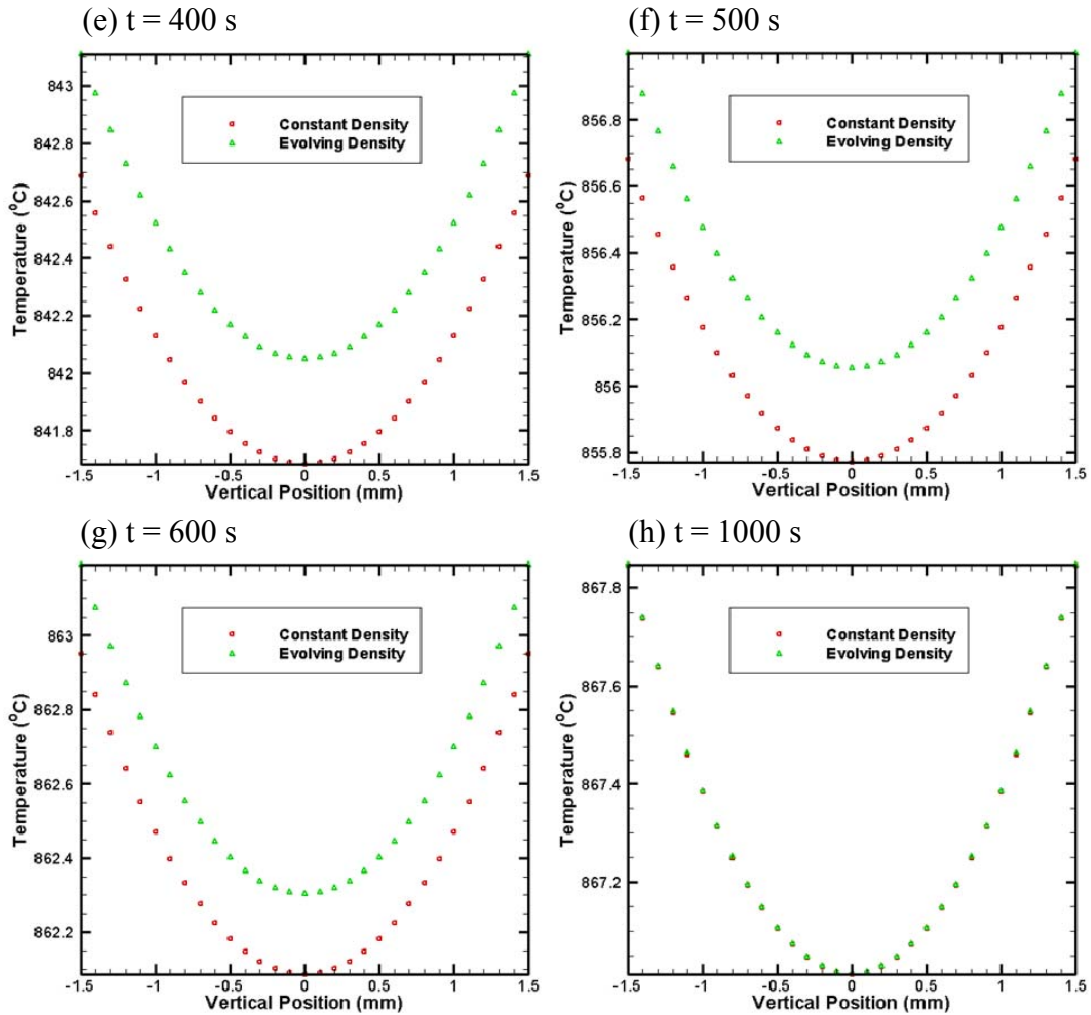


Figure 4-18. Comparison of the vertical temperature profiles along the axis of symmetry in the sample at different time steps: (e)  $t=400$  s, (f)  $t=500$  s, (g)  $t=600$  s, and (h)  $t=1000$  s.

### 4.3.2 Stress Distributions

The stress distributions in the radial, hoop, and axial directions in the sample region at different time steps are shown in Figures 4-19 to 4-42; magnitude difference of the stresses between the two adjacent isolines in Figures 4-19 to 4-34 is 1.0 MPa, while a 0.5 MPa difference between two adjacent isolines in Figures 4-35 to 4-42 exists. As revealed in these figures, the magnitudes of the radial and axial stresses of the constant density case are always higher than that of the evolving density before the powder is fully condensed. However, the magnitudes of the axial stress of the two cases show no obvious difference. In addition, lower stress gradients exist in the sample with evolving density when compared with the constant density case; the stress gradients decrease with each increment of sintering time until approximating 300 s to 500 s, and then begin to increase.

Figures 4-43 to 4-58 also show the stress profiles in the middle cross-section and along the axis of symmetry of the sample. Once again, larger stress gradients can be observed for the case of constant density. Moreover, the stress gradients in the middle cross-section of the sample turn out to be more severe than that along the axis of symmetry, especially for the radial and hoop stresses. Even though the magnitude may vary slightly due to the thermal expansion effect, the axial stress in both cases is very close to the nominal stress generated by the externally applied pressure.

According to the simulation results, the discrepancies of the stress distributions between the two cases with constant and evolving densities can be attributed to the density dependent mechanical properties of the sample. As the densification effect of the

powder compact is considered in the case with evolving density, the Young's modulus and the Poisson's ratio change with density, and their values are less than that of the fully dense material. Therefore, less Poisson-type expansion occurs during the sintering process, which subsequently leads to lower magnitudes of the radial and hoop stresses. It is also worth noting that for the parameters used in this study, there exists a critical moment during the sintering process, specifically between 300 s and 500 s, at which the most uniform stress distributions can be expected.

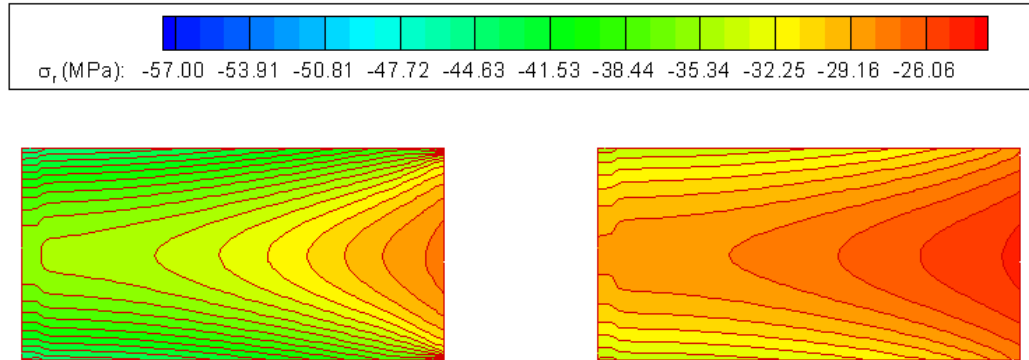


Figure 4-19. Contour plots of the radial stress distribution in the region of samples with constant density (left) and evolving density (right) at  $t=50$  s.

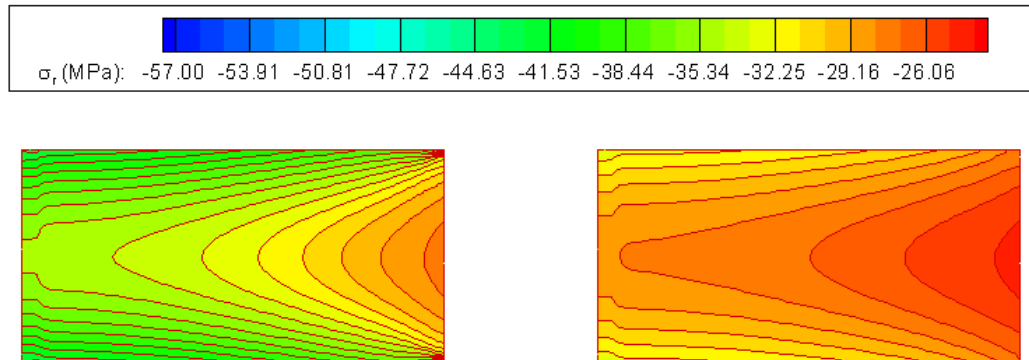


Figure 4-20. Contour plots of the radial stress distribution in the region of samples with constant density (left) and evolving density (right) at  $t=100$  s.

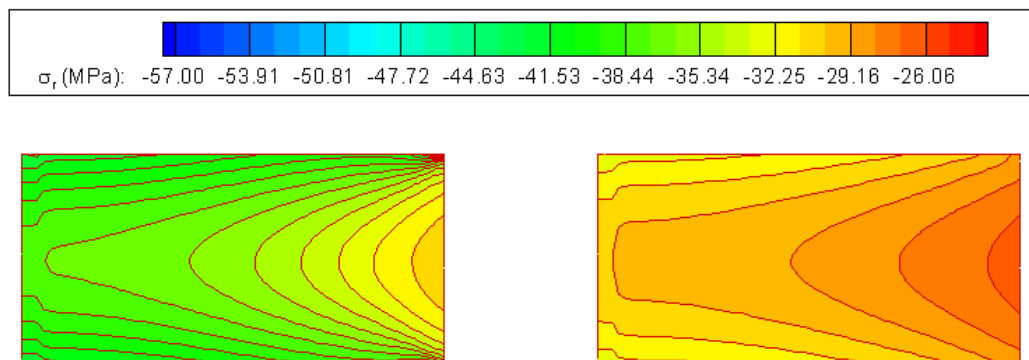


Figure 4-21. Contour plots of the radial stress distribution in the region of samples with constant density (left) and evolving density (right) at  $t=200$  s.

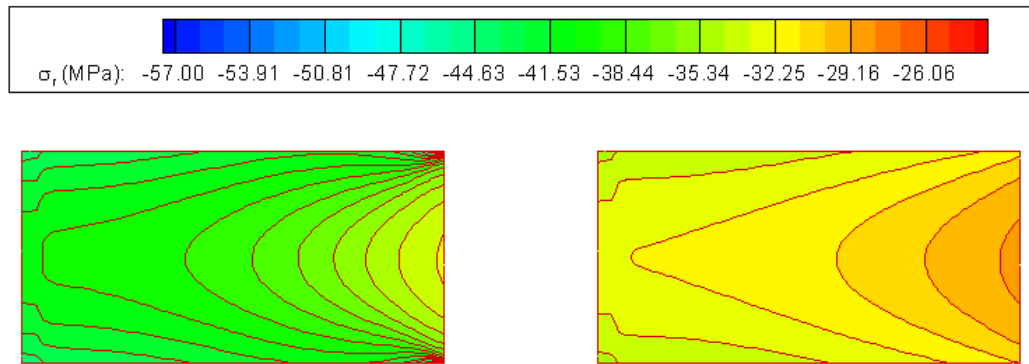


Figure 4-22. Contour plots of the radial stress distribution in the region of samples with constant density (left) and evolving density (right) at  $t=300$  s.

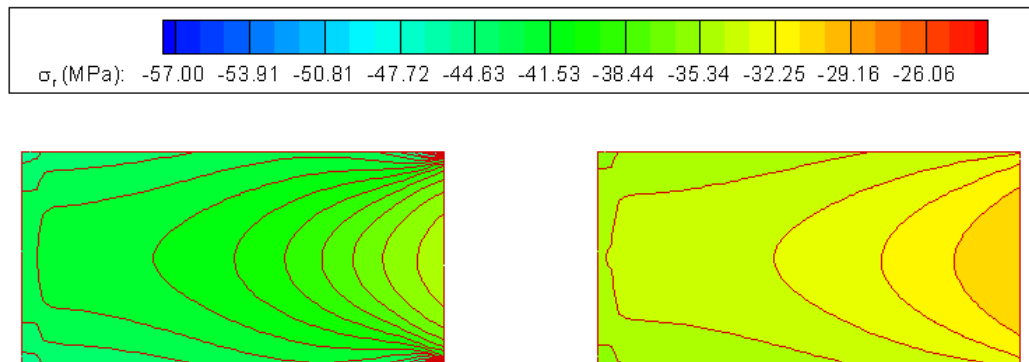


Figure 4-23. Contour plots of the radial stress distribution in the region of samples with constant density (left) and evolving density (right) at  $t=400$  s.

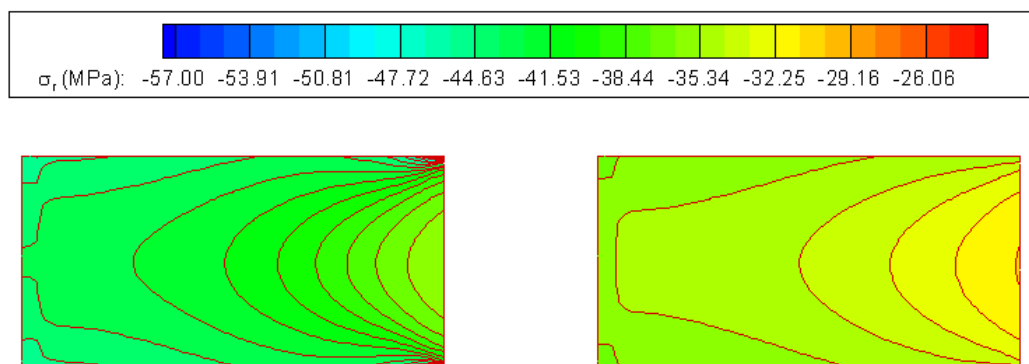


Figure 4-24. Contour plots of the radial stress distribution in the region of samples with constant density (left) and evolving density (right) at  $t=500$  s.

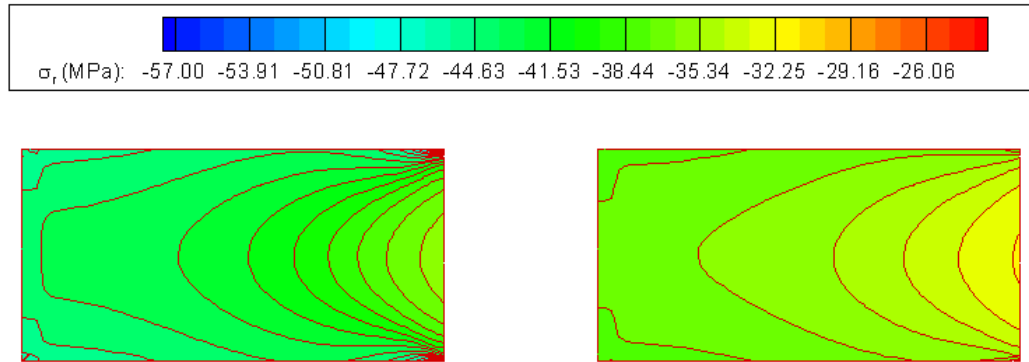


Figure 4-25. Contour plots of the radial stress distribution in the region of samples with constant density (left) and evolving density (right) at  $t=600$  s.

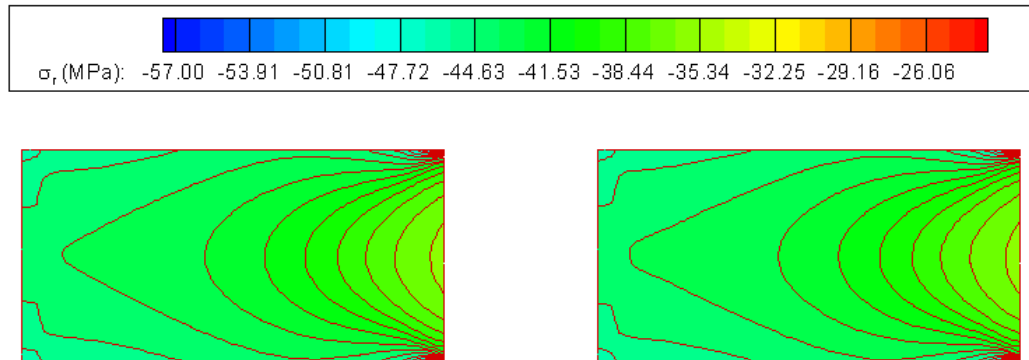


Figure 4-26. Contour plots of the radial stress distribution in the region of samples with constant density (left) and evolving density (right) at  $t=1000$  s.

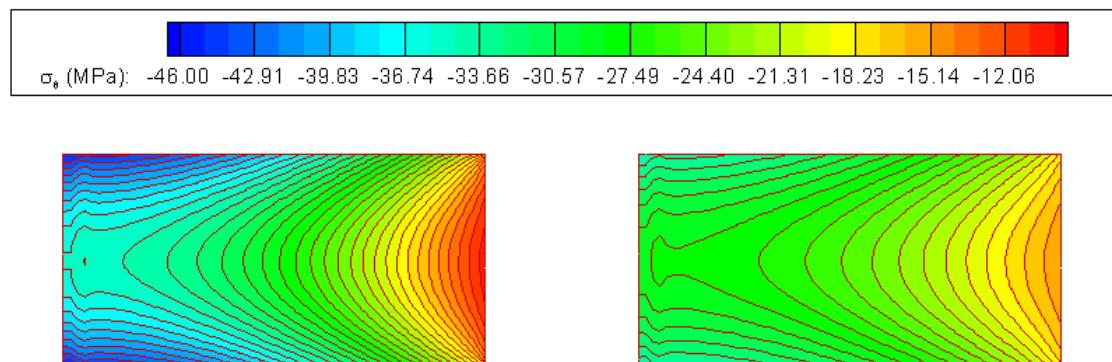


Figure 4-27. Contour plots of the hoop stress distribution in the region of samples with constant density (left) and evolving density (right) at  $t=50$  s.

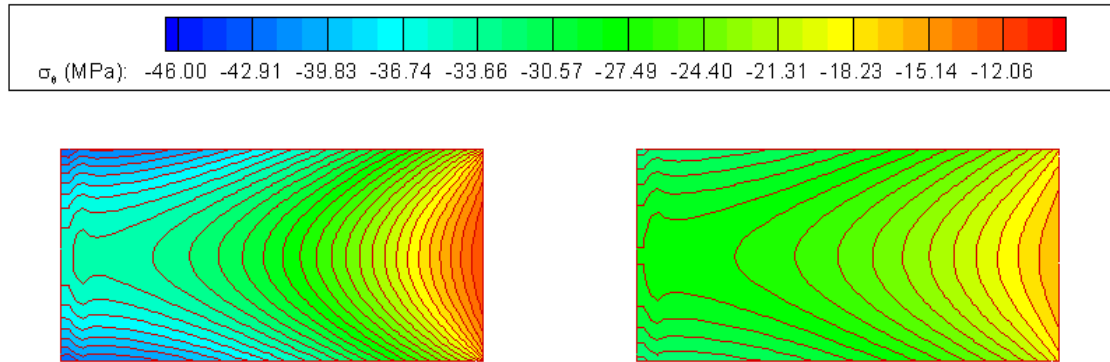


Figure 4-28. Contour plots of the hoop stress distribution in the region of samples with constant density (left) and evolving density (right) at  $t=100$  s.

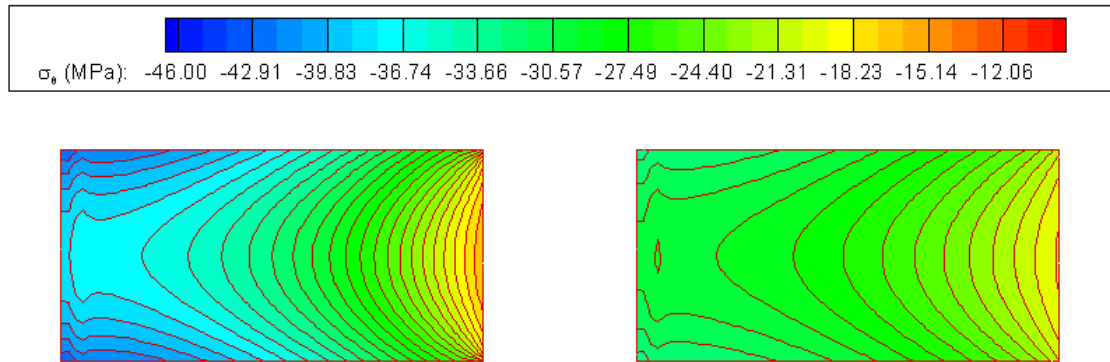


Figure 4-29. Contour plots of the hoop stress distribution in the region of samples with constant density (left) and evolving density (right) at  $t=200$  s.

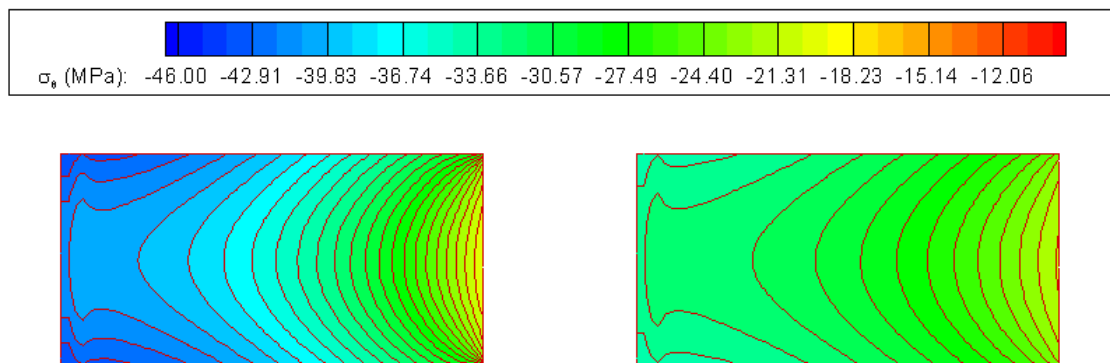


Figure 4-30. Contour plots of the hoop stress distribution in the region of samples with constant density (left) and evolving density (right) at  $t=300$  s.

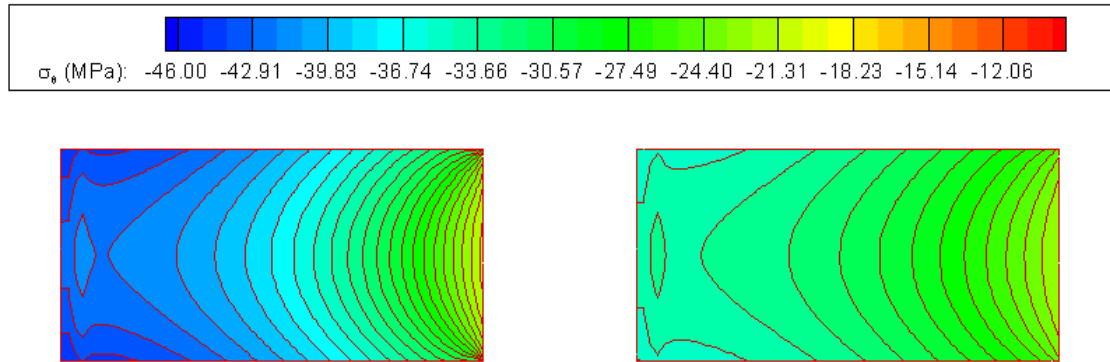


Figure 4-31. Contour plots of the hoop stress distribution in the region of samples with constant density (left) and evolving density (right) at  $t=400$  s.

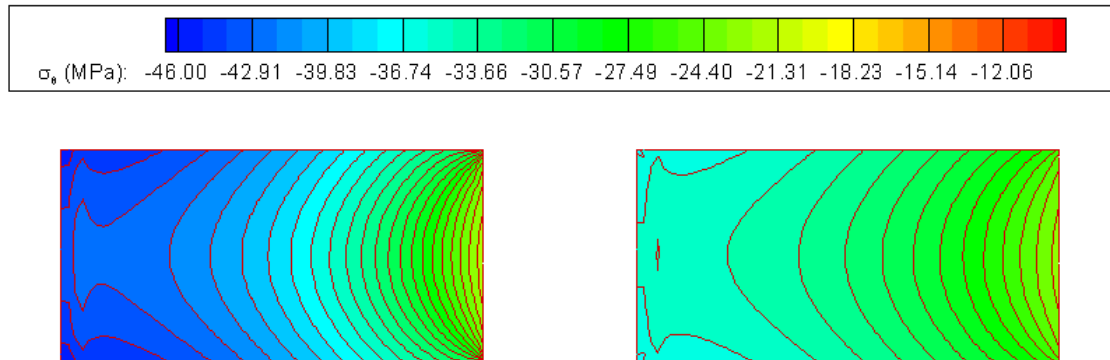


Figure 4-32. Contour plots of the hoop stress distribution in the region of samples with constant density (left) and evolving density (right) at  $t=500$  s.

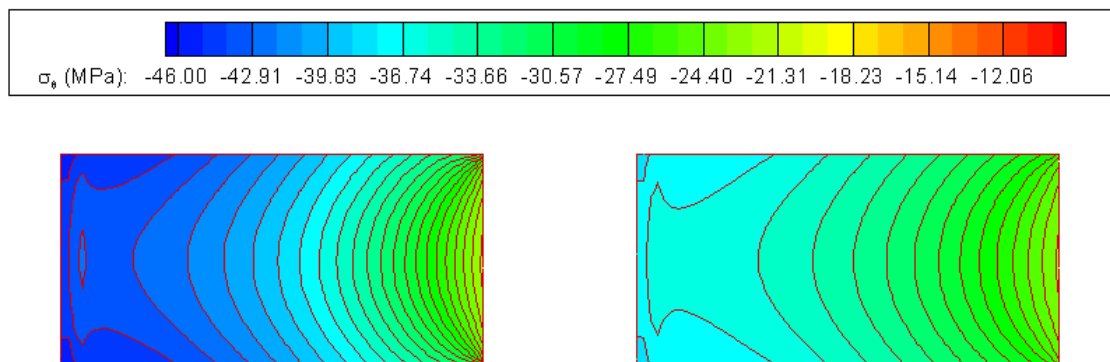


Figure 4-33. Contour plots of the hoop stress distribution in the region of samples with constant density (left) and evolving density (right) at  $t=600$  s.

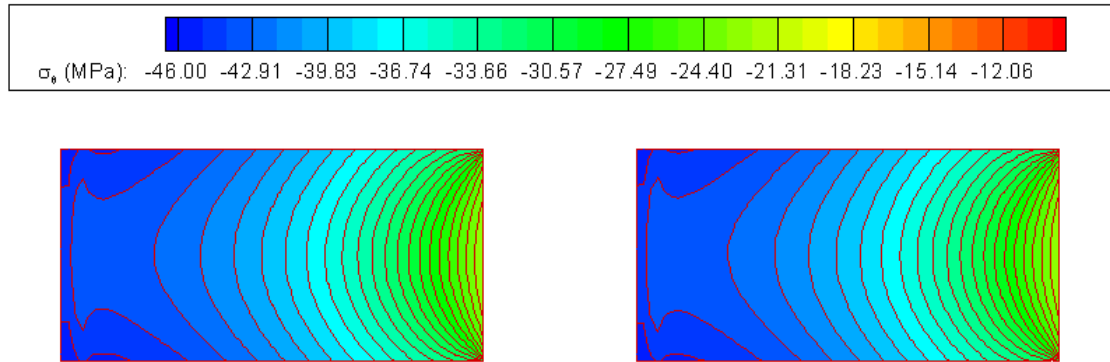


Figure 4-34. Contour plots of the hoop stress distribution in the region of samples with constant density (left) and evolving density (right) at  $t=1000$  s.

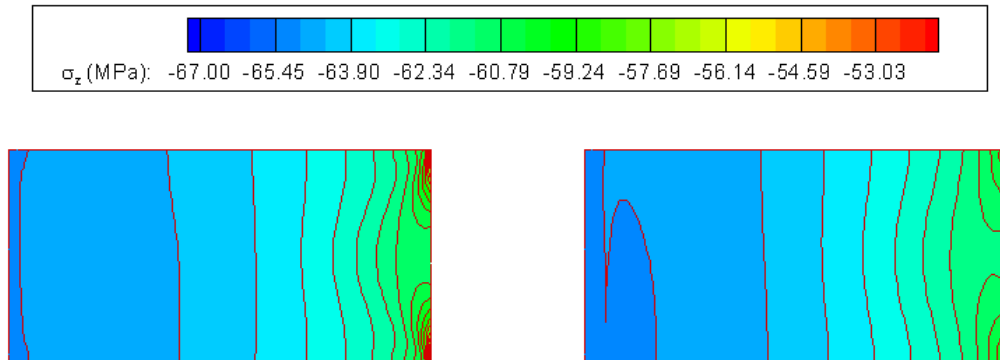


Figure 4-35. Contour plots of the axial stress distribution in the region of samples with constant density (left) and evolving density (right) at  $t=50$  s.

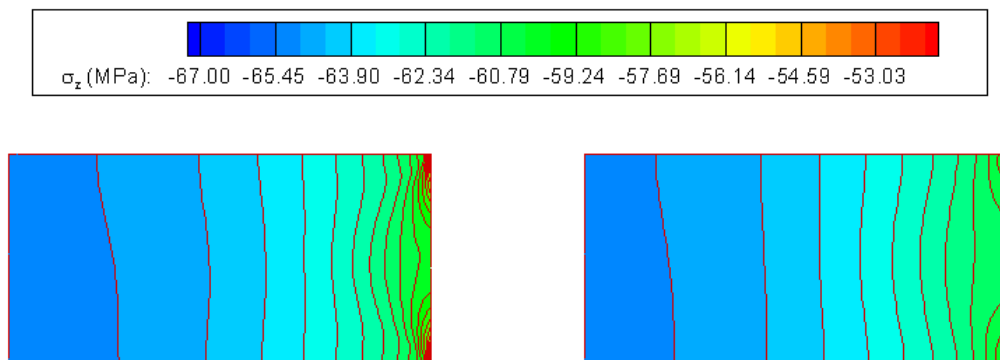


Figure 4-36. Contour plots of the axial stress distribution in the region of samples with constant density (left) and evolving density (right) at  $t=100$  s.

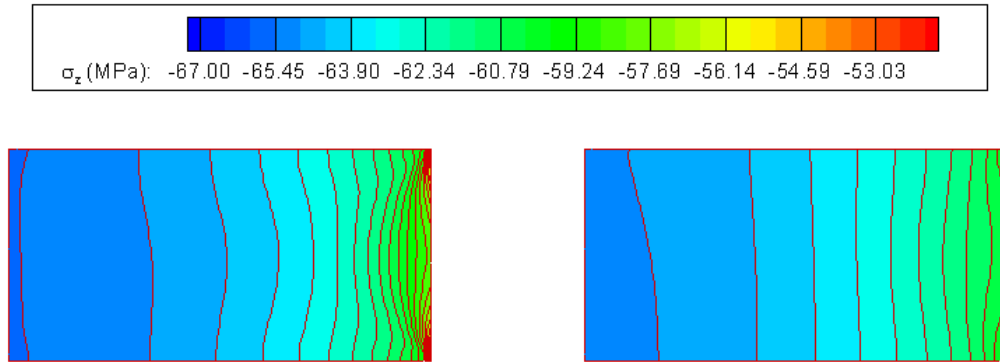


Figure 4-37. Contour plots of the axial stress distribution in the region of samples with constant density (left) and evolving density (right) at  $t=200$  s.

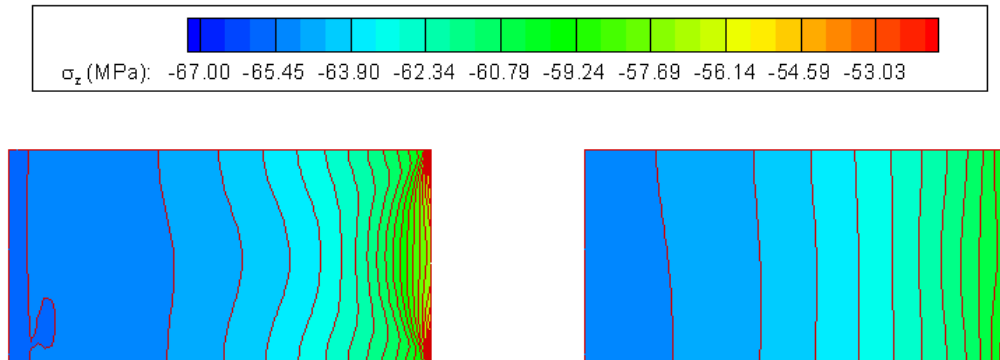


Figure 4-38. Contour plots of the axial stress distribution in the region of samples with constant density (left) and evolving density (right) at  $t=300$  s.

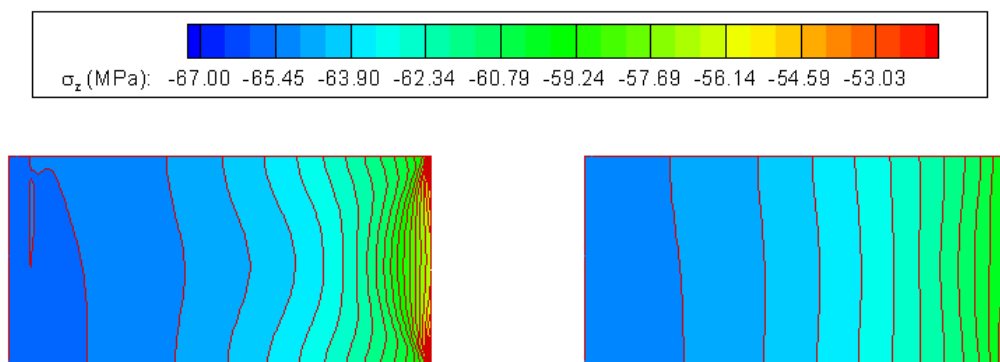


Figure 4-39. Contour plots of the axial stress distribution in the region of samples with constant density (left) and evolving density (right) at  $t=400$  s.

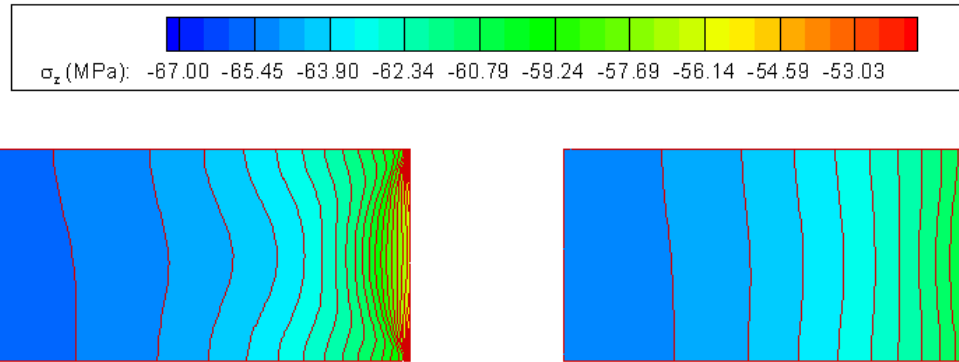


Figure 4-40. Contour plots of the axial stress distribution in the region of samples with constant density (left) and evolving density (right) at  $t=500$  s.

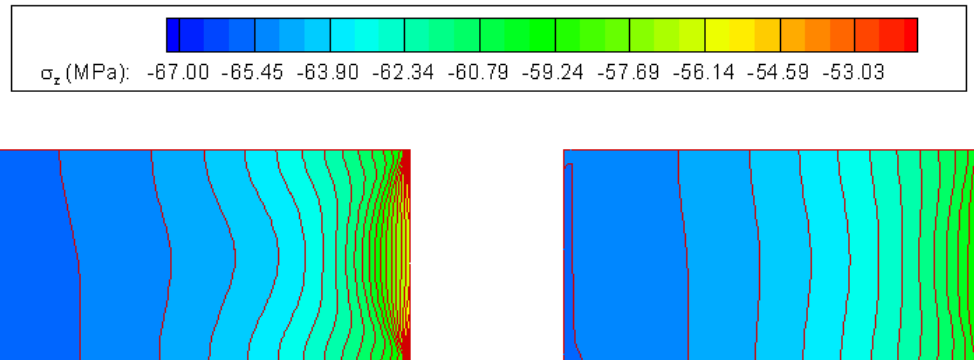


Figure 4-41. Contour plots of the axial stress distribution in the region of samples with constant density (left) and evolving density (right) at  $t=600$  s.

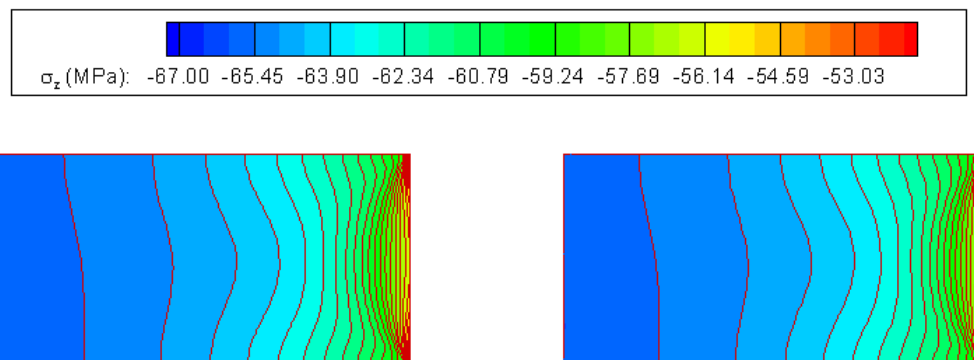


Figure 4-42. Contour plots of the axial stress distribution in the region of samples with constant density (left) and evolving density (right) at  $t=1000$  s.

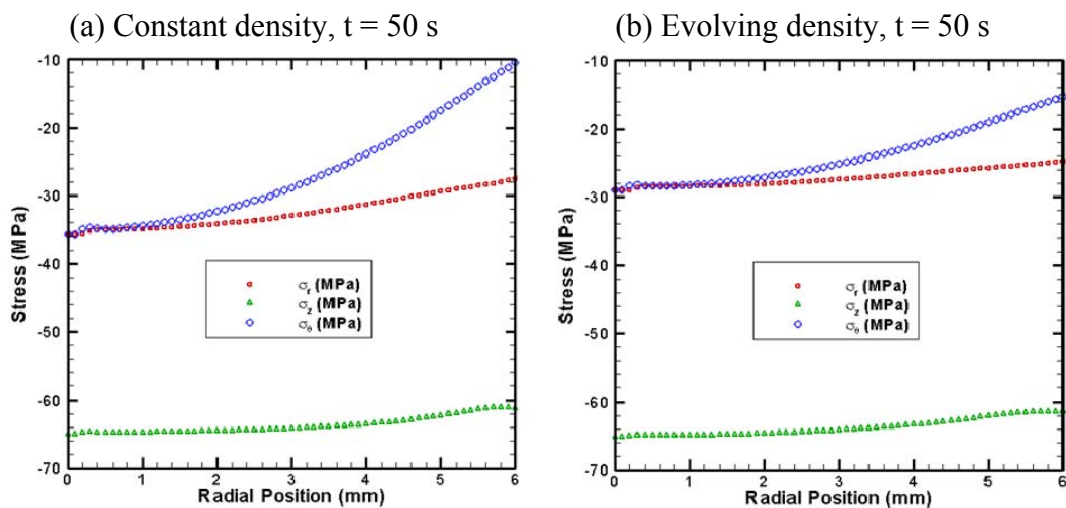


Figure 4-43. Comparison of the stress profiles in the middle cross-section of the samples with constant density (left) and evolving density (right) at  $t=50$  s.

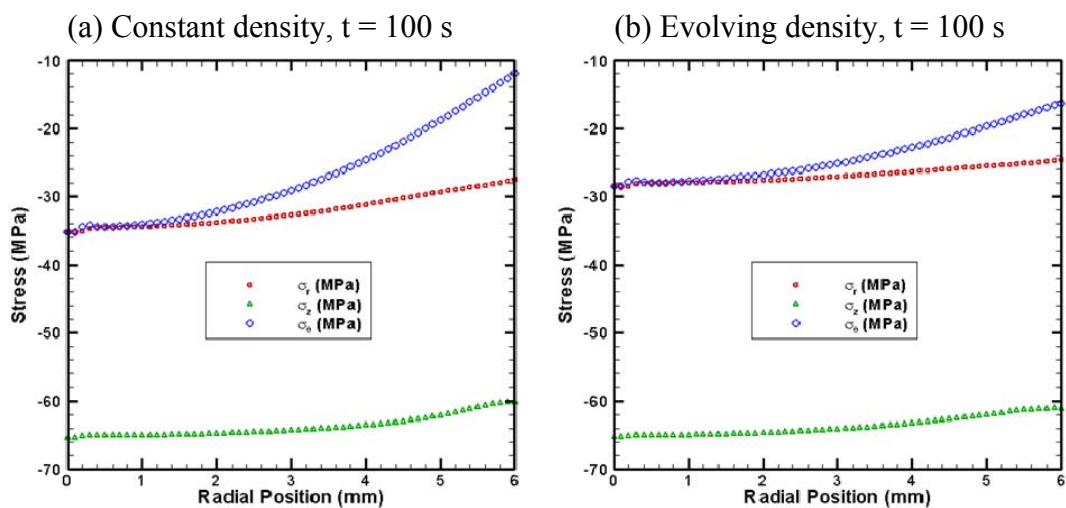


Figure 4-44. Comparison of the stress profiles in the middle cross-section of the samples with constant density (left) and evolving density (right) at  $t=100$  s.

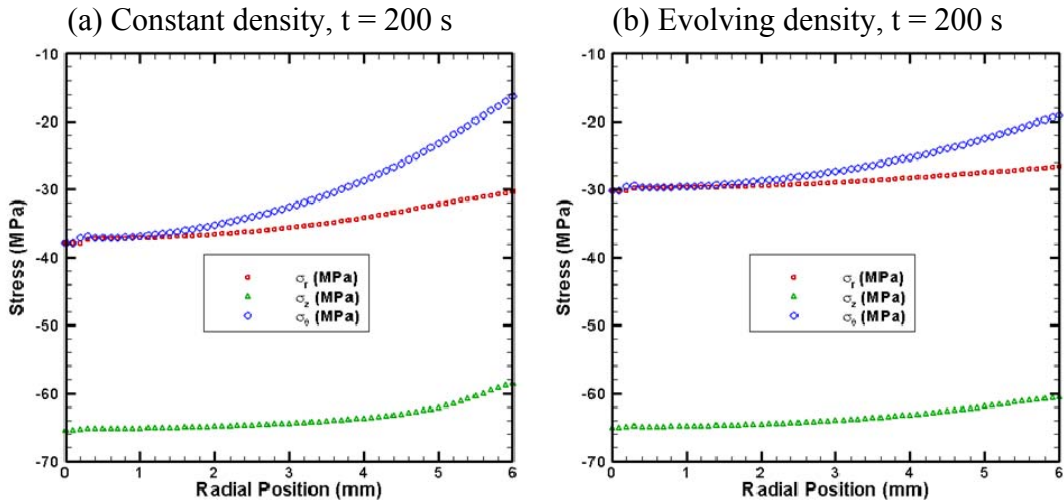


Figure 4-45. Comparison of the stress profiles in the middle cross-section of the samples with constant density (left) and evolving density (right) at  $t=200$  s.

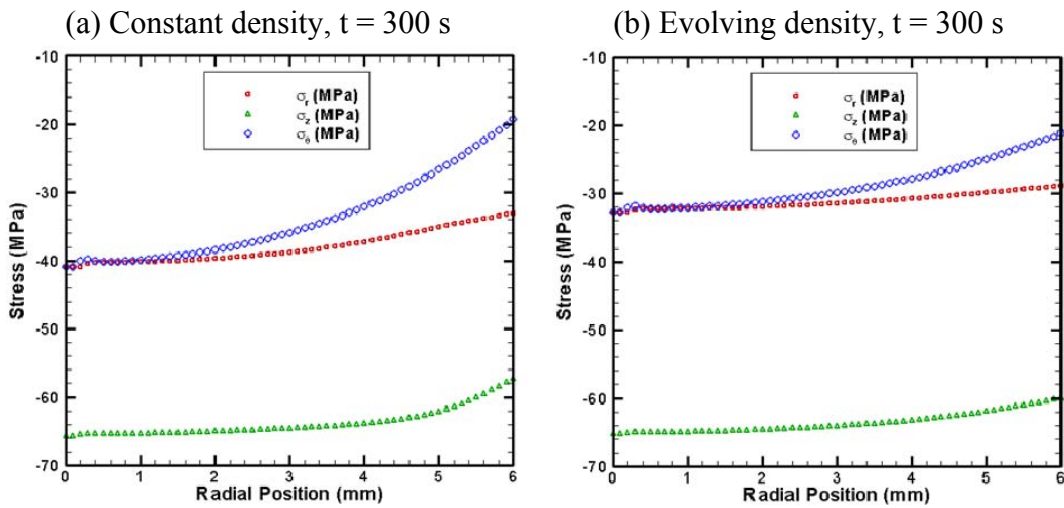


Figure 4-46. Comparison of the stress profiles in the middle cross-section of the samples with constant density (left) and evolving density (right) at  $t=300$  s.

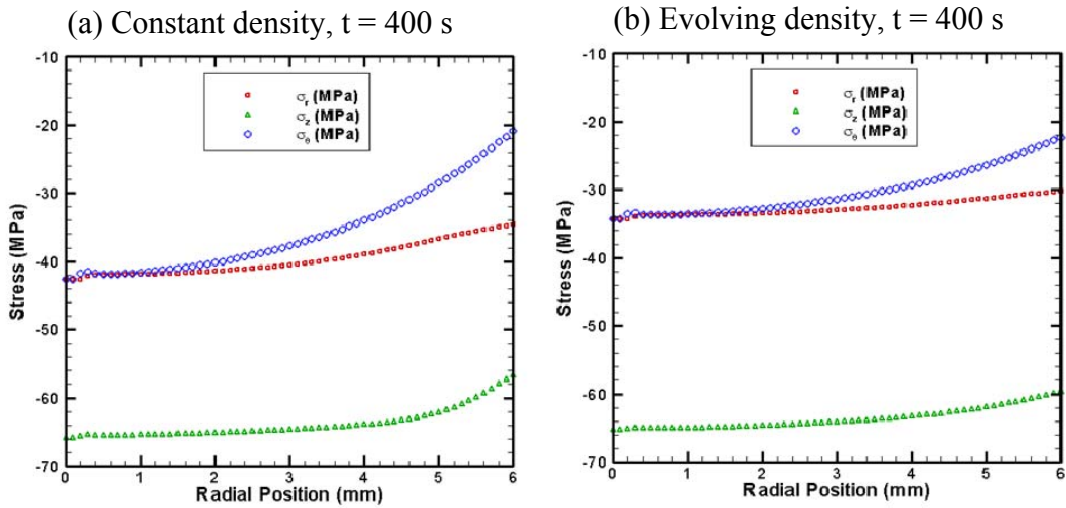


Figure 4-47. Comparison of the stress profiles in the middle cross-section of the samples with constant density (left) and evolving density (right) at  $t=400$  s.

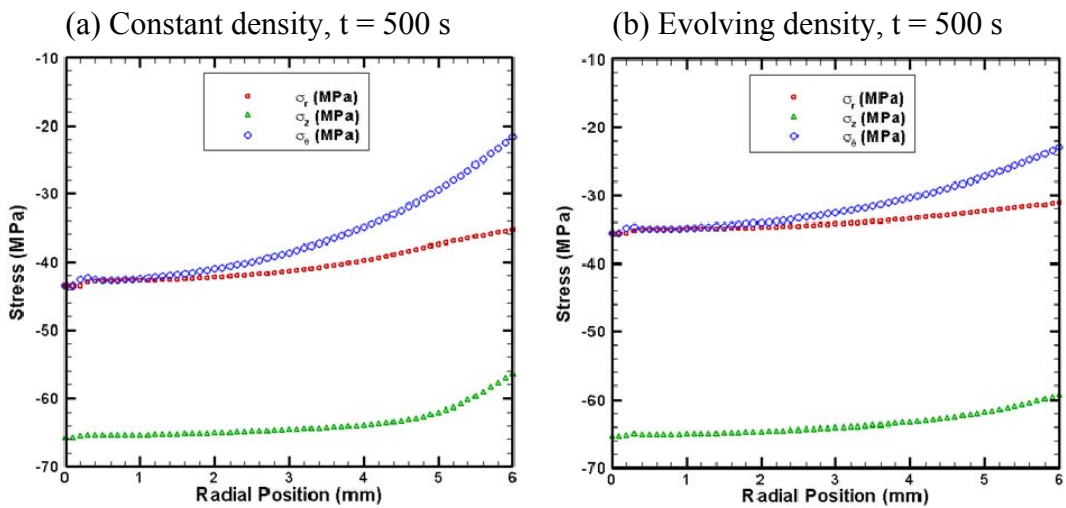


Figure 4-48. Comparison of the stress profiles in the middle cross-section of the samples with constant density (left) and evolving density (right) at  $t=500$  s.

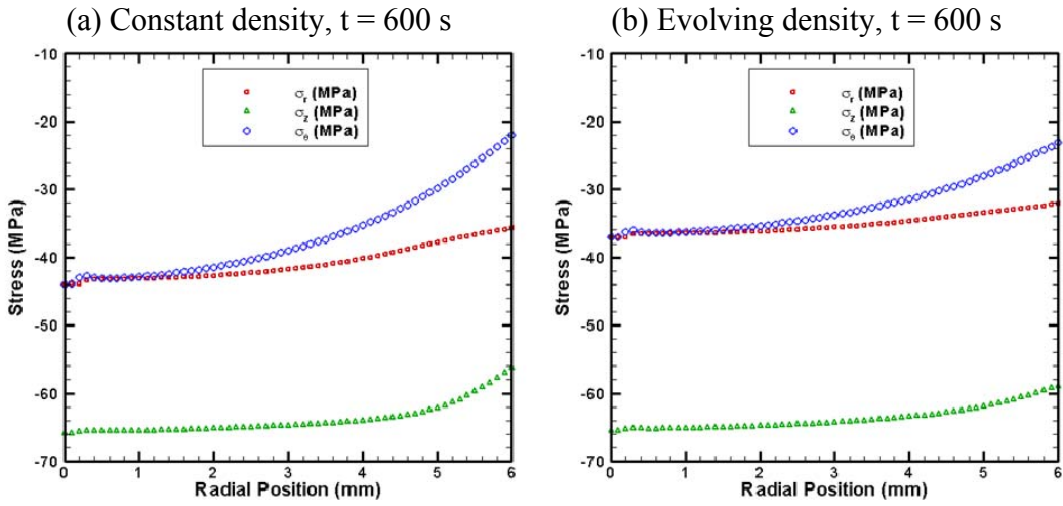


Figure 4-49. Comparison of the stress profiles in the middle cross-section of the samples with constant density (left) and evolving density (right) at  $t=600$  s.

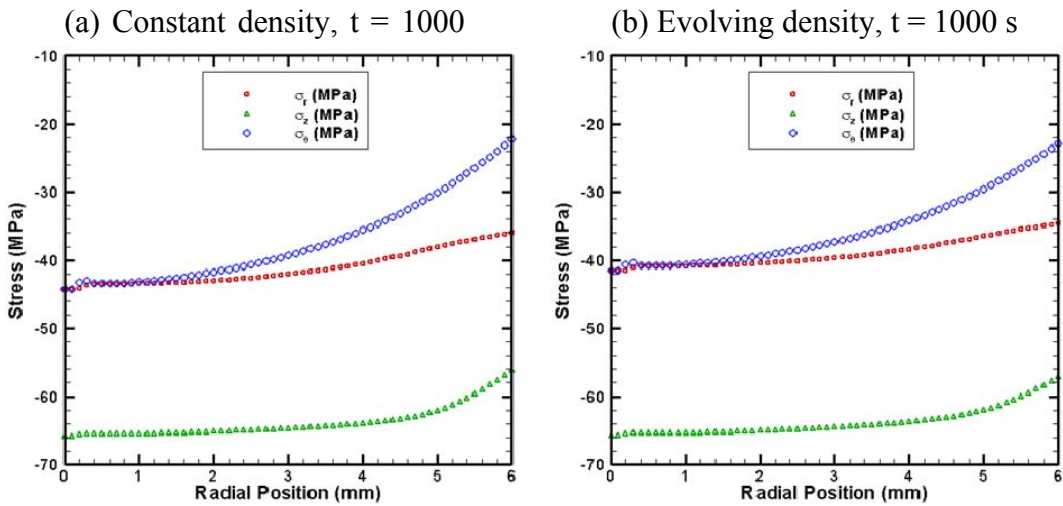


Figure 4-50. Comparison of the stress profiles in the middle cross-section of the samples with constant density (left) and evolving density (right) at  $t=1000$  s.

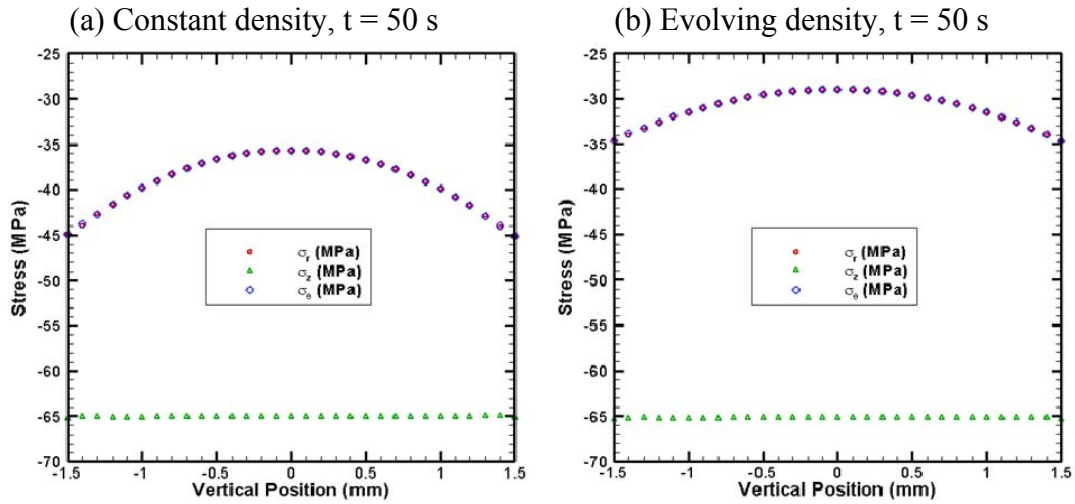


Figure 4-51. Comparison of the stress profiles along the axis of symmetry in the samples with constant density (left) and evolving density (right) at  $t=50$  s.

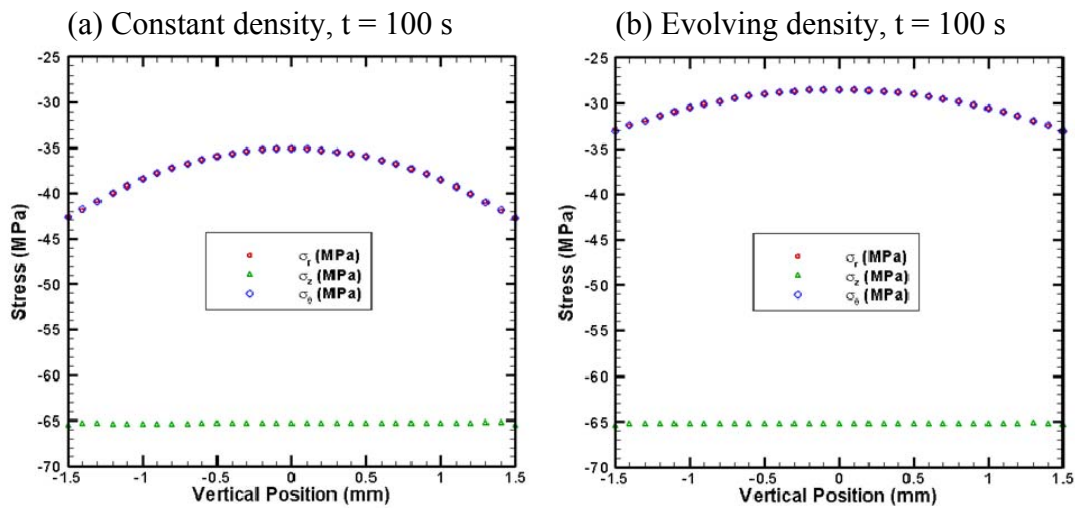


Figure 4-52. Comparison of the stress profiles along the axis of symmetry in the samples with constant density (left) and evolving density (right) at  $t=100$  s.

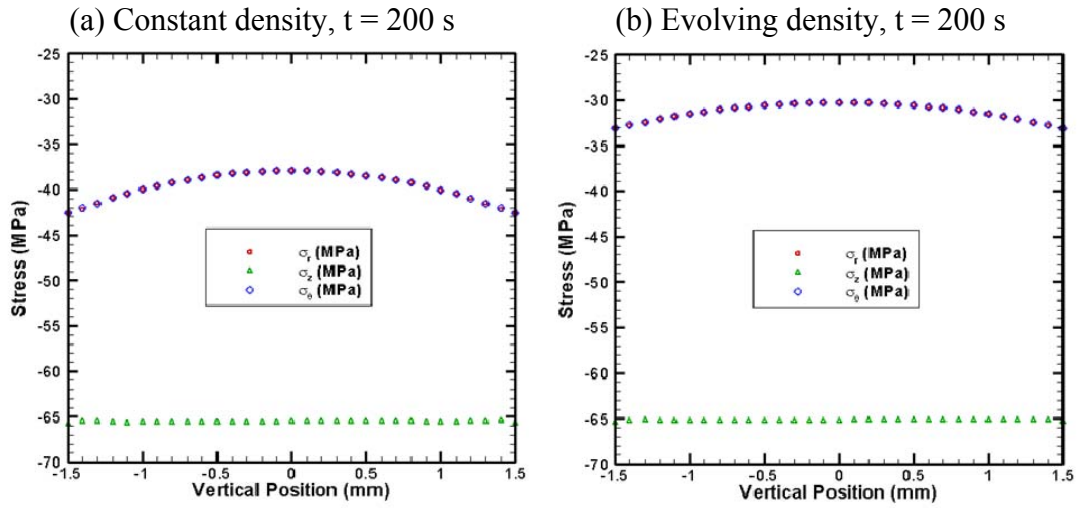


Figure 4-53. Comparison of the stress profiles along the axis of symmetry in the samples with constant density (left) and evolving density (right) at  $t=200$  s.

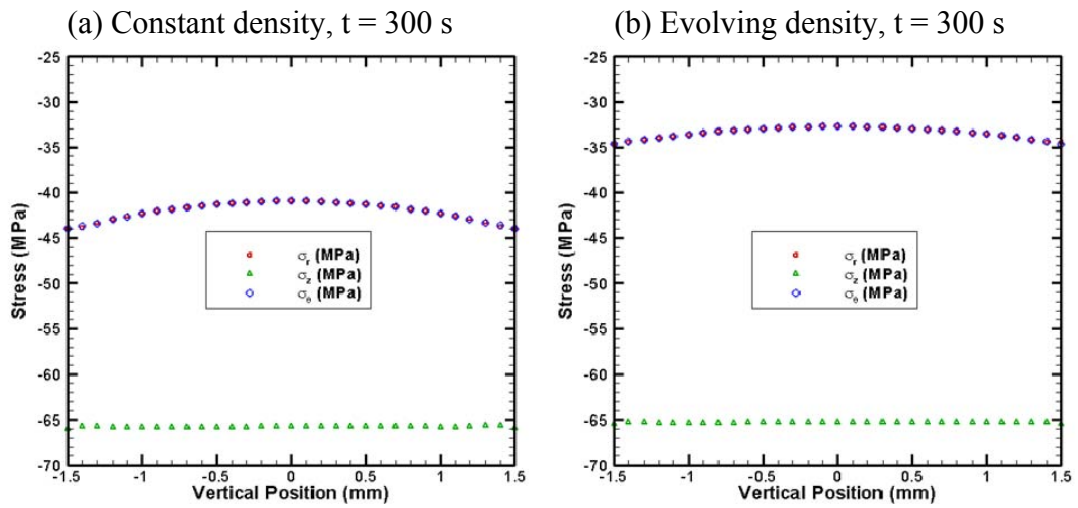


Figure 4-54. Comparison of the stress profiles along the axis of symmetry in the samples with constant density (left) and evolving density (right) at  $t=300$  s.

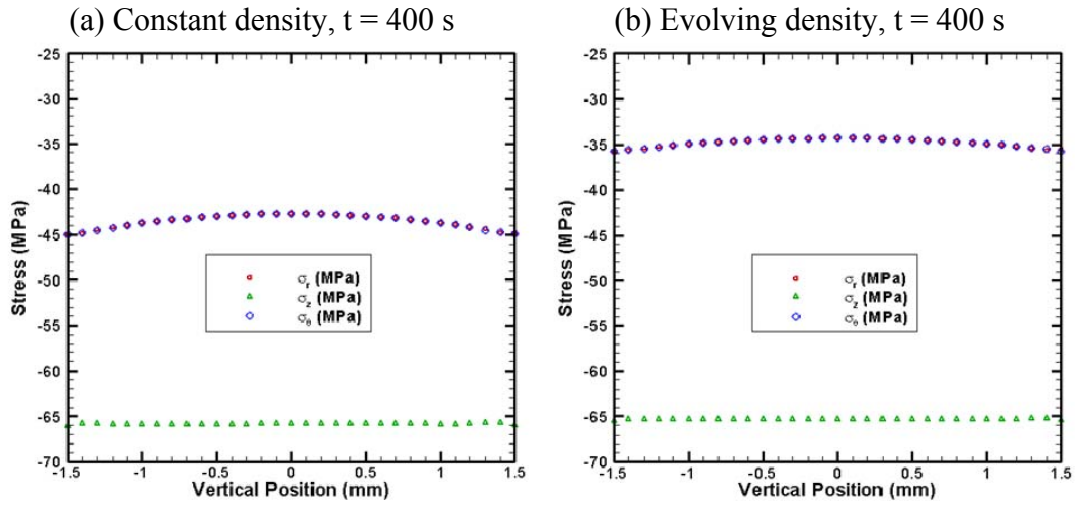


Figure 4-55. Comparison of the stress profiles along the axis of symmetry in the samples with constant density (left) and evolving density (right) at  $t=400$  s.

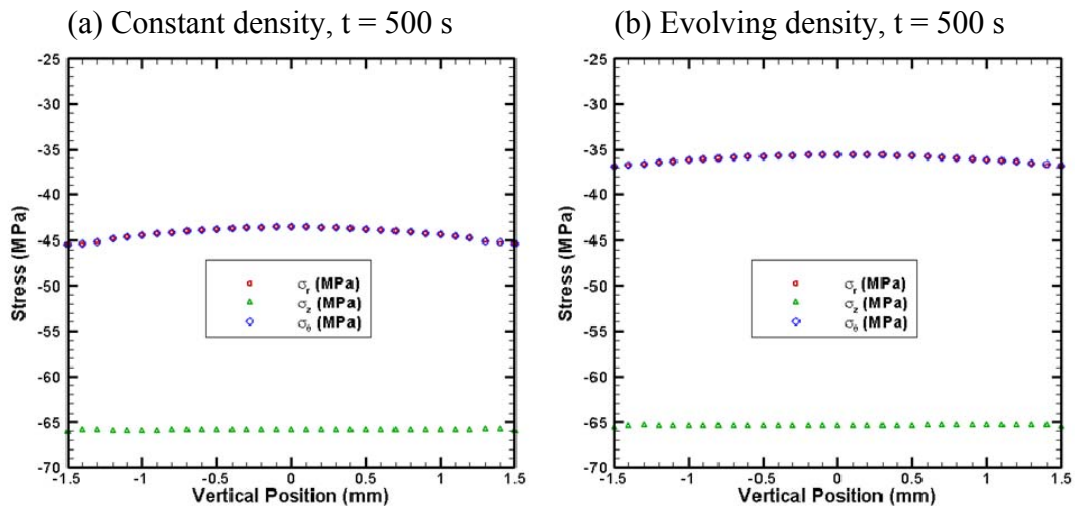


Figure 4-56. Comparison of the stress profiles along the axis of symmetry in the samples with constant density (left) and evolving density (right) at  $t=500$  s.

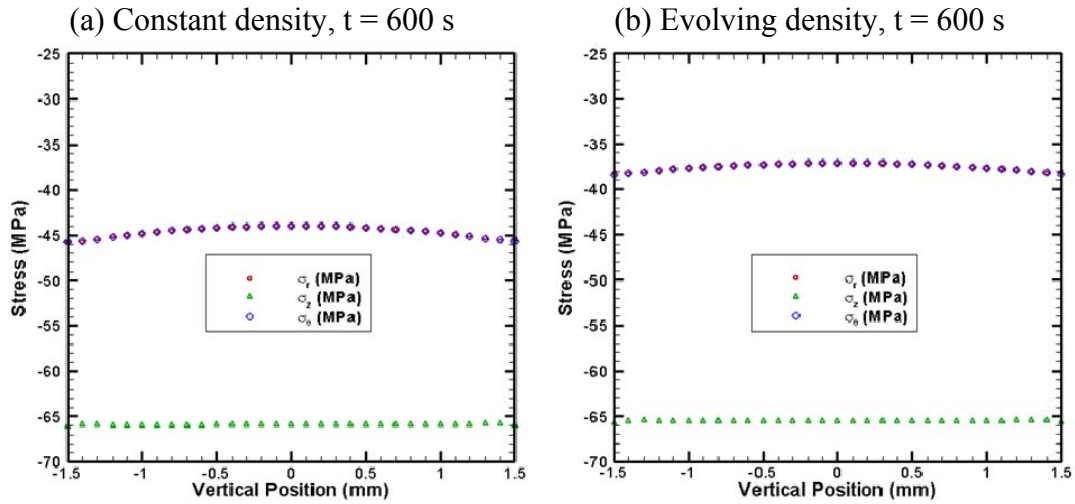


Figure 4-57. Comparison of the stress profiles along the axis of symmetry in the samples with constant density (left) and evolving density (right) at  $t=600$  s.

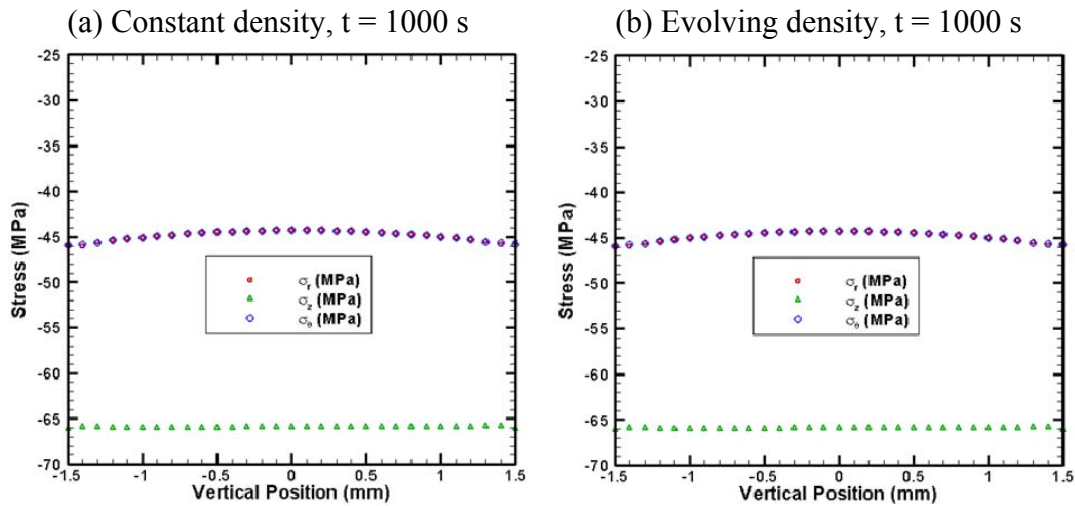


Figure 4-58. Comparison of the stress profiles along the axis of symmetry in the samples with constant density (left) and evolving density (right) at  $t=1000$  s.

#### 4.4 Conclusions

An integrated experimental/numerical methodology was developed in this chapter, and the densification effect of the powder compact during the SPS process was investigated by taking into consideration of the temperature-density dependent properties of the sintering material. A case study was presented, and the comparison between the results corresponding to the constant and evolving densities cases revealed the influence of density change on the temperature and stress distributions.

The simulation results showed that the magnitude of the temperature in the evolving density case is higher than that of constant density before the temperature reaches steady state, and larger temperature gradients exist in the case with evolving density. However, when the temperature of the system reaches steady state, the temperature profiles of the two cases are almost the same. This is due to the density dependence of thermal conductivity of the porous powder compact; before becoming fully condensed, the thermal conductivity of the sample is lower than that of the fully dense material, which leads to more local heating effect and subsequently higher temperature gradients.

In addition, as the Young's modulus and the Poisson's ratio change with density in the evolving density case while their values are still less than those of the fully dense material, reduced Poisson-type expansion occurs during the sintering process, leading to lower magnitudes of the radial and hoop stresses. Moreover, less stress gradients exist in the sample with evolving density; the stress gradients decrease with the increment of sintering time until approximating 300 s to 500 s, and then begin to increase. This

phenomenon indicates that for the parameters used in this study, there must exist a critical moment during the sintering process at which the most uniform stress distributions can be expected.

## **Chapter 5**

### **Conclusions and Future Work**

#### **5.1 Conclusions**

A finite element model capable of simulating the three-way coupling of thermal, electrical, and mechanical behavior of the SPS process was developed using ANSYS software in order to gain an insight into the cause of potential temperature and stress heterogeneities. Based on the model, the influences of different materials and sample aspect ratios on the temperature and stress distributions were systematically investigated.

The simulation results indicated that both thermal conductivity/diffusivity and electrical conductivity had important roles in establishing the temperature gradients throughout the whole SPS system, especially in the sample region. Relatively low temperature corresponded to the electrically conductive samples while higher temperature gradients were observed in the samples with low thermal conductivities. Sample aspect ratios did influence the magnitude and severity of the temperature, namely the temperature and corresponding gradients are directly proportional to the aspect ratios. With increasing aspect ratios, the temperature gradients in the sample region became more severe, especially in the vertical direction. The temperature gradients and applied pressure in turn, affected the magnitudes and distributions of the stresses that help govern final densification. It was found that the stress gradients are much higher than the temperature counterparts. Moreover, the mechanical properties (coefficient of thermal

expansion, Poisson's ratio, and Young's modulus) of the sample also exerted a significant influence on the stress distributions. Comparatively large magnitudes of the radial and hoop stresses, which exceed the axial components, were observed in samples with higher coefficients of thermal expansion. Hence, the electrical, thermal, and mechanical properties, as well as sample size and aspect ratio, all played an important role in determining the sample temperature and the corresponding uniformity.

In addition, an integrated experimental/numerical methodology was also developed, and the densification effect of the powder compact during the SPS process was investigated by taking into consideration of the temperature-density dependent properties of the sintering material. The simulation results revealed that the temperature and stress distributions were closely related to the instantaneous density of the powder compact. At lower density, more local heating and subsequently higher temperature gradients could be expected in the sample region as the thermal conductivity is relatively low. However, less Poisson-type expansion occurred during the sintering process, which subsequently led to lower magnitudes of the radial and hoop stresses. Furthermore, it is also worth noting that, for the given parameters, there exists a critical moment during the sintering process at which the most uniform stress distributions can be obtained.

## **5.2 Future Work**

According to the three-way coupling finite element model developed in this study, the thermal and electrical contact resistances, which have been intensively investigated by Zhang [41], Zavaliangos et al. [42], Cincotti et al. [46], Maizza et al. [47, 48], and

McWilliams [54], was not considered, even though they were thought to have a dramatic effect on the current and temperature distributions within the SPS system. Therefore, it is strongly recommended that further study should incorporate both thermal and electrical contact resistances into the model by constructing a function which can relate the resistances to temperature, externally applied load, and instantaneous density of the powder compact.

In addition, the systematic investigation of the influences of material properties and sample aspect ratios on the temperature and stress distributions was only conducted at the latter stage of the SPS sintering process without taking into account of the densification process and the ensuing changes to thermal, electrical, and mechanical properties. Thus, future studies of the temperature and stress distributions during the entire SPS process with different sample aspect ratios and evolving material properties that beyond the scope of this thesis should also be conducted.

Moreover, as the moving mesh technique [47, 48] is currently not available in ANSYS, the finite element mesh in the sample region was not be updated during the densification modeling. The volume of the powder compact was kept constant in the simulation, which is contrary to the experimental observations, and may lead to the discrepancies of the magnitudes and gradients of the temperature and subsequently the stresses. One conceivable solution could be the incorporation of ANSYS with other software, such as MATLAB. In each densification step, the temperature and displacement fields are calculated in ANSYS, and the results are exported to MATLAB for calculation to update of the mesh of the whole SPS system for the next iteration. Before moving into the next densification step, the updated mesh is imported into ANSYS. The nodal

temperatures of the last step and boundary conditions could then be applied to the corresponding nodes in the new mesh for the next multi-field calculation and the process is iterated. In order to simulate the whole densification process, an interface program should be developed so that the data passing between ANSYS and MATLAB can be conducted automatically.

While not modeled in this study, it is also feasible that the tailoring of the punch geometry, especially at the sample interface, has the potential to improve the final density of the samples undergoing SPS treatment. Therefore, additional studies that include the non-linear changes in properties during the SPS process, as well as potential changes to the punch/sample interface is strongly recommended in order to optimize the process for specific materials and different geometries.

## Bibliography

1. Grasso, S., Sakka, Y., and Maizza, G., *Electric current activated/assisted sintering (ECAS): A review of patents 1906-2008*. Science and Technology of Advanced Materials, 2009. **10**: p. 1-24.
2. Orru, R., Licheri, R., Locci, A.M., Cincotti, A., and Cao, G.C., *Consolidation/synthesis of materials by electric current activated/assisted sintering*. Materials Science & Engineering R, 2009. **63**(4-6): p. 127-287.
3. Munir, Z.A., Anselmi-Tamburini, U., and Ohyanagi, M., *The effect of electric field and pressure on the synthesis and consolidation of materials: A review of the spark plasma sintering method*. Journal of Materials Science, 2006. **41**(3): p. 763-777.
4. Gu, Y.W., Loh, N.H., Khor, K.A., Tor, S.B., and Cheang, P., *Spark plasma sintering of hydroxyapatite powders*. Biomaterials, 2002. **23**(1): p. 37-43.
5. Elissalde, C., Maglione, M., and Estournes, C., *Tailoring dielectric properties of multilayer composites using spark plasma sintering*. Journal of the American Ceramic Society, 2007. **90**(3): p. 973-976.
6. Jiang, D.T., Hulbert, D.M., Kuntz, J.D., Anselmi-Tamburini, U., and Mukherjee, A.K., *Spark plasma sintering: A high strain rate low temperature forming tool for ceramics*. Materials Science and Engineering A, 2007. **463**(1-2): p. 89-93.
7. Hulbert, D.M., Jiang, D.T., Anselmi-Tamburini, U., Unuvar, C., and Mukherjee, A.K., *Experiments and modeling of spark plasma sintered, functionally graded*

- boron carbide-aluminum composites*. Materials Science and Engineering A, 2008. **488**(1-2): p. 333-338.
8. Omori, M., *Sintering, consolidation, reaction and crystal growth by the spark plasma system (SPS)*. Materials Science and Engineering A, 2000. **287**(2): p. 183-188.
  9. Chaim, R., Levin, M., Shlayer, A., and Estournes, C., *Sintering and densification of nanocrystalline ceramic oxide powders: a review* Advances in Applied Ceramics, 2008. **107**(3): p. 159-169.
  10. Kar, S., Sarma, E.S., Somu, V.B., Kishore, N.K., and Srinivas, V., *Evaluation of different consolidation methods for nano-materials*. Indian Journal of Engineering and Materials Sciences, 2008. **15**(4): p. 343-346.
  11. Lu, K., *Sintering of nanoceramics*. International Materials Reviews, 2008. **53**(1): p. 21-38.
  12. Hungria, T., Galy, J., and Castro, A., *Spark Plasma Sintering as a Useful Technique to the Nanostructuring of Piezo-Ferroelectric Materials*. Advanced Engineering Materials, 2009. **11**(8): p. 615-631.
  13. Dobedoe, R.S., West, G.D., and Lewis, M.H., *Spark plasma sintering of ceramics: understanding temperature distribution enables more realistic comparison with conventional processing*. Advances in Applied Ceramics, 2005. **104**(3): p. 110-116.
  14. Hulbert, D.M., Anders, A., Dudina, D.V., Andersson, J., Jiang, D., Unuvar, C., Anselmi-Tamburini, U., Lavernia, E.J., and Mukherjee, A.K., *The absence of plasma in "spark plasma sintering"*. Journal of Applied Physics, 2008. **104**(3).

15. Hulbert, D.M., Anders, A., Andersson, J., Lavernia, E.J., and Mukherjee, A.K., *A discussion on the absence of plasma in spark plasma sintering*. Scripta Materialia, 2009. **60**(10): p. 835-838.
16. Taylor, G.F., *Apparatus for making hard metal compositions*. 1933, GEN ELECTRIC: United States.
17. Inoue, K., *Electric discharge heat treatment of metals in electrolytes*. 1965, Kiyoshi, Inoue: United States.
18. Inoue, K., *Electric-discharge sintering*. 1966, Kiyoshi, Inoue: United States.
19. Anselmi-Tamburini, U., Garay, J.E., Munir, Z.A., Tacca, A., Maglia, F., and Spinolo, G., *Spark plasma sintering and characterization of bulk nanostructured fully stabilized zirconia: Part I. Densification studies*. Journal of Materials Research, 2004. **19**(11): p. 3255-3262.
20. Kang, S.L., *Sintering: Densification, grain growth and microstructure*. 2005, Oxford: Elsevier.
21. Anselmi-Tamburini, U., Garay, J.E., and Munir, Z.A., *Fast low-temperature consolidation of bulk nanometric ceramic materials*. Scripta Materialia, 2006. **54**(5): p. 823-828.
22. Grasso, S., Sakka, Y., Maizza, G., and Hu, C.F., *Pressure effect on the homogeneity of spark plasma-sintered tungsten carbide powder*. Journal of the American Ceramic Society, 2009. **92**(10): p. 2418-2421.
23. Salarnon, D. and Shen, Z.J., *Pressure-less spark plasma sintering of alumina*. Materials Science and Engineering A, 2008. **475**(1-2): p. 105-107.

24. Zhou, Y., Hirao, K., Yamauchi, Y., and Kanzaki, S., *Densification and grain growth in pulse electric current sintering of alumina*. Journal of the European Ceramic Society, 2004. **24**(12): p. 3465-3470.
25. Chen, D.J. and Mayo, M.J., *Rapid rate sintering of nanocrystalline ZrO<sub>2</sub>-3mol% Y<sub>2</sub>O<sub>3</sub>*. Journal of the American Ceramic Society, 1996. **79**(4): p. 906-912.
26. Wang, S.W., Chen, L.D., Hirai, T., and Kang, Y.S., *Microstructure inhomogeneity in Al<sub>2</sub>O<sub>3</sub> sintered bodies formed during the plasma-activated sintering process*. Journal of Materials Science Letters, 1999. **18**(14): p. 1119-1121.
27. Wang, Y.C., Fu, Z.Y., Wang, W.M., and Zhu, H.X., *Temperature field distribution in spark plasma sintering of BN*. Journal of Wuhan University of Technology-Materials Science Edition, 2002. **17**(2): p. 19-21.
28. Wang, Y.C., Fu, Z.Y., and Zhang, Q.J., *SPS temperature distribution of different conductivity materials*, in *High-Performance Ceramics 2001, Proceedings*, J. Gong and W. Pan, Editors. 2002, Trans Tech Publications Ltd: Zurich-Uetikon. p. 717-720.
29. Zhang, D.M., Zhang, L.M., Guo, J.K., and Tuan, W.H., *Direct evidence of temperature variation within ceramic powder compact during pulse electric current sintering*. Journal of the American Ceramic Society, 2006. **89**(2): p. 680-683.
30. Xie, G.Q., Ohashi, O., Chiba, K., Yamaguchi, N., Song, M.H., Furuya, K., and Noda, T., *Frequency effect on pulse electric current sintering process of pure*

- aluminum powder*. Materials Science and Engineering A, 2003. **359**(1-2): p. 384-390.
31. Conrad, H., *Thermally activated plastic flow of metals and ceramics with an electric field or current*. Materials Science and Engineering A, 2002. **322**(1-2): p. 100-107.
32. Chen, W., Anselmi-Tamburini, U., Garay, J.E., Groza, J.R., and Munir, Z.A., *Fundamental investigations on the spark plasma sintering/synthesis process - I. Effect of dc pulsing on reactivity*. Materials Science and Engineering A, 2005. **394**(1-2): p. 132-138.
33. Anselmi-Tamburini, U., Garay, J.E., and Munir, Z.A., *Fundamental investigations on the spark plasma sintering/synthesis process III. Current effect on reactivity*. Materials Science and Engineering A, 2005. **407**(1-2): p. 24-30.
34. Anderson, K.R., Groza, J.R., Fendorf, M., and Echer, C.J., *Surface oxide debonding in field assisted powder sintering*. Materials Science and Engineering A, 1999. **270**(2): p. 278-282.
35. Groza, J.R. and Zavaliangos, A., *Sintering activation by external electrical field*. Materials Science and Engineering A, 2000. **287**(2): p. 171-177.
36. Shen, Z.J., Johnsson, M., Zhao, Z., and Nygren, M., *Spark plasma sintering of alumina*. Journal of the American Ceramic Society, 2002. **85**(8): p. 1921-1927.
37. Wang, Y.C. and Fu, Z.Y., *Study of temperature field in spark plasma sintering*. Materials Science and Engineering B, 2002. **90**(1-2): p. 34-37.
38. Matsugi, K., Kuramoto, H., Hatayama, T., and Yanagisawa, O., *Temperature distribution at steady state under constant current discharge in spark sintering*

- process of Ti and Al<sub>2</sub>O<sub>3</sub> powders*. Journal of Materials Processing Technology, 2003. **134**(2): p. 225-232.
39. Matsugi, K., Kuramoto, H., Yanagisawa, O., and Kiritani, M., *A case study for production of perfectly sintered complex compacts in rapid consolidation by spark sintering*. Materials Science and Engineering A, 2003. **354**(1-2): p. 234-242.
40. Wang, Y.C., Fu, Z.Y., and Wang, W.M., *Numerical simulation of the temperature field in sintering of BN by SPS*, in *Composite Materials Iii*, L. Zhang, J.K. Guo, and W.H. Tuan, Editors. 2003, Trans Tech Publications Ltd: Zurich-Uetikon. p. 471-476.
41. Zhang, J., *Numerical simulation of thermoelectric phenomena in field activated sintering*, in *Department of Materials Science and Engineering*. 2004, Drexel University.
42. Zavaliangos, A., Zhang, J., Krammer, M., and Groza, J.R., *Temperature evolution during field activated sintering*. Materials Science and Engineering A, 2004. **379**(1-2): p. 218-228.
43. Anselmi-Tamburini, U., Gennari, S., Garay, J.E., and Munir, Z.A., *Fundamental investigations on the spark plasma sintering/synthesis process - II. Modeling of current and temperature distributions*. Materials Science and Engineering A, 2005. **394**(1-2): p. 139-148.
44. Vanmeensel, K., Laptev, A., Hennicke, J., Vleugels, J., and Van der Biest, O., *Modelling of the temperature distribution during field assisted sintering*. Acta Materialia, 2005. **53**(16): p. 4379-4388.

45. McWilliams, B., Zavaliangos, A., Cho, K.C., and Dowding, R.J., *The modeling of electric-current-assisted sintering to produce bulk nanocrystalline tungsten*. Jom, 2006. **58**(4): p. 67-71.
46. Cincotti, A., Locci, A.M., Orru, R., and Cao, G., *Modeling of SPS apparatus: Temperature, current and strain distribution with no powders*. AIChE Journal, 2007. **53**(3): p. 703-719.
47. Maizza, G., Grasso, S., Sakka, Y., Noda, T., and Ohashi, O., *Relation between microstructure, properties and spark plasma sintering (SPS) parameters of pure ultrafine WC powder*. Science and Technology of Advanced Materials, 2007. **8**(7-8): p. 644-654.
48. Maizza, G., Grasso, S., and Sakka, Y., *Moving finite-element mesh model for aiding spark plasma sintering in current control mode of pure ultrafine WC powder*. Journal of Materials Science, 2009. **44**(5): p. 1219-1236.
49. Rathel, J., Herrmann, M., and Beckert, W., *Temperature distribution for electrically conductive and non-conductive materials during Field Assisted Sintering (FAST)*. Journal of the European Ceramic Society, 2009. **29**(8): p. 1419-1425.
50. Tiwari, D., Basu, B., and Biswas, K., *Simulation of thermal and electric field evolution during spark plasma sintering*. Ceramics International, 2009. **35**(2): p. 699-708.
51. Wang, X., Casolco, S.R., Xu, G., and Garay, J.E., *Finite element modeling of electric current-activated sintering: The effect of coupled electrical potential, temperature and stress*. Acta Materialia, 2007. **55**(10): p. 3611-3622.

52. Antou, G., Mathieu, G., Troliard, G., and Maitre, A., *Spark plasma sintering of zirconium carbide and oxycarbide: Finite element modeling of current density, temperature, and stress distributions*. Journal of Materials Research, 2009. **24**(2): p. 404-412.
53. McWilliams, B. and Zavaliangos, A., *Multi-phenomena simulation of electric field assisted sintering*. Journal of Materials Science, 2008. **43**(14): p. 5031-5035.
54. McWilliams, B.A., *Numerical simulation of electric field assisted sintering*, in *Department of Materials Science and Engineering*. 2008, Drexel University.
55. Kim, H.G., Gillia, O., Doremus, P., and Bouvard, D., *Near net shape processing of a sintered alumina component: adjustment of pressing parameters through finite element simulation*. International Journal of Mechanical Sciences, 2002. **44**(12): p. 2523-2539.
56. Loeb, A.L., *Thermal Conductivity: VIII, A Theory of Thermal Conductivity of Porous Materials*. Journal of the American Ceramic Society, 1954. **37**(2): p. 96-99.
57. Asmani, M., Kermel, C., Leriche, A., and Ourak, M., *Influence of porosity on Young's modulus and Poisson's ratio in alumina ceramics*. Journal of the European Ceramic Society, 2001. **21**(8): p. 1081-1086.
58. Montes, J.M., Rodriguez, J.A., and Herrera, E.J., *Thermal and electrical conductivities of sintered powder compacts*. Powder Metallurgy, 2003. **46**(3): p. 251-256.
59. Pabst, W., *Simple second-order expression: For the porosity dependence of thermal conductivity*. Journal of Materials Science, 2005. **40**(9-10): p. 2667-2669.

60. Pabst, W., Gregorova, E., and Ticha, G., *Elasticity of porous ceramics - A critical study of modulus-porosity relations*. Journal of the European Ceramic Society, 2006. **26**(7): p. 1085-1097.
61. Poulhier, C., Smith, D.S., and Absi, J., *Thermal conductivity of pressed powder compacts: tin oxide and alumina*. Journal of the European Ceramic Society, 2007. **27**(2-3): p. 475-478.
62. Pabst, W., Gregorova, E., and Ticha, G., *Effective properties of suspensions, composites and porous materials*. Journal of the European Ceramic Society, 2007. **27**(2-3): p. 479-482.
63. Zivcova, Z., Gregorova, E., Pabst, W., Smith, D.S., Michot, A., and Poulhier, C., *Thermal conductivity of porous alumina ceramics prepared using starch as a pore-forming agent*. Journal of the European Ceramic Society, 2009. **29**(3): p. 347-353.
64. Touloukian, Y.S., *Thermophysical properties of high temperature solid materials*. 1967, New York: Macmillan.
65. Inaba, H., *Semiempirical estimation of thermal expansion coefficients and isobaric heat capacities of fluorite-type compounds*. International Journal of Thermophysics, 2000. **21**(1): p. 249-268.
66. Kanchana, V., Vaitheeswaran, G., Svane, A., and Delin, A., *First-principles study of elastic properties of CeO<sub>2</sub>, ThO<sub>2</sub> and PoO<sub>2</sub>*. Journal of Physics-Condensed Matter, 2006. **18**(42): p. 9615-9624.

## Appendix A

### Material Properties

The temperature dependent properties of the fully dense materials were listed in Tables A-1 to A-5, where the properties of graphite, alumina and copper used in [43, 51] were adopted in this study for the purpose to compare with the published results. Other material properties were obtained from [64-66]. In the following tables,  $T$  is the temperature,  $\lambda$  is the thermal conductivity,  $\rho_e$  is the electrical resistivity,  $c_p$  is the specific heat capacity,  $\alpha$  the linear coefficient of thermal expansion,  $\rho$  is the density,  $E$  is the Young's modulus, and  $\nu$  is the Poisson's ratio.

Table A-1. Temperature dependent material properties of fully dense alumina.

$T$ ( $^{\circ}\text{C}$ )	$\lambda$ (W/m/K)	$\rho_e$ ( $\Omega$ m)	$c_p$ (J/kg/K)	$\alpha$ (1/K)	$\rho$ (kg/m $^3$ )	$E$ (GPa)	$\nu$
27	36.56	1.0e8	854.77	1.0e-8	3970	402.17	0.2337
50	33.07	1.0e8	883.42	1.0e-8	3970	402.17	0.2337
100	27.39	1.0e8	938.42	1.0e-8	3970	402.17	0.2337
150	23.37	1.0e8	985.31	1.0e-8	3970	402.17	0.2337
200	20.38	1.0e8	1025.76	1.0e-8	3970	402.17	0.2337
250	18.07	1.0e8	1061.02	1.0e-8	3970	402.17	0.2337
300	16.23	1.0e8	1092.05	1.0e-8	3970	402.17	0.2337
350	14.73	1.0e8	1119.56	1.0e-8	3970	402.17	0.2337
400	13.49	1.0e8	1144.13	1.0e-8	3970	402.17	0.2337
450	12.44	1.0e8	1166.22	1.0e-8	3970	402.17	0.2337
500	11.54	1.0e8	1186.18	1.0e-8	3970	402.17	0.2337
550	10.76	1.0e8	1204.32	1.0e-8	3970	402.17	0.2337
600	10.08	1.0e8	1220.88	1.0e-8	3970	402.17	0.2337
650	9.48	1.0e8	1236.06	1.0e-8	3970	402.17	0.2337
700	8.95	1.0e8	1250.03	1.0e-8	3970	402.17	0.2337
750	8.47	1.0e8	1262.93	1.0e-8	3970	402.17	0.2337
800	8.04	1.0e8	1274.89	1.0e-8	3970	402.17	0.2337
850	7.66	1.0e8	1286.01	1.0e-8	3970	402.17	0.2337
900	7.31	1.0e8	1296.37	1.0e-8	3970	402.17	0.2337
950	6.99	1.0e8	1306.06	1.0e-8	3970	402.17	0.2337
1000	6.69	1.0e8	1315.13	1.0e-8	3970	402.17	0.2337
1050	6.42	1.0e8	1323.66	1.0e-8	3970	402.17	0.2337
1100	6.18	1.0e8	1331.68	1.0e-8	3970	402.17	0.2337
1150	5.94	1.0e8	1339.25	1.0e-8	3970	402.17	0.2337
1200	5.73	1.0e8	1346.40	1.0e-8	3970	402.17	0.2337

Table A-2. Temperature dependent material properties of fully dense ceria.

$T$ ( $^{\circ}\text{C}$ )	$\lambda$ (W/m/K)	$\rho_e$ ( $\Omega$ m)	$c_p$ (J/kg/K)	$\alpha$ (1/K)	$\rho$ (kg/m $^3$ )	$E$ (GPa)	$\nu$
27	12.52	2.35e7	355.11	9.80e-6	7650	249.00	0.297
50	11.70	1.25e7	365.02	9.91e-6	7650	249.00	0.297
100	10.24	3.35e6	381.15	10.14e-6	7650	249.00	0.297
150	9.11	9.48e5	394.07	10.37e-6	7650	249.00	0.297
200	8.26	2.84e5	404.80	10.60e-6	7650	249.00	0.297
250	7.60	8.79e4	413.66	10.83e-6	7650	249.00	0.297
300	7.04	2.92e4	419.75	11.06e-6	7650	249.00	0.297
350	6.54	1.04e4	425.09	11.29e-6	7650	249.00	0.297
400	6.07	3.81e3	429.81	11.51e-6	7650	249.00	0.297
450	5.61	1.46e3	434.58	11.73e-6	7650	249.00	0.297
500	5.16	5.76e2	438.57	11.96e-6	7650	249.00	0.297
550	4.76	2.39e2	442.17	12.18e-6	7650	249.00	0.297
600	4.38	9.99e1	446.22	12.41e-6	7650	249.00	0.297
650	4.02	4.21e1	449.72	12.64e-6	7650	249.00	0.297
700	3.68	1.79e1	452.97	12.87e-6	7650	249.00	0.297
750	3.34	7.71e0	455.90	13.10e-6	7650	249.00	0.297
800	3.01	3.50e0	458.61	13.33e-6	7650	249.00	0.297
850	2.69	1.68e0	461.51	13.56e-6	7650	249.00	0.297
900	2.38	8.12e-1	464.63	13.79e-6	7650	249.00	0.297
950	2.08	4.14e-1	467.41	14.02e-6	7650	249.00	0.297
1000	1.78	2.14e-1	470.35	14.26e-6	7650	249.00	0.297
1050	1.51	1.10e-1	473.10	14.49e-6	7650	249.00	0.297
1100	1.29	5.94e-2	475.71	14.72e-6	7650	249.00	0.297
1150	1.13	3.27e-2	478.38	14.96e-6	7650	249.00	0.297
1200	1.01	1.84e-2	480.95	15.19e-6	7650	249.00	0.297

Table A-3. Temperature dependent material properties of fully dense copper.

$T$ ( $^{\circ}\text{C}$ )	$\lambda$ (W/m/K)	$\rho_e$ ( $\Omega$ m)	$c_p$ (J/kg/K)	$\alpha$ (1/K)	$\rho$ (kg/m $^3$ )	$E$ (GPa)	$\nu$
27	441.67	16.91e-9	385.32	16.5e-6	8940	120	0.34
50	443.28	17.78e-9	387.62	16.5e-6	8940	120	0.34
100	446.78	19.68e-9	392.62	16.5e-6	8940	120	0.34
150	450.28	21.58e-9	397.62	16.5e-6	8940	120	0.34
200	453.78	23.48e-9	402.62	16.5e-6	8940	120	0.34
250	457.28	25.38e-9	407.62	16.5e-6	8940	120	0.34
300	460.78	27.28e-9	412.62	16.5e-6	8940	120	0.34
350	464.28	29.18e-9	417.62	16.5e-6	8940	120	0.34
400	467.78	31.08e-9	422.62	16.5e-6	8940	120	0.34
450	471.28	32.98e-9	427.62	16.5e-6	8940	120	0.34
500	474.78	34.88e-9	432.62	16.5e-6	8940	120	0.34
550	478.28	36.78e-9	437.62	16.5e-6	8940	120	0.34
600	481.78	38.68e-9	442.62	16.5e-6	8940	120	0.34
650	485.28	40.58e-9	447.62	16.5e-6	8940	120	0.34
700	488.78	42.48e-9	452.62	16.5e-6	8940	120	0.34
750	492.28	44.38e-9	457.62	16.5e-6	8940	120	0.34
800	495.78	46.28e-9	462.62	16.5e-6	8940	120	0.34
850	499.28	48.18e-9	467.62	16.5e-6	8940	120	0.34
900	502.78	50.08e-9	472.62	16.5e-6	8940	120	0.34
950	506.28	51.98e-9	477.62	16.5e-6	8940	120	0.34
1000	509.78	53.88e-9	482.62	16.5e-6	8940	120	0.34
1050	513.28	55.78e-9	487.62	16.5e-6	8940	120	0.34

Table A-4. Temperature dependent material properties of fully dense tungsten.

$T$ ( $^{\circ}\text{C}$ )	$\lambda$ (W/m/K)	$\rho_e$ ( $\Omega$ m)	$c_p$ (J/kg/K)	$\alpha$ (1/K)	$\rho$ (kg/m $^3$ )	$E$ (GPa)	$\nu$
27	177.98	0.47e-7	132.23	4.5e-6	19250	411.00	0.28
50	173.78	0.52e-7	132.75	4.5e-6	19250	411.00	0.28
100	165.75	0.64e-7	133.87	4.5e-6	19250	411.00	0.28
150	158.76	0.76e-7	134.95	4.5e-6	19250	411.00	0.28
200	152.80	0.88e-7	136.01	4.5e-6	19250	411.00	0.28
250	147.64	1.01e-7	137.04	4.5e-6	19250	411.00	0.28
300	143.09	1.14e-7	138.05	4.5e-6	19250	411.00	0.28
350	139.10	1.29e-7	139.05	4.5e-6	19250	411.00	0.28
400	135.58	1.44e-7	140.02	4.5e-6	19250	411.00	0.28
450	132.46	1.57e-7	140.98	4.5e-6	19250	411.00	0.28
500	129.76	1.72e-7	141.93	4.5e-6	19250	411.00	0.28
550	127.48	1.87e-7	142.87	4.5e-6	19250	411.00	0.28
600	125.28	2.02e-7	143.81	4.5e-6	19250	411.00	0.28
650	123.29	2.18e-7	144.73	4.5e-6	19250	411.00	0.28
700	121.51	2.34e-7	145.64	4.5e-6	19250	411.00	0.28
750	119.93	2.49e-7	146.54	4.5e-6	19250	411.00	0.28
800	118.38	2.64e-7	147.43	4.5e-6	19250	411.00	0.28
850	116.85	2.80e-7	148.31	4.5e-6	19250	411.00	0.28
900	115.76	2.95e-7	149.20	4.5e-6	19250	411.00	0.28
950	114.59	3.11e-7	150.08	4.5e-6	19250	411.00	0.28
1000	113.45	3.26e-7	150.97	4.5e-6	19250	411.00	0.28
1050	112.40	3.42e-7	151.88	4.5e-6	19250	411.00	0.28
1100	111.42	3.57e-7	152.80	4.5e-6	19250	411.00	0.28
1150	110.39	3.73e-7	153.74	4.5e-6	19250	411.00	0.28
1200	109.42	3.89e-7	154.69	4.5e-6	19250	411.00	0.28

Table A-5. Temperature dependent material properties of fully dense graphite.

$T$ ( $^{\circ}\text{C}$ )	$\lambda$ (W/m/K)	$\rho_e$ ( $\Omega$ m)	$c_p$ (J/kg/K)	$\alpha$ (1/K)	$\rho$ (kg/m $^3$ )	$E$ (GPa)	$\nu$
27	59.90	18.63e-6	820.76	8.0e-6	1850	193.17	0.2383
50	59.51	18.19e-6	859.86	8.0e-6	1850	193.17	0.2383
100	58.66	17.27e-6	944.86	8.0e-6	1850	193.17	0.2383
150	57.81	16.43e-6	1029.86	8.0e-6	1850	193.17	0.2383
200	56.96	15.64e-6	1114.86	8.0e-6	1850	193.17	0.2383
250	56.11	14.92e-6	1199.86	8.0e-6	1850	193.17	0.2383
300	55.26	14.25e-6	1284.86	8.0e-6	1850	193.17	0.2383
350	54.41	13.64e-6	1369.86	8.0e-6	1850	193.17	0.2383
400	53.56	13.08e-6	1454.86	8.0e-6	1850	193.17	0.2383
450	52.71	12.56e-6	1539.86	8.0e-6	1850	193.17	0.2383
500	51.86	12.08e-6	1624.86	8.0e-6	1850	193.17	0.2383
550	51.01	11.65e-6	1709.86	8.0e-6	1850	193.17	0.2383
600	50.16	11.25e-6	1794.86	8.0e-6	1850	193.17	0.2383
650	49.31	10.88e-6	1879.86	8.0e-6	1850	193.17	0.2383
700	48.46	10.55e-6	1964.86	8.0e-6	1850	193.17	0.2383
750	47.61	10.24e-6	2049.86	8.0e-6	1850	193.17	0.2383
800	46.76	9.96e-6	2134.86	8.0e-6	1850	193.17	0.2383
850	45.91	9.71e-6	2219.86	8.0e-6	1850	193.17	0.2383
900	45.06	9.48e-6	2304.86	8.0e-6	1850	193.17	0.2383
950	44.21	9.26e-6	2389.86	8.0e-6	1850	193.17	0.2383
1000	43.36	9.07e-6	2474.86	8.0e-6	1850	193.17	0.2383
1050	42.51	8.89e-6	2559.86	8.0e-6	1850	193.17	0.2383
1100	41.66	8.72e-6	2644.86	8.0e-6	1850	193.17	0.2383
1150	40.81	8.56e-6	2729.86	8.0e-6	1850	193.17	0.2383
1200	39.96	8.42e-6	2814.86	8.0e-6	1850	193.17	0.2383

## Appendix B

### ANSYS Input Files

Following is the ANSYS APDL code developed to conduct the multi-field analysis, where the first part is for thermal-electric field analysis, and second for the stress field simulation. Material property input file for alumina is also attached.

```
! Thermal-electric field analysis
```

```
FINISH
```

```
/CLEAR
```

```
/PREP7
```

```
/TITLE, SPS SIMULATION
```

```
/UNITS, SI
```

```
! Input geometry information
```

```
sample_rad = 6.0e-3
```

```
! Radius of sample (m)
```

```
sample_height = 2.0e-3
```

```
! Half height of sample due to symmetry (m)
```

```
punch_rad = 6.0e-3
```

```
! Radius of Punch (m)
```

```
punch_height = 20e-3
```

```
! Height of Punch (m)
```

```
outer_die_thick = 16.25e-3
```

```
! Thickness of outer die (m)
```

```
outer_die_height = 15e-3
```

```
! Half height of outer die (m)
```

```
outer_die_felt_thick = 6.0e-3
```

```
! Thickness of outer die felt (m)
```

```
outer_die_felt_height = 15e-3
```

```
! Half height of outer die felt (m)
```

```
upper_punch_thick = 19.05e-3
```

```
! Radius of 1st part of upper punch (m)
```

```
upper_punch_height = 4.0e-3
```

```
! Height of 1st part of upper punch (m)
```

```
upper_punch_2_thick = 19.05e-3
```

```
! Radius of 2nd part of upper punch (m)
```

```
upper_punch_2_height = 5.0e-3
```

```
! Height of 2nd part of upper punch (m)
```

```
upper_punch_3_thick = 19.05e-3
```

```
! Radius of 3rd part of upper punch (m)
```

```
upper_punch_3_height = 6.0e-3
```

```
! Height of 3rd part of upper punch (m)
```

```
upper_punch_4_thick = 19.05e-3
```

```
! Radius of 4th part of upper punch (m)
```

```
upper_punch_4_height = 10.4e-3
```

```
! Height of 4th part of upper punch (m)
```

```
upper_punch_5_thick = 76.2e-3
```

```
! Radius of 1st part of spacer (m)
```

```
upper_punch_5_height = 8.0e-3
```

```
! Height of 1st part of spacer (m)
```

```

upper_punch_6_thick = 76.2e-3      ! Radius of 2nd part of spacer (m)
upper_punch_6_height = 17.4e-3    ! Height of 2nd part of spacer (m)

! Rename Variables and draw
sr = sample_rad
sh = sample_height
pr = punch_rad
ph = punch_height
odt = outer_die_thick
odh = outer_die_height
odft = outer_die_felt_thick
odfh = outer_die_felt_height
upt = upper_punch_thick
uph = upper_punch_height
up2t = upper_punch_2_thick
up2h = upper_punch_2_height
up3t = upper_punch_3_thick
up3h = upper_punch_3_height
up4t = upper_punch_4_thick
up4h = upper_punch_4_height
up5t = upper_punch_5_thick
up5h = upper_punch_5_height
up6t = upper_punch_6_thick
up6h = upper_punch_6_height

chamber_rad = 0.5      ! Radius of vacuum chamber
selem = 0.10e-3      ! Size of elements per area
emis1 = 1.0          ! Emissivity
bolt = 5.6704E-8     ! Stefan-Boltzmann radiation constant (W/m^2.K^4)
T0 = 300             ! Initial temperature (K)
mps = 800            ! Current (Amps)

! Read material properties from file matlib.mpl
MPREAD, 'matlib', 'mpl', ''

! Generate keypoints
K, 1, 0, 0
K, 2, sr, 0
K, 3, sr, sh
K, 4, 0, sh
K, 5, sr, -sh
K, 6, 0, -sh

```

K, 7, pr, sh  
K, 8, 0, sh  
K, 9, pr, sh+sh  
K, 10, 0, sh+sh  
K, 11, 0, sh+ph  
K, 12, pr, sh+ph  
K, 13, pr, odh  
K, 14, pr, -sh  
K, 15, 0, -sh  
K, 16, pr, -sh-sh  
K, 17, 0, -sh-sh  
K, 18, 0, -sh-ph  
K, 19, pr, -sh-ph  
K, 20, pr, -odh  
K, 21, sr, 0  
K, 22, sr+sr, 0  
K, 23, sr+odt, 0  
K, 24, sr, sh  
K, 25, sr, sh+sh  
K, 26, sr, odh  
K, 27, sr+sr, sh+sh  
K, 28, sr+sr, odh  
K, 29, sr+odt, odh  
K, 30, sr, -sh  
K, 31, sr, -sh-sh  
K, 32, sr, -odh  
K, 33, sr+sr, -sh-sh  
K, 34, sr+sr, -odh  
K, 35, sr+odt, -odh  
K, 36, sr+odt+odft, 0  
K, 37, sr+odt+odft, odfh  
K, 38, sr+odt+odft, -odfh  
K, 39, 0, sh+ph  
K, 40, pr, sh+ph  
K, 41, upt, sh+ph  
K, 42, upt, sh+ph+uph  
K, 43, 0, sh+ph+uph  
K, 44, 0, -sh-ph  
K, 45, 0, -sh-ph-uph  
K, 46, upt, -sh-ph-uph  
K, 47, upt, -sh-ph  
K, 48, pr, -sh-ph

K, 49, 0, sh+ph+uph+up2h  
 K, 50, up2t, sh+ph+uph+up2h  
 K, 51, 0, sh+ph+uph+up2h+up3h  
 K, 52, up3t, sh+ph+uph+up2h+up3h  
 K, 53, 0, sh+ph+uph+up2h+up3h+up4h  
 K, 54, up4t, sh+ph+uph+up2h+up3h+up4h  
 K, 55, up5t, sh+ph+uph+up2h+up3h+up4h  
 K, 56, 0, sh+ph+uph+up2h+up3h+up4h+up5h  
 K, 57, up4t, sh+ph+uph+up2h+up3h+up4h+up5h  
 K, 58, up5t, sh+ph+uph+up2h+up3h+up4h+up5h  
 K, 59, 0, sh+ph+uph+up2h+up3h+up4h+up5h+up6h  
 K, 60, up6t, sh+ph+uph+up2h+up3h+up4h+up5h+up6h  
 K, 61, 0, -sh-ph-uph-up2h  
 K, 62, up2t, -sh-ph-uph-up2h  
 K, 63, 0, -sh-ph-uph-up2h-up3h  
 K, 64, up3t, -sh-ph-uph-up2h-up3h  
 K, 65, 0, -sh-ph-uph-up2h-up3h-up4h  
 K, 66, up4t, -sh-ph-uph-up2h-up3h-up4h  
 K, 67, up5t, -sh-ph-uph-up2h-up3h-up4h  
 K, 68, 0, -sh-ph-uph-up2h-up3h-up4h-up5h  
 K, 69, up4t, -sh-ph-uph-up2h-up3h-up4h-up5h  
 K, 70, up5t, -sh-ph-uph-up2h-up3h-up4h-up5h  
 K, 71, 0, -sh-ph-uph-up2h-up3h-up4h-up5h-up6h  
 K, 72, up6t, -sh-ph-uph-up2h-up3h-up4h-up5h-up6h

! Generate areas

VSEL, NONE

CSYS, 0

A, 1, 2, 3, 4

ET, 1, PLANE67

A, 1, 6, 5, 2

ET, 1, PLANE67

ASEL, S, AREA, , 1, 2

AATT, 1, , 1, 0,

A, 8, 7, 9, 10

ET, 1, PLANE67

A, 17, 16, 14, 15

ET, 1, PLANE67

A, 10, 9, 13, 12, 11

ET, 1, PLANE67

A, 18, 19, 20, 16, 17  
ET, 1, PLANE67  
ASEL, S, AREA, , 3, 6  
AATT, 2, , 1, 0,

A, 21, 22, 27, 25, 24  
ET, 1, PLANE67  
A, 21, 30, 31, 33, 22  
ET, 1, PLANE67  
A, 25, 27, 28, 26  
ET, 1, PLANE67  
A, 31, 32, 34, 33  
ET, 1, PLANE67  
A, 22, 23, 29, 28, 27  
ET, 1, PLANE67  
A, 22, 33, 34, 35, 23  
ET, 1, PLANE67  
ASEL, S, AREA, , 7, 12  
AATT, 2, , 1, 0,

A, 23, 36, 37, 29  
ET, 1, PLANE67  
A, 23, 35, 38, 36  
ET, 1, PLANE67  
ASEL, S, AREA, , 13, 14  
AATT, 2, , 1, 0,

A, 39, 40, 41, 42, 43  
ET, 1, PLANE67  
A, 44, 45, 46, 47, 48  
ET, 1, PLANE67  
ASEL, S, AREA, , 15, 16  
AATT, 2, , 1, 0

A, 43, 42, 50, 49  
ET, 1, PLANE67  
A, 45, 61, 62, 46  
ET, 1, PLANE67  
ASEL, S, AREA, , 17, 18  
AATT, 2, , 1, 0,

A, 49, 50, 52, 51

ET, 1, PLANE67  
A, 61, 63, 64, 62  
ET, 1, PLANE67  
ASEL, S, AREA, , 19, 20  
AATT, 2, , 1, 0,

A, 51, 52, 54, 53  
ET, 1, PLANE67  
A, 63, 65, 66, 64  
ET, 1, PLANE67  
ASEL, S, AREA, , 21, 22  
AATT, 2, , 1, 0

A, 53, 54, 57, 56  
ET, 1, PLANE67  
A, 65, 68, 69, 66  
ET, 1, PLANE67  
A, 54, 55, 58, 57  
ET, 1, PLANE67  
A, 66, 69, 70, 67  
ET, 1, PLANE67  
ASEL, S, AREA, , 23, 26  
AATT, 2, , 1, 0

A, 56, 57, 58, 60, 59  
ET, 1, PLANE67  
A, 68, 71, 72, 70, 69  
ET, 1, PLANE67  
ASEL, S, AREA, , 27, 28  
AATT, 2, , 1, 0

KEYOPT, 1, 3, 1       ! Turn on axisymmetry option  
ASEL, ALL

! Glue areas  
AGLUE, 1, 2  
AGLUE, 3, 5  
AGLUE, 4, 6  
AGLUE, 7, 8, 9, 10, 11, 12, 13, 14  
AGLUE, 15, 17, 19, 21, 23, 25, 27  
AGLUE, 16, 18, 20, 22, 24, 26, 28

```
! Generate mesh
ASEL, ALL
ASEL, S, AREA, , 1, 4, 1, 0
ASEL, A, AREA, , 7, 8, 1, 0
AESIZE, ALL, selem

MSHAPE, 0, 2D
MSHKEY, 1
AMAP, 1, 1, 2, 3, 4
AMAP, 2, 1, 6, 5, 2
AMAP, 7, 21, 22, 27, 25
AMAP, 8, 21, 31, 33, 22
AMAP, 3, 8, 7, 9, 10
AMAP, 4, 15, 17, 16, 14

ASEL, S, AREA, , 5, 6, 1, 0
ASEL, A, AREA, , 9, 16, 1, 0
AESIZE, ALL, 2.0*selem
MSHKEY, 1
AMAP, 5, 10, 9, 12, 11
AMAP, 6, 18, 19, 16, 17
AMAP, 9, 25, 27, 28, 26
AMAP, 10, 32, 34, 33, 31
AMAP, 11, 22, 23, 29, 28
AMAP, 12, 34, 35, 23, 22
AMAP, 13, 23, 36, 37, 29
AMAP, 14, 35, 38, 36, 23
AMAP, 15, 39, 41, 42, 43
AMAP, 16, 45, 46, 47, 44

LSEL, S, LINE, , 60, 69, 3
LESIZE, ALL, , , 38
LSEL, S, LINE, , 65
LSEL, A, LINE, , 67, 68
LSEL, A, LINE, , 70
LESIZE, ALL, , , 6

ASEL, S, AREA, , 19, 20, 1, 0
MSHKEY, 0
AMESH, ALL

ASEL, S, AREA, , 21, 22, 1, 0
```

AESIZE, ALL, 9.0\*selem  
MSHKEY, 1  
AMAP, 21, 51, 52, 54, 53  
AMAP, 22, 65, 66, 64, 63

LSEL, S, LINE, , 77, 79, 2  
LSEL, A, LINE, , 80, 84, 2  
LSEL, A, LINE, , 87  
LESIZE, ALL, , , 5  
LSEL, S, LINE, , 78, 81, 3  
LESIZE, ALL, , , 8  
LSEL, S, LINE, , 83, 85, 2  
LSEL, A, LINE, , 86, 88, 2  
LESIZE, ALL, , , 26  
LSEL, S, LINE, , 89, 91, 2  
LSEL, A, LINE, , 92, 94, 2  
LESIZE, ALL, , , 7  
LSEL, S, LINE, , 90, 93, 3  
LESIZE, ALL, , , 34  
ALLSEL, ALL, ALL

MSHKEY, 1  
AMAP, 25, 54, 55, 58, 57  
AMAP, 26, 66, 69, 70, 67  
AMAP, 27, 56, 58, 60, 59  
AMAP, 28, 68, 71, 72, 70  
AMAP, 23, 53, 54, 57, 56  
AMAP, 24, 65, 68, 69, 66

LSEL, S, LINE, , 59, 61, 2  
LSEL, A, LINE, , 62, 64, 2  
LESIZE, ALL, , , 7  
ALLSEL, ALL, ALL

MSHKEY, 1  
ASEL, S, AREA, , 17, 18, 1, 0  
AMESH, ALL  
ASEL, ALL

! Define Contact Pairs  
ET, 2, 169  
ET, 3, 171

KEYOPT, 3, 1, 4	! Selects degrees of freedom: 0-UX, UY; 4-TEMP, VOLT
KEYOPT, 3, 2, 0	! Contact algorithm
KEYOPT, 3, 3, 0	! Stress state when superelements are present
KEYOPT, 3, 4, 0	! Location of contact detection point
KEYOPT, 3, 5, 0	! CNOF/ICONT Automated adjustment
KEYOPT, 3, 7, 1	! Element level time incrementation control
KEYOPT, 3, 8, 0	! Asymmetric contact selection
KEYOPT, 3, 9, 0	! Effect of initial penetration or gap
KEYOPT, 3, 10, 2	! Contact stiffness update
KEYOPT, 3, 11, 0	! Behavior of contact surface
KEYOPT, 3, 12, 0	! Contact stiffness variation

Tccecc = 1.0e10                   ! Thermal and electrical contact conductance

R, 1, , , 1.0, 0.1, 0,  
 RMORE, , , 1.0E20, 0, 1.0, 0  
 RMORE, 0.0, tccecc, 1.0, bolt, 1.0, 0.5  
 RMORE, tccecc, 1.0, 1.0, 0.0, , 1.0

R, 2, , , 1.0, 0.1, 0,  
 RMORE, , , 1.0E20, 0, 1.0, 0  
 RMORE, 0.0, tccecc, 1.0, bolt, 1.0, 0.5  
 RMORE, tccecc, 1.0, 1.0, 0.0, , 1.0

R, 3, , , 1.0, 0.1, 0,  
 RMORE, , , 1.0E20, 0, 1.0, 0  
 RMORE, 0.0, tccecc, 1.0, bolt, 1.0, 0.5  
 RMORE, tccecc, 1.0, 1.0, 0.0, , 1.0

R, 4, , , 1.0, 0.1, 0,  
 RMORE, , , 1.0E20, 0, 1.0, 0  
 RMORE, 0.0, tccecc, 1.0, bolt, 1.0, 0.5  
 RMORE, tccecc, 1.0, 1.0, 0.0, , 1.0

R, 5, , , 1.0, 0.1, 0,  
 RMORE, , , 1.0E20, 0, 1.0, 0  
 RMORE, 0.0, tccecc, 1.0, bolt, 1.0, 0.5  
 RMORE, tccecc, 1.0, 1.0, 0.0, , 1.0

R, 6, , , 1.0, 0.1, 0,  
 RMORE, , , 1.0E20, 0, 1.0, 0  
 RMORE, 0.0, tccecc, 1.0, bolt, 1.0, 0.5

RMORE, tccecc, 1.0, 1.0, 0.0, , 1.0

R, 7, , , 1.0, 0.1, 0,  
 RMORE, , , 1.0E20, 0, 1.0, 0  
 RMORE, 0.0, tccecc, 1.0, bolt, 1.0, 0.5  
 RMORE, tccecc, 1.0, 1.0, 0.0, , 1.0

! Contact Pair (1): contact between sample and upper punch

! Generate the target surface

LSEL, S, LINE, , 8

CM, \_TARGET, LINE

NSLL, S, 1

ESLN, S, 0

MP, MU, 2, 0

MP, EMIS, 2, 0

TYPE, 2

MAT, 2

REAL, 1

ESURF ! Generate TARGE169 elements

! Generate the contact surface

LSEL, S, LINE, , 3

CM, \_CONTACT, LINE

NSLL, S, 1

ESLN, S, 0

MP, MU, 1, 0

MP, EMIS, 1, 0

TYPE, 3

MAT, 1

REAL, 1

ESURF ! Generate CONTA171 elements

ALLSEL

CMDEL, \_TARGET

CMDEL, \_CONTACT

! Contact Pair (2): contact between sample and lower punch

! Generate the target surface

LSEL, S, LINE, , 14

CM, \_TARGET, LINE

NSLL, S, 1

ESLN, S, 0

MP, MU, 2, 0

MP, EMIS, 2, 0

```
TYPE, 2
MAT, 2
REAL, 2
ESURF          ! Generate TARGE169 elements
! Generate the contact surface
LSEL, S, LINE, , 6
CM, _CONTACT, LINE
NSLL, S, 1
ESLN, S, 0
MP, MU, 1, 0
MP, EMIS, 1, 0
TYPE, 3
MAT, 1
REAL, 2
ESURF          ! Generate CONTA171 elements
ALLSEL
CMDEL, _TARGET
CMDEL, _CONTACT

! Contact Pair (3): contact between sample and die
! Generate the target surface
LSEL, S, LINE, , 27
LSEL, A, LINE, , 28
LSEL, A, LINE, , 29
LSEL, A, LINE, , 30
CM, _TARGET, LINE
NSLL, S, 1
ESLN, S, 0
MP, MU, 2, 0
MP, EMIS, 2, 0
TYPE, 2
MAT, 2
REAL, 3
ESURF          ! Generate TARGE169 elements
! Generate the contact surface
LSEL, S, LINE, , 2
LSEL, A, LINE, , 7
CM, _CONTACT, LINE
NSLL, S, 1
ESLN, S, 0
MP, MU, 1, 0
MP, EMIS, 1, 0
```

```

TYPE, 3
MAT, 1
REAL, 3
ESURF          ! Generate CONTA171 elements
ALLSEL
CMDEL, _TARGET
CMDEL, _CONTACT

! Contact Pair (4): contact between die and upper punch
! Generate the target surface
LSEL, S, LINE, , 27
LSEL, A, LINE, , 28
LSEL, A, LINE, , 35
CM, _TARGET, LINE
NSLL, S, 1
ESLN, S, 0
MP, MU, 2, 0
MP, EMIS, 2, 0
TYPE, 2
MAT, 2
REAL, 4
ESURF          ! Generate TARGE169 elements
! Generate the contact surface
LSEL, S, LINE, , 9
LSEL, A, LINE, , 16
LSEL, A, LINE, , 17
CM, _CONTACT, LINE
NSLL, S, 1
ESLN, S, 0
MP, MU, 2, 0
MP, EMIS, 2, 0
TYPE, 3
MAT, 2
REAL, 4
ESURF          ! Generate CONTA171 elements
ALLSEL
CMDEL, _TARGET
CMDEL, _CONTACT

! Contact Pair (5): contact between die and lower punch
! Generate the target surface
LSEL, S, LINE, , 29

```

```
LSEL, A, LINE, , 30
LSEL, A, LINE, , 36
CM, _TARGET, LINE
NSLL, S, 1
ESLN, S, 0
MP, MU, 2, 0
MP, EMIS, 2, 0
TYPE, 2
MAT, 2
REAL, 5
ESURF                ! Generate TARGE169 elements
! Generate the contact surface
LSEL, S, LINE, , 13
LSEL, A, LINE, , 21
LSEL, A, LINE, , 22
CM, _CONTACT, LINE
NSLL, S, 1
ESLN, S, 0
MP, MU, 2, 0
MP, EMIS, 2, 0
TYPE, 3
MAT, 2
REAL, 5
ESURF                ! Generate CONTA171 elements
ALLSEL
CMDEL, _TARGET
CMDEL, _CONTACT

! Contact Pair (6): upper punch and spacer
! Generate the target surface
LSEL, S, LINE, , 49
LSEL, A, LINE, , 50
CM, _TARGET, LINE
NSLL, S, 1
ESLN, S, 0
MP, MU, 2, 0
MP, EMIS, 2, 0
TYPE, 2
MAT, 2
REAL, 6
ESURF                ! Generate TARGE169 elements
! Generate the contact surface
```

```

LSEL, S, LINE, , 18
CM, _CONTACT, LINE
NSLL, S, 1
ESLN, S, 0
MP, MU, 2, 0
MP, EMIS, 2, 0
TYPE, 3
MAT, 2
REAL, 6
ESURF                ! Generate CONTA171 elements
ALLSEL
CMDEL, _TARGET
CMDEL, _CONTACT

! Contact Pair (7): contact between lower punch and spacer
! Generate the target surface
LSEL, S, LINE, , 57
LSEL, A, LINE, , 58
CM, _TARGET, LINE
NSLL, S, 1
ESLN, S, 0
MP, MU, 2, 0
MP, EMIS, 2, 0
TYPE, 2
MAT, 2
REAL, 7
ESURF                ! Generate TARGE169 elements
! Generate the contact surface
LSEL, S, LINE, , 20
CM, _CONTACT, LINE
NSLL, S, 1
ESLN, S, 0
MP, MU, 2, 0
MP, EMIS, 2, 0
TYPE, 3
MAT, 2
REAL, 7
ESURF                ! Generate CONTA171 elements
ALLSEL
CMDEL, _TARGET
CMDEL, _CONTACT

```

ALLSEL, ALL, ALL

! Generate radiation element

ET, 12, SURF151  
 KEYOPT, 12, 3, 1  
 KEYOPT, 12, 4, 1  
 KEYOPT, 12, 5, 1  
 KEYOPT, 12, 9, 1  
 R, 12, 1, bolt  
 MP, EMIS, 4, emis1  
 TYPE, 12  
 MAT, 4  
 REAL, 12  
 N, 100000, chamber\_rad, 0  
 LSEL, S, LINE, , 45  
 LSEL, A, LINE, , 48  
 NSLL, S, 1  
 ESURF, 100000  
 ALLSEL, ALL, ALL  
 FINISH

! Solve the problem

/SOLU  
 ANTYPE, TRANS ! Transient analysis  
 TRNOPT, FULL  
 LUMPM, 0  
 TUNIF, T0 ! Set the initial temperature of the whole model  
 TREF, T0 ! Defines the reference temperature for the thermal strain calculations

D, 100000, TEMP, T0 ! Set the temperature of the chamber wall  
 NSEL, S, LOC, Y, -sh-ph-uph-up2h-up3h-up4h-up5h-up6h ! Select lower boundary  
 D, ALL, TEMP, T0 ! Hold temperature at T0  
 NSEL, S, LOC, Y, -sh-ph-uph-up2h-up3h-up4h-up5h-up6h  
 CP, 1, VOLT, ALL  
 n\_bott = ndnext(0)  
 D, n\_bott, VOLT, 0

NSEL, S, LOC, Y, sh+ph+uph+up2h+up3h+up4h+up5h+up6h ! Select upper bound  
 D, ALL, TEMP, T0 ! Hold temperature at T0  
 NSEL, S, LOC, Y, sh+ph+uph+up2h+up3h+up4h+up5h+up6h  
 CP, 2, VOLT, ALL  
 NSEL, S, LOC, Y, sh+ph+uph+up2h+up3h+up4h+up5h+up6h

```
n_top = ndnext(0)
F, n_top, AMPS, mps
ALLSEL, ALL, ALL
```

```
SOLCONTROL, ON
TIME, 1000
AUTOTS, ON
DELTIM, 0.00005
KBC, 1
TIMINT, ON
NSUBST, 8000
NEQIT, 100           ! Max no. of iterations
OUTRES, ALL, 1      ! Controls the solution data written to the database
STEF, bolt          ! Specifies Stefan-Boltzmann radiation constant
TOFFST, 0           ! Specifies the temperature offset from absolute zero to zero
! Defines a free-space ambient temperature for radiation using the radiosity method
SPCTEMP, 1, TO
V2DOPT, 1           ! Specifies 2-D/axisymmetric view factor calculation options
```

```
SOLVE
FINISH
```

```
! Stress field analysis
! Change element type
/PREP7
ETCHG, TTS
ESEL, S, ENAME, , SURF153
EDELE, ALL
ALLSEL, ALL
ETDEL, 12
KEYOPT, 1, 3, 1
KEYOPT, 3, 1, 0
FINISH
```

```
! Solve the problem
/SOL
ANTYPE, STATIC
NLGEOM, 1
NSUBST, 400, 500, 100
KBC, 0
OUTRES, ALL, 100
```

```

NSEL, S, LOC, Y, -sh-ph-uph-up2h-up3h-up4h-up5h-up6h ! Select lower bound
D, ALL, UY, 0
NSEL, S, LOC, Y, 0
NSEL, R, LOC, X, sr+odt+odft
D, ALL, UY, 0
NSEL, S, LOC, Y, sh+ph+uph+up2h+up3h+up4h+up5h+up6h ! Select upper bound
SF, ALL, PRES, 0.3947e6 ! Apply pressure
ALLSEL, ALL, ALL

LDREAD, TEMP, , , 1000, , , , ! Apply temperature field
ALLSEL, ALL, ALL

SOLVE
FINISH

```

```

! Material-property file for ANSYS
! File name: "matlib.mpl"

```

```

! Input material properties of Alumina
MPTEMP
MPTEMP, 1, 300, 302, 304, 306, 310, 315
MPTEMP, 7, 320, 324, 328, 332, 336, 340
MPTEMP, 13, 345, 350, 360, 370, 380, 390
MPTEMP, 19, 400, 410, 420, 430, 440, 450
MPTEMP, 25, 460, 470, 490, 500, 510, 520
MPTEMP, 31, 530, 540, 550, 560, 570, 580
MPTEMP, 37, 590, 600, 615, 630, 645, 660
MPTEMP, 43, 675, 690, 705, 720, 735, 750
MPTEMP, 49, 765, 780, 795, 810, 825, 840
MPTEMP, 55, 860, 880, 900, 920, 940, 960
MPTEMP, 61, 980, 1000, 1030, 1060, 1090, 1120
MPTEMP, 67, 1150, 1180, 1210, 1240, 1280, 1320
MPTEMP, 73, 1360, 1400, 1440, 1480, 1520, 1560
MPTEMP, 79, 1600, 1650, 1700, 1750, 1800, 1850
MPTEMP, 85, 1900, 1950, 2000, 2050, 2100, 2150
MPTEMP, 91, 2200, 2250, 2300, 2350, 2400, 2450
MPTEMP, 97, 2500

```

```

! Thermal Conductivity (W/(m.K))

```

MPDATA, KXX, 1, 1, 36.5550, 36.2228, 35.8966, 35.5763, 34.9524, 34.2027  
 MPDATA, KXX, 1, 7, 33.4844, 32.9312, 32.3959, 31.8778, 31.3760, 30.8897  
 MPDATA, KXX, 1, 13, 30.3027, 29.7375, 28.6682, 27.6731, 26.7448, 25.8767  
 MPDATA, KXX, 1, 19, 25.0632, 24.2993, 23.5806, 22.9032, 22.2636, 21.6588  
 MPDATA, KXX, 1, 25, 21.0860, 20.5427, 19.5359, 19.0687, 18.6232, 18.1981  
 MPDATA, KXX, 1, 31, 17.7920, 17.4036, 17.0318, 16.6756, 16.3340, 16.0060  
 MPDATA, KXX, 1, 37, 15.6910, 15.3882, 14.9552, 14.5459, 14.1584, 13.7910  
 MPDATA, KXX, 1, 43, 13.4423, 13.1107, 12.7951, 12.4943, 12.2073, 11.9333  
 MPDATA, KXX, 1, 49, 11.6712, 11.4204, 11.1802, 10.9499, 10.7289, 10.5166  
 MPDATA, KXX, 1, 55, 10.2463, 9.9895, 9.7453, 9.5127, 9.2910, 9.0794  
 MPDATA, KXX, 1, 61, 8.8772, 8.6838, 8.4091, 8.1511, 7.9086, 7.6800  
 MPDATA, KXX, 1, 67, 7.4643, 7.2604, 7.0673, 6.8842, 6.6544, 6.4394  
 MPDATA, KXX, 1, 73, 6.2379, 6.0486, 5.8705, 5.7025, 5.5439, 5.3939  
 MPDATA, KXX, 1, 79, 5.2518, 5.0843, 4.9272, 4.7795, 4.6404, 4.5092  
 MPDATA, KXX, 1, 85, 4.3852, 4.2678, 4.1566, 4.0510, 3.9506, 3.8551  
 MPDATA, KXX, 1, 91, 3.7641, 3.6773, 3.5944, 3.5152, 3.4394, 3.3667  
 MPDATA, KXX, 1, 97, 3.2971

! Specific heat (J/(Kg.K))

MPDATA, C, 1, 1, 854.7712, 857.3562, 859.9227, 862.4708, 867.5127, 873.7151  
 MPDATA, C, 1, 7, 879.8093, 884.6086, 889.3418, 894.0103, 898.6155, 903.1585  
 MPDATA, C, 1, 13, 908.7519, 914.2526, 924.9851, 935.3735, 945.4343, 955.1827  
 MPDATA, C, 1, 19, 964.6333, 973.7996, 982.6944, 991.3295, 999.7165, 1007.8658  
 MPDATA, C, 1, 25, 1015.7875, 1023.4912, 1038.2797, 1045.3811, 1052.2975, 1059.0362  
 MPDATA, C, 1, 31, 1065.6039, 1072.0073, 1078.2523, 1084.3451, 1090.2910, 1096.0954  
 MPDATA, C, 1, 37, 1101.7634, 1107.2998, 1115.3677, 1123.1643, 1130.7034, 1137.9977  
 MPDATA, C, 1, 43, 1145.0591, 1151.8988, 1158.5272, 1164.9542, 1171.1889, 1177.2400  
 MPDATA, C, 1, 49, 1183.1157, 1188.8236, 1194.3710, 1199.7646, 1205.0110, 1210.1162  
 MPDATA, C, 1, 55, 1216.7133, 1223.0825, 1229.2355, 1235.1834, 1240.9367, 1246.5050  
 MPDATA, C, 1, 61, 1251.8973, 1257.1220, 1264.6622, 1271.8678, 1278.7613, 1285.3632  
 MPDATA, C, 1, 67, 1291.6924, 1297.7659, 1303.5995, 1309.2078, 1316.3578, 1323.1597  
 MPDATA, C, 1, 73, 1329.6393, 1335.8201, 1341.7233, 1347.3682, 1352.7724, 1357.9517  
 MPDATA, C, 1, 79, 1362.9208, 1368.8568, 1374.5088, 1379.8981, 1385.0439, 1389.9637  
 MPDATA, C, 1, 85, 1394.6731, 1399.1866, 1403.5171, 1407.6768, 1411.6764, 1415.5259  
 MPDATA, C, 1, 91, 1419.2347, 1422.8110, 1426.2627, 1429.5970, 1432.8206, 1435.9395  
 MPDATA, C, 1, 97, 1438.9596

MP, DENS, 1, 3970 ! kg/m<sup>3</sup>  
 MP, Rsvx, 1, 1e8 ! Ohm.m  
 MP, ALPX, 1, 8.0E-6 ! 1/K  
 MP, EX, 1, 402.1732e9 ! Pa  
 MP, PRXY, 1, 0.2337

! Input material properties of Graphite

MPTEMP

MPTEMP, 1, 300, 320, 340, 360, 380, 400

MPTEMP, 7, 420, 440, 460, 480, 500, 525

MPTEMP, 13, 550, 575, 600, 625, 650, 675

MPTEMP, 19, 700, 725, 750, 775, 800, 825

MPTEMP, 25, 850, 875, 900, 925, 950, 975

MPTEMP, 31, 1000, 1040, 1080, 1120, 1160, 1200

MPTEMP, 37, 1250, 1300, 1350, 1400, 1450, 1500

MPTEMP, 43, 1550, 1600, 1650, 1700, 1750, 1800

MPTEMP, 49, 1850, 1900, 1950, 2000, 2050, 2100

MPTEMP, 55, 2150, 2200, 2300, 2400, 2500, 2600

MPTEMP, 61, 2700, 2800

MPDATA, DENS, 2, 1, 1850

! kg/m<sup>3</sup>

MP, C, 2, 310.5, 1.7

! J/kg.K

MP, Kxx, 2, 65, -0.017

! W/m.K

MP, RSVX, 2, 26e-6, -3e-8, 2e-11, -6.4e-15, 7.8e-19

! Ohm.m

MP, ALPX, 2, 8.0E-6

! 1/K

MP, EX, 2, 193.1678e9

! Pa

MP, PRXY, 2, 0.2383